FRICTION STIR WELD DEVELOPMENT AND DYNAMIC CRASH TESTING OF BUMPER-BEAM/CRASH-BOX ASSEMBLIES MADE FROM AA6082-T6 and AA6063-T6 EXTRUSIONS

A Dissertation by

Farzad Baratzadeh

Master of Science, Wichita State University, 2010

Submitted to the Department of Mechanical Engineering
and the faculty of the Graduate School of
Wichita State University
in partial fulfillment of
the requirements for degree of
Doctor of Philosophy

December 2013

FRICTION STIR WELD DEVELOPMENT AND DYNAMIC CRASH TESTING OF BUMPER-BEAM/CRASH-BOX ASSEMBLIES MADE FROM AA6082-T6 and AA6063-T6 EXTRUSIONS

The following faculty members have examined the final copy of this dissertation for form and content, and recommend that it be accepted in partial fulfillment of the requirement for the degree of Doctor of Philosophy with a major in Mechanical Engineering.

_____
Hamid Lankarani, Committee Chair

_____
Michael McCoy, Committee Member

_____
Ramazan Asmatulu, Committee Member

_____
Krishna Krishnan, Committee Member

_____
Brian Driessen, Committee Member

Accepted for the College of Engineering

_____
Vish Prasad, Interim Dean

Accepted for the Graduate School

_____
Abu Masud, Interim Dean

DEDICATION

To my wife Bahareh Karimi, my parents, and my sisters
for supporting my vision and helping me one day to turn it into a reality

ACKNOWLEDGEMENTS

The work presented here is the result of three years of study and research that started in the fall of 2010. First, I thank God for the greatest opportunity to complete this doctoral research study. I also thank my advisor, Dr. Hamid Lankarani, for his assistance and support since I first became his graduate student six years ago. His wide knowledge, logical way of thinking, and support have been of great value to me. In addition, I thank my advisors for their guidance, patience, and assistance. Great appreciation goes to two individuals at Wichita State University (WSU) for their support: Dr. Dwight Burford, Director of the Advanced Joining and Processing Laboratory (AJPL) at the National Institute for Aviation Research (NIAR), and Mike McCoy, Site Director of the Center for Friction Stir Processing at NIAR. I must also acknowledge Alan Bruce Handyside and Jeff Buller for their great assistance and help to complete this project.

This study was funded through the Center for Friction Stir Processing (CFSP), an Industry/UniversityCooperative Research Center under the National Science Foundation, of which WSU is a site member. This research would not have been possible without funding from WSU sponsors, especially the General Motors Corporation and Dr. Blair Carlson, Laboratory Group Manager at General Motors Research and Development.

I thank my wonderful family, especially my wife, my father, and my mother, whose love and care have helped me grow to be the person that I am today. I also thank all of the staff and students in the WSU AJPL for their assistance and collaboration with research, testing, sample preparation, welding, and experimentation advice.

ABSTRACT

Advancements in friction stir welding (FSW) have enabled the development and testing of a lightweight automotive bumper-beam/crash-box assembly. Previously, a test fixture to dynamically (crash) test the functionality of advanced bumper assemblies fabricated by FSW was developed. This FSW development work included microstructural examination and static mechanical testing. Results from coupon-level development were compared against results from component-level testing of prototype articles using micrographs and an advanced electronic (signal/frequency analysis) non-destructive evaluation (e-NDE) technique in order to detect weld anomalies primarily in the form of voids. Due to the geometry of the welded part joint, conventional mechanical testing methods (tensile and peel test) were not applicable. Therefore, a wedge test was devised to test the relative toughness of the FSW joint. From recorded data, toughness plots were calculated to select the best joint from three weld tools, each having the same basic threaded probe and Wiper™ shoulder designs, and differing only in probe features. In addition to the basic tool configuration, one tool had a set of partial CounterFlow™ grooves, and the other had a set of partial straight flats. Each also had a special geometrical feature added to the tip of the tool probe, referred to as a concentrating tip, to improve metal flow at the end of the probe in order to inhibit void formation. Traditional sled testing for low-speed bumper requirements was performed at the General Motors (GM) Research and Development (R&D) facility in Detroit, Michigan, and drop tower tests were performed using an FSW test fixture at the National Institute for Aviation Research (NIAR) at Wichita State University (WSU). These dynamic tests were performed on bumpers using both FSW and gas metal arc welding (GMAW). Finite element analysis (FEA) was used to compare the predicted damage to the actual damage sustained by the bumpers fabricated by GMAW and FSW, respectively.

TABLE OF CONTENTS

TABLE OF CONTENTS (continued)

TABLE OF CONTENTS (continued)

LIST OF TABLES

LIST OF FIGURES

LIST OF FIGURES (continued)

LIST OF FIGURES (continued)

LIST OF FIGURES (continued)

LIST OF FIGURES (continued)

LIST OF FIGURES (continued)

LIST OF ABBREVIATIONS

AA	Aluminum Alloy
AJPL	Advanced Joining and Processing Laboratory
AS	Advancing Side
ASTM	American Society for Testing and Materials
CAD	Computer-Aided Design
CFSP	Center for Friction Stir Processing
DXZ	Dynamically Recrystallized
DOE	Design of Experiments
e-NDE	Electronic Non-Destructive Evaluation
EST	Effective Sheet Thickness
FAA	Federal Aviation Administration
FEA	Finite Element Analysis
FEM	Finite Element Model
FMVSS	Federal Motor Vehicle Safety Standard
FSP	Friction Stir Processing
FSW	Friction Stir Welding (Welded)
FSSW	Friction Stir Spot Welding (Welded)
GM	General Motors Corporation
GMAW	Gas Metal Arc Welding (Welded)
HDAZ	Heat and Deformation Affected Zone
HAZ	Heat-Affected Zone
HV	Vickes Hardness Profile

in	Inch
ipm	Inches per Minute
KE	Kinetic Energy
kph	Kilometers per Hour
ksi	Kilo Pounds per Square Inch
LH	Left-Hand
MDB	Moving Deformable Barrier
MEK	Methyl Ethyl Ketone
MI	Metal Inert Gas Welding
mm/s	Millimeters per Second
MPa	Mega Pascal
NCAP	New Car Assessment Program
NIAR	National Institute for Aviation Research
PDS	Process Development System
PFSW	Plunge Friction Spot Welding (Welded)
PRZ	Partially Recrystallized Zone
RFSW	Refill Friction Spot Welding (Welded)
RH	Right-Hand
rpm	Revolutions per Minute
RPT	Retractable Pin Tool
RS	Retreating Side
SE	Specific Weld Energy

SZ	Stir Zone
TMAZ	Thermomechanically Affected Zone
TWI	The Welding Institute, Ltd.
UTS	Ultimate Tensile Strength
VMS	von Mises Stress
WSU	Wichita State University

CHAPTER 1

INTRODUCTION

1.1 Background

A new technology and welding method was invented patented by Wayne Thomas and others in 1991 at The Welding Institute (TWI) of Cambridge, England. Called friction stir welding (FSW), this method is a localized solid-state, extrusion and forging joining process. Conventionally it involves pressing a rotating non-consumable tool, with a shoulder and terminating threaded pin, into the joint line between two rigidly clamped plates placed on a backing plate and then moving the tool along the joint line formed by the butting surfaces. A schematic representation of the FSW process as well as information regarding the terminology used to describe friction stir welding is provided in Figure 1.1 [1–2].

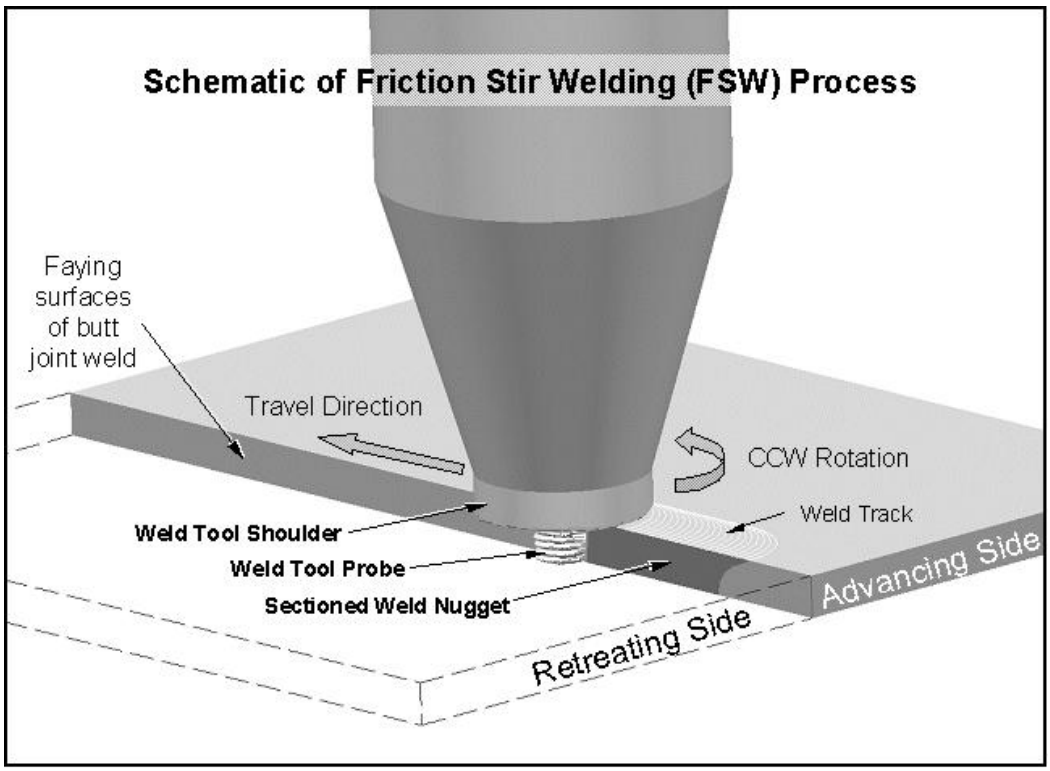

Figure 1.1. Schematic representation of friction stir welding process and terminology [14].

In FSW technology, the rotating tool generates a considerable amount of heat due to friction and plastic deformation of the workpiece material [2]. Upon contact with the top surface of the workpiece, heat is created through friction at the shoulder and, to a lesser degree, the pin surface, which in turn causes the material to soften. As the tool is plunged into the material being welded, severe plastic deformation and flow of the plasticized metal around the tool occurs, releasing a large amount of heat. This allows the tool to be readily translated along the welding direction, whereby material is transported from the front of the tool to the trailing edge of the tool and forged into a joint [3, 4].

FSW is a solid-state process because the maximum temperature during welding does not exceed the melting temperature of the bulk material. In fact, it typically only reaches approximately 80% of the base material's melting temperature. Basically, the process is most appropriate for components that are long (sheets and plates) but can be adapted for pipes, hollow sections, and complex curvatures [5, 6].

FSW was used in the present study to build an experimental bumper-beam/crash-box assembly having partial FSW butt joints between extrusions of dissimilar alloys. Mechanical and metallurgical characterization studies of FSW joints were carried out to test several new FSW weld tool features. The new tool evaluation was deemed warranted because the original weld tool designs, those that had been evaluated using coupon-level testing, were not found to be capable of producing void-free (sound) joints at the test article (assembly) level. Deviating from the process parameters (process window) established in the coupon-level work could not even resolve the issue related to these tools. Therefore, a tool redesign evaluation was undertaken for FSW at the assembly level (without coupon development work). Three tool designs were investigated for joining the aluminum alloy (AA) 6082-T6 bumper beam to the higher strength

AA6063-T6 crash box extrusions to produce the assembly. The key innovation added to the tool was a concentrating probe tip that was designed to draw the joint material at the probe tip together and thereby resist void formation at this location in the joint. Feedback forces at the tool center, in particular drag force and transverse force, were considered using a new electronic non-destructive evaluation (e-NDE) methodology [7] to confirm that sound welds were produced in the assemblies with the new tool designs. This e-NDE methodology is based on algorithms developed earlier by Boldsaikhan et al. [8]. Because of the configuration of the assembly joint, a new wedge test was devised to evaluate the mechanical strength of the partial butt joint between the bumper beam and crash box extrusions.

1.2 Advantages of Friction Stir Welding

Friction stir welding has several benefits over traditional arc or fusion welding. FSW is a relatively new solid-state joining technology for joining metals and plastics. Unlike fusion welding, FSW does not require melting or filler material. It generates no fumes, results in improved weld quality and reduced distortion for the proper parameters, is adaptable to all positions, and is relatively quiet compared to other joining methods. Also, FSW has a reduced defect rate and lower health hazard. It can improve mechanical properties such as fatigue, fracture toughness, and ductility, and it simplifies dissimilar alloy welding [9, 12].

1.3 Research Objective

The application of FSW to aluminum is not new, but its application to the bumper-beam/crash-box assembly allowed for those benefits that are unique to FSW. Loading on the joint requires a significant nugget size, which precludes resistance spot welding. Gas metal arc welding (GMAW) is feasible but introduces a significant heat input and dimensional distortion from end to end of the bumper beam, which needs to be minimized in order to reduce any

residual stress when attaching the bumper assembly to the front rail face pads. Therefore, in order to produce a feasible solution, advancements were applied in the present study to build an experimental bumper-beam/crash-box assembly having partial FSW butt joints between dissimilar alloy extruded components.

The objective of this study was to design, simulate, fabricate, and dynamically test a friction stir-welded (FSW) bumper-beam/crash-box assembly. This required conducting a case study based on both coupon-level and component-level work. It meant developing a robust FSW process for partial butt joints between dissimilar alloys AA6082-T6 and AA6063-T6. The final objective of this research was to compare bumpers welded with FSW with bumpers welded using the traditional method of GMAW or fusion welding.

CHAPTER 2

LITERATURE REVIEW

As mentioned previously, friction stir welding was invented and patented by Thomas and others at The Welding Institute in 1991, but most of the research on this method has been published since 1997. FSW was first introduced in the United States in 1995 but since then has matured a great deal. The technology readiness level for FSW of aluminum alloys is high, with many successful industrial implementations. As development efforts and property characterizations have shown, FSW can be used to process ferrous, stainless, nickel, copper, and titanium alloys [9, 10].

The NASA Marshall Space Flight Center, Boeing Company, and Lockheed Martin Corporation's Michoud Facility are the first sites that started research on friction stir welding in the U.S. In general, there are many applications for FSW in the aerospace and automotive industries. Some of the first applications of FSW in the U.S. were in space applications like the Delta II Heavy Rocket and the welding of an aluminum-lithium alloy, AL 2195, for the Space Shuttle's external tank. For this dissertation, the majority of published research on friction stir welding of 6XXX series aluminum alloys that is available to the public has been reviewed. A discussion of the published work relating to microstructural testing and mechanical testing involving FSW of 6XXX series aluminum alloys is described here [11].

2.1 Basics of Friction Stir Welding

Friction stir welding is a solid-state, hot-shear joining process, whereby the material temperature during welding does not does not exceed the melting temperature ($T_{welding} < T_{melting}$) of the alloys, typically only reaching approximately 80% to 90% of the melting temperature. Originally the process was considered most appropriate for long components, such as sheets and

plates, but FSW can be adapted for pipes, hollow sections, and positional welding [5, 12]. Applications using short or discontinuous welds are being developed, hence the need for this study. This technique was used as a new way to weld high-strength alloys that were difficult to join with conventional techniques. It was initially used for aluminum alloys and then developed for many different materials due to its suitability for joining. To form a basic butt weld joint with this process, a weld tool (usually cylindrical made from steel) with a particular rotation speed rotates and plunges into the workpieces that are to be welded. Because of the velocity difference between the rotating tool and workpieces, friction results, causing a considerable amount of heat, deformation of the workpiece material, and decrease in the flow stress of material around the rotating pin and shoulder tool. The weld joint is produced by carrying material away from the leading side of the tool to the trailing side of the tool where the material is forged and extruded into a solid-state joint [12, 13]. The many different weld joint configurations include T-joints, lap joints, fillet joints, and butt joints, which are currently employed in the aerospace, automotive, railway, and maritime industries.

A schematic representation of FSW for a simple butt joint configuration was shown previously in Figure 1.1. As illustrated, moving the rotating FSW tool along the joint line produces what are conventionally called retreating and advancing sides. The advancing side is the side for which the surface of the tool is rotating in the same direction as the direction of travel. The retreating side is the other side of the tool where the tool surface is traveling opposite the direction of travel. This differing motion creates asymmetry in the weld [5]. For a given workpiece material, the most important parameters of interest in the basic FSW process are the following: (1) tool rotation rate ($\boldsymbol{\omega}$) in either the clockwise or counterclockwise direction, (2)

tool travel speed or welding feed rate (ν) along the line of joint, (3) plunge depth, (4) tool geometry, and (5) tool material.

Rotation speed is the amount of energy being contributed per unit time and is measured in revolutions per minute (rpm). The temperature of the weld zone is obtained with travel speed and is measured in inches per minute (ipm) or millimeters per second (mm/s). The role of plunge depth is to control the forge force behind the weld tool, thus contributing to the joint formation with no defects. Weld power (P) and specific weld energy (SE) equations were developed by Reynolds and Tang [23] to characterize FSW. The tool rotation speed (**ω**) and spindle torque (T) are used to calculate P:

$$P = \boldsymbol{\omega} T \tag{2.1}$$

It is assumed that the spindle efficiency is equal to unity; however, when making changes to the design of the weld tool, and thus weld parameters, this assumption is no longer valid. See equation (2.2). Also, the specific weld energy is calculated by dividing the weld power by the tool travel speed (ν_f) in inches per minute:

$$SE = P/\nu_f \tag{2.2}$$

2.2 Friction Stir Processing

Friction stir processing (FSP) is a variant of friction stir welding. It was developed based on the basic concepts of FSW (a solid state welding process), but FSP is used to modify the local microstructure of a component as opposed to joining components together. FSP may be used to modify surface material to introduce microstructural modification close to the near-surface layer of metal components. It provides the ability to thermomechanically process selected locations on a structure's surface to a range of depths (from shallow to full penetration) to alter the properties of the material, e.g. grain size [15, 16].

2.3 Friction Stir Welding Tools

The process of friction stir welding requires a non-consumable welding tool, sometimes referred to in the literature as a weld tool. A weld tool with the CounterFlow™ feature is illustrated in Figure 2.1. The function of this pin tool is to produce thermomechanical deformation in the workpiece through frictional heating and mechanical stirring. The tool is slowly plunged into the workpiece as it is rotated at a fixed speed. Once the workpiece has been softened to the desired level through heating from friction and mechanical stirring, the material of the workpiece can be easily mixed by the probe and shoulder due to the low flow strength of the material. While the probe extrudes the material in a circular pattern, the tool shoulder keeps the plasticized material contained in order to provide the required forging pressure for forming a consolidated joint [3, 9, 15].

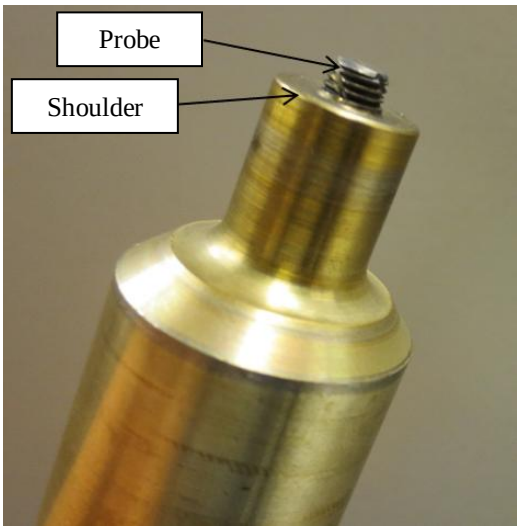

Figure 2.1. Weld tool profile [19].

The basic friction stirring tool consists of a shoulder and a probe. The probe can be integral with the shoulder or inserted in the shoulder as a separate piece, and can possibly be made of a different material. The design of the probe and shoulder significantly affects the quality of the weld as well as the rate of welding. When welding thin sheets of material, as in this

study, the shoulder generates much of the heat. As the thickness of the weld increases, such as in the plate material, the probe of the tool generates an increasing amount of heat and stirs the material being welded. The shoulder plays a decreasing part in overall heat generation as the thickness of the weld increases while preventing the plasticized material from escaping from the weld region [17].

The geometry of the probe can be cylindrical, quadrangular, or conical. The material, structure, and configuration of the FSW tool is related to the desired quality of the weld, material of the workpiece, rotation speed, and travel speed (e.g., productivity). Usually a tool designer adds flutes and/or threads to the probe in order to promote better material flow and avoid the formation of defects and wormholes.

In the welding of aluminum or aluminum alloys, the most common tool materials are tool steels (e.g., H13) and high-strength steels (e.g., Maraging 300), which retain their strength and hardness at FSW processing temperatures (usually below 900°F). Other materials, such as MP159, a cobalt-based bolt material for high-temperature applications, are used in both research and production. With the selection of appropriate welding parameters, a steel tool produces the proper weld quality and strengths without significant tool wear. However, if a steel tool is used to weld more abrasive materials, such as metal matrix composites, tool wear becomes an important issue due to the presence of rough particles and the strength of the material to be welded. Tools can be made of more exotic materials such as tungsten carbide, tungsten, and molybdenum to decrease or eliminate tool wear and distortion, which have been observed in steel tools when welding in materials at a high rotation speed and/or forces [9, 18].

2.4 Metallurgical Processing Zones

The heating of a material during the friction stir welding process is not intended to bring the material above the solidus temperature, therefore making FSW a solid-state welding process. Also, FSW can be considered to be a metal working process that includes both forging and extruding, which are related to processes used to create wrought manufactured goods [20].

FSW has important effects on the microstructure of the base material. The microstructure of a friction stir weld is separated into four principal zones: parent or base material, heat-affected zone (HAZ), thermomechanically affected zone (TMAZ), and weld nugget or dynamically recrystallized zone (DXZ). Each of these zones has a distinct microstructure property. The first zone, which is very far from the joint line, is called the unaffected base metal zone. In this zone, there are no microstructural or property changes in the metal. In the second zone, HAZ, the material does not experience plastic deformation; however, the heat of welding influences this region by causing some microstructural changes (break up of inter-metallic particles, variable grain size, and over-aging, causing a decrease in hardness). This area of the weld is known as the weak point due to its minimum hardness and fracture initiation. In the third zone, TMAZ, which lies in toward the joint line, material is affected by the heat generated by the FSW process and may contain some areas of partial recrystallization. The grain size of the TMAZ remains the same as that of the base material; however, its orientation is altered by partial mechanical deformation. The fourth zone, the nugget area or stir zone, is comparable to the pin diameter in size. The grain size here is substantially smaller than the grain size in base material. This zone is the dynamically recrystallized region bounded by the TMAZ. Here the welded material is heavily deformed and corresponds to the pin location during the welding. These four zones have been identified by TWI, but their terminology is not used uniformly throughout the FSW

community. For example, some authors recognize the nugget as the DXZ, while others refer to it as the stir zone (SZ). The TMAZ is also referred to as the heat and deformation affected zone (HDAZ) and the partially recrystallized zone (PRZ). The use of the term PRZ suggests the presence of both recrystallized and deformed grains. TWI has agreed to categorize the TMAZ and the region underneath the shoulder as two separate zones. Some authors categorize the region underneath the shoulder as the region of rotation and therefore categorize it as a part of the SZ, while other authors continue to maintain that the SZ actually includes the nugget, the TMAZ, and the region immediately underneath the shoulder [11, 15, 21].

Figure 2.2 shows some important elements of the weld zone based on results produced by an original tool design, similar to the tool represented previously in Figure 2.1. As can be seen, the nugget zone is asymmetrical where it expands more towards the advancing side. Tool geometry and a backup plate define the shape of the inverted trapezoidal profile of the joint shown here. The wide base of the trapezoid corresponds to shoulder contact area and heating, while the thin base responds to heating of the narrower pin profile, which is strongly influenced by the heat sink effect of the backup plate. This sort of joint profile has been utilized for a broad range of FSW joints in a wide variety of metals [15, 21].

Figure 2.2. Schematic of butt joint cross section showing four distinct zones.

In certain materials, such as titanium steels and alloy steels, the heat of welding may cause polymorphism, phase changes that cause recrystallization with no strain. Consequently, any TMAZ that may have formed will likely be recrystallized, causing difficulty in

differentiating between the HAZ and TMAZ boundaries. Other materials such as austenitic stainless steels and aluminum alloys do not cause polymorphism and, therefore, simplify the identification of the TMAZ [15, 21].

2.5 Metalworking Process

Researchers have conducted an excellent characterization of the most fundamental thermal and mechanical principles of friction stir welding. A number of first-order approximation models in order to explain that FSW could be modeled as a forging and extrusion process was developed by Arbegast [22]. He was able to correlate his FSW model with experimental data. His model associates five important process zone with FSW, as shown in Figure 2.3. When the rotational weld tool has been plunged into the workpiece and plasticized the material, it can begin travel to the joint line. While the weld tool is in the steady-state process of forming a joint, it can be characterized at any time by the zones depicted here.

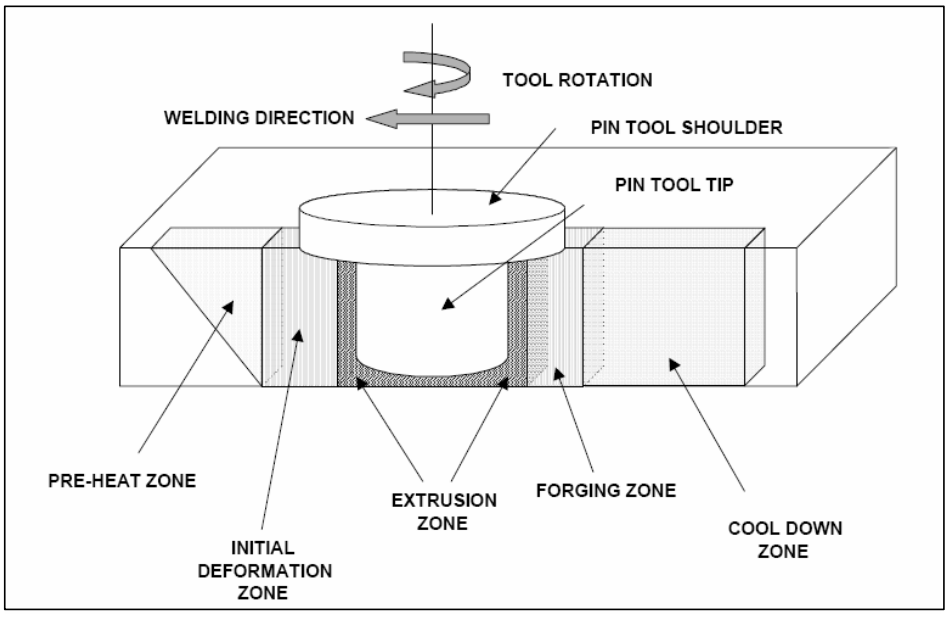

Figure 2.3. Schematic of metallurgical processing zones during FSW [22].

The pre-heat zone refers to the frictional heating of the spinning weld tool, the plastic strain energy release of the deforming material, and the heat generated by the FSW. If the tool

travels faster than the heat conduction ratio in the material, then the process force will increase, resulting in a weld that may be too cold to extrude around the pin. Thus, weld defects (wormholes or voids) are formed due to the faster travel speed of the weld tool compared to the material heat conduction, as shown in Figure 2.4 [11].

In the initial deformation zone, the pre-heated metal begins to plasticize the material and deform ahead of the weld pin tool. Also, as the strain energy is released, heat forms in this zone and results in softening the material [11].

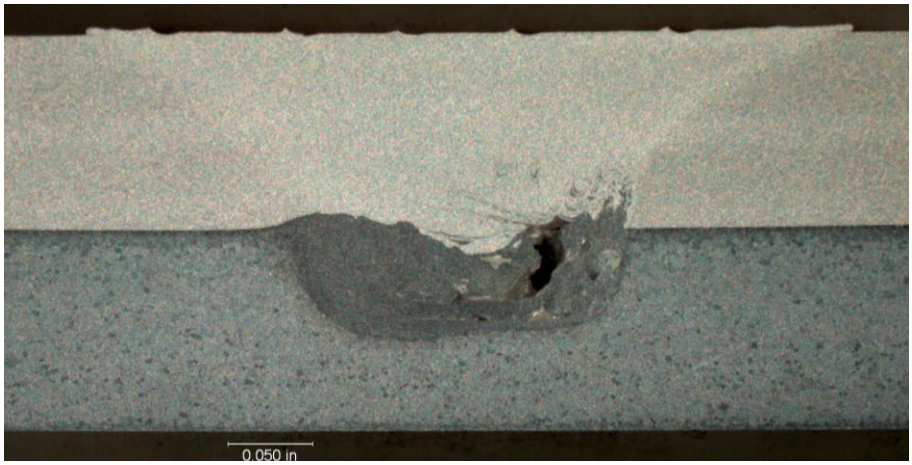

Figure 2.4. Weld macro of aluminum alloys 6082-T6 and 6063-T6 with wormhole and several small voids (lap weld configuration) [13].

In the next zone, the extrusion zone, material from the advancing and retreating sides of the joint is mixed and then pushed to extrude around the rotational weld tool. Usually, a larger volume of material passes on the retreating side of the tool than on the advancing side. In addition, the material is also moving underneath the weld tool probe and shoulder. The FSW weld temperature has its maximum value in this zone, which is about 0.6 to 0.9 of the melting point temperature ($T_{melting}$) and can be approximately calculated by

$$\frac{T}{T_{melting}} = K\left(\frac{\omega^2}{V_f \times 10^4}\right)^a \tag{2.3}$$

where **ω** is the rotation speed (rpm), *a* is in the range of 0.04–0.06, and *K* is a constant value for aluminum alloys ranging between 0.65 and 0.75 [11].

In the forging zone, all extruded material from the shoulder, pin, and beneath the pin is forged under a large hydrostatic force into a consolidated, void-free joint. If there is no sufficient downward pressing force on the weld tool, then volumetric defects can be observed [11].

The last zone is the cool-down zone where the final FSW joint is created and the material remains hot for a limited amount of grain growth in the nugget. The cool-down process is very fast because FSW is a forging process and a localized extrusion. Also, the weld anvil and undeformed material in the vicinity of the joint weld act as a heat sink, which results in quenching the material temperature back to room temperature [11].

2.6 Basic Types of FSW Joint Design

In general, different types of joint configurations for friction stir welding can be applied to most geometric structural shapes and most types of joints such as the lap joint, butt joint, T-joint, and fillet joint, as shown in Figure 2.5. The most convenient joint configurations in FSW are the butt weld and lap weld configurations. Other types of joint configurations are essentially variations or combinations of these. Details are discussed later in this chapter [9].

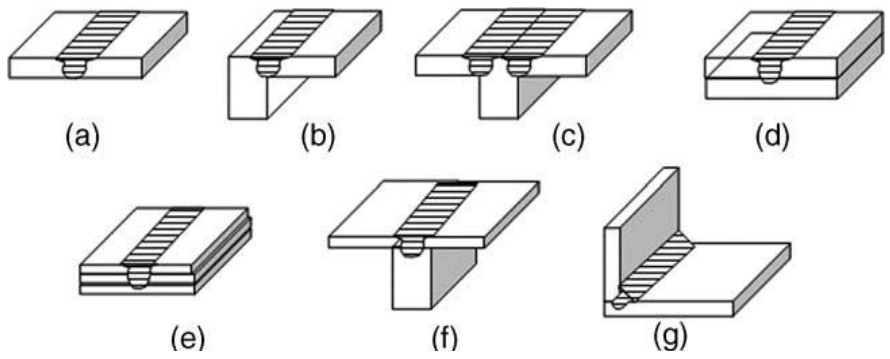

Figure 2.5. FSW joint configurations: (a) butt weld, (b) edge butt weld, (c) T butt weld, (d) lap weld, (e) multiple lap weld, (f) T lap weld, and (g) fillet joint [9].

2.6.1 Butt Joints

Butt joints are the most common configuration of friction stir welding used in different applications. In this simplest form of welding, two workpieces with the same thickness and square mating edges are placed next to each other on a rigid backing plate and clamped tightly together, as shown in Figure 2.6 [24].

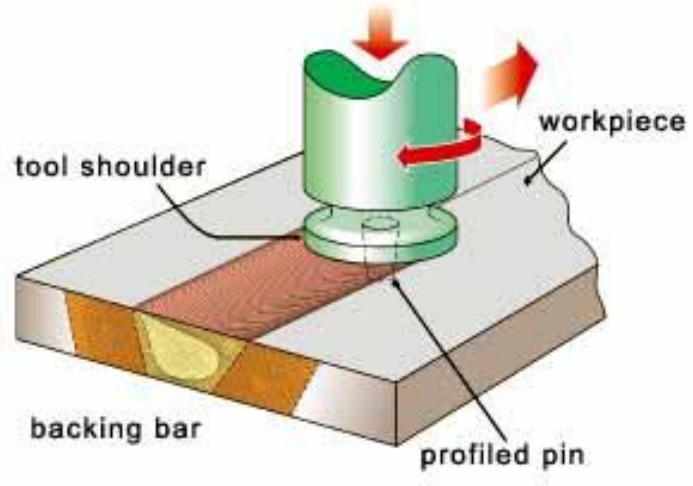

Figure 2.6. Butt joint configuration [24].

The main reason for using rigid fixturing is to keep the two sheets of material from spreading apart or lifting during welding. The FSW tool, consisting of a shoulder and pin, is then rotated to a particular speed and tilted with respect to the sheet's normal orientation. The tool is gradually plunged into the workpiece material at the butt line until the shoulder of the tool forcefully contacts the upper surface of the material and the pin is embedded in the joint a short distance from the backing plate. At this time, the lateral forces (X and Y) are large enough that additional care is required to ensure that the plates remain in the butt configuration and are not allowed to separate. To begin a weld, a downward force is applied through the tool to maintain contact between the plates. A short dwell time is then applied to allow for the growth of the thermal fields for softening and preheating the material along the joint line. At the end of the

weld, the tool is moved up while still being rotated, whereby the pin is retracted from the workpiece normal to the surface of the plate. As a result, an exit hole remains at the end of the weld. The shoulder contact on the material leaves a series of semi-circular patterns in the weld track, as illustrated schematically in Figure 2.7. Consequently, the start and end of the weld line will not be completely welded, especially at the end of the weld, where an exit hole is left [21].

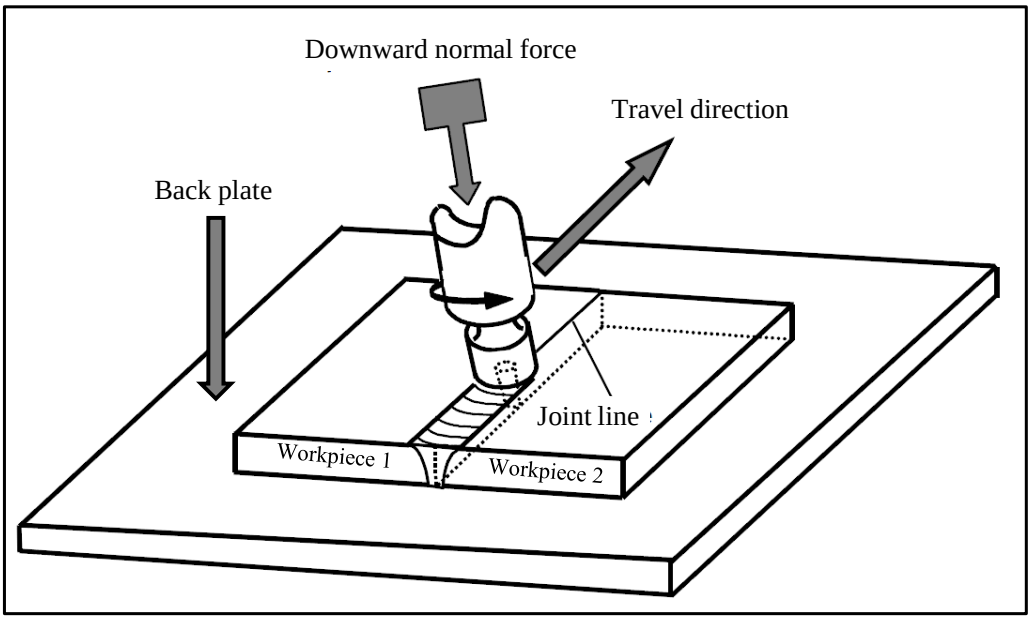

Figure 2.7. Force of tool at desired travel speed along butt line [21].

2.6.2 Lap Joints

A lap joint consists of two lapped sheets or plates clamped together. Depending on the bottom sheet thickness, a structurally supporting backing plate may or may not be needed. Conventionally, a rotating pin tool is plunged through the upper sheet normal to the surface and into the bottom sheet a set depth less than its thickness. Once the plunge phase of the weld is complete, the tool is traversed along the desired direction to join the two sheets together [9].

The same methods and principles mentioned in the previous section for butt joints apply to lap welds, with a few exceptions. In the lap weld there is no butt line where the pin tool can be plunged among the sheets; rather, the pin tool needs to be inserted through the top sheet. Also, it

is necessary for the stirring movement to break up the oxides, scale, and the other contaminants at the interface. This is the fundamental difference between butt and lap joints. For butt welds, stirring is primarily in the plane of the abutting surfaces being welded. In contrast, for lap welds, stirring is out of plane and across the interface of the two surfaces being welded.

Brooker et al. [25] introduced an innovative lap weld tool. The major difference between their lap weld tool and conventional tools for butt joints is the introduction of a second shoulder, which is placed at the interface between the two sheets being welded (Figure 2.8). Most existing publications regarding lap welds indicate that drilling a starting hole is not required to produce a sound lap joint [25].

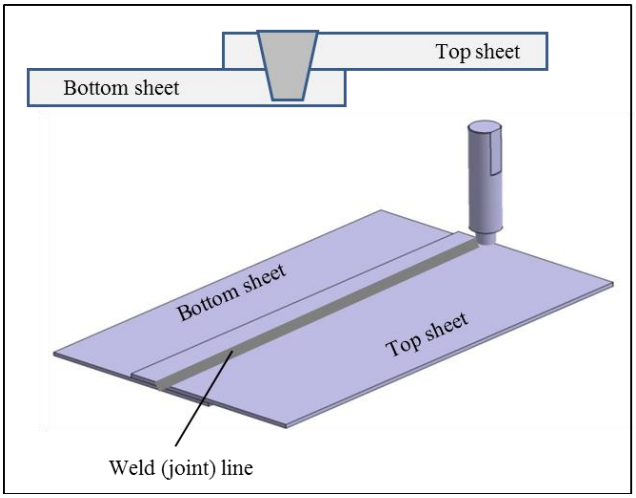

Figure 2.8. Schematic of lap joint pin tool.

In lap joints, the top plate of a lap joint must be distinguished from the bottom plate since it is in contact with the shoulder. The end of the pin needs to penetrate through the top sheet completely and enter a sufficient distance into the bottom sheet. It is not necessary for the end of the pinto pass all of the way through the bottom sheet, since, in contrast to butt joints, there is no weld root closure involved. However, the effect of the intrusion distance into the lapped (bottom) sheet on the mechanical properties of the weld cannot be underestimated. The notches on either

side of the joint (Figure 2.9) are potential sites for crack initiation (under certain loading conditions), and as such, they can have a significant effect on mechanical properties. While lap joints may not be as strong as butt joints, they have been shown in several case studies to have sufficient fatigue and static properties to replace fastened joints [25].

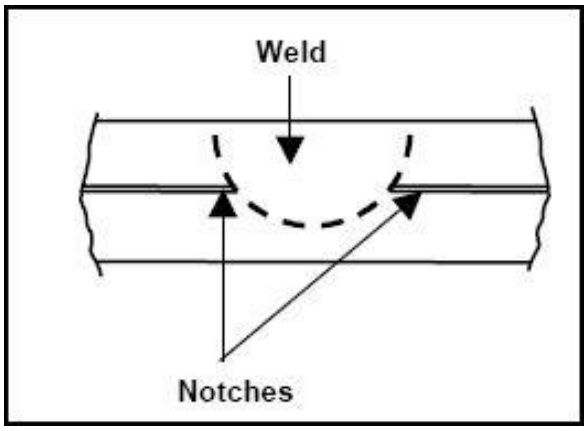

Figure 2.9 Notches location in lap joint [25].

2.6.3 Friction Stir Spot Welding

A variant of FSW is friction stir "spot" welding (FSSW), which creates a lap weld with discrete joints similar to installed fasteners [19]. As with FSW, there is no bulk melting in FSSW. This method has been shown to be more efficient (cost savings and significant energy) compared to electric resistance spot welding [26]. The principle of FSSW is based on the continuous FSW process. However, in its simplest form, FSSW is much less complex in the sense that the actual welding time itself is very short, but the process dynamics involved are still the same—tool plunge, material mixing (during dwell time), and tool retraction. The key parameters for FSSW are tool geometry, weld rotation speed, plunge depth, and dwell time. Each of these plays an important role in the weld in terms of material mixing, heat input, and weld cycle time, all of which are key to achieving a good weld in terms of strength and material morphology [27].

Some spin-off technologies can be recognized by considering FSW as a “controlled-path extrusion” rather than a “welding” process. Recently two variations of FSSW are being used in production: one is “plunge” friction spot welding (PFSW), which was patented by the Mazda automotive company in 2003, and the other is “refill” friction spot welding (RFSW), which was patented by the GKSS Research Centre in 2002 [10].

2.6.3.1 Plunge Friction Spot Welding

In plunge friction spot welding, a rotating fixed pin tool is plunged and retracted through the upper and lower workpieces of the lap joint to plasticize the metal locally and stir together material from each sheet, as shown as Figure 2.10. Although this method creates an exit, or pull-out hole, in the center of the spot, the fatigue life and strength are adequate to allow application at a reduced cost of production, as in the Mazda RX-8 aluminum rear-door structure. Since 2003, the Mazda company has produced up to 100,000 vehicles with this PFSW rear-door structure, which reportedly have very good structural stability against a side impact and provide five-star roll-over protection [10].

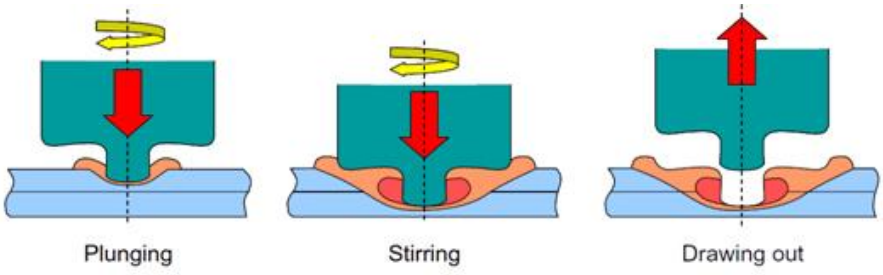

Figure 2.10. Plunge friction spot welding [29].

Tweedy et al. [30] investigated the important parameters of FSSW on bare AA7075-T6 and 2024-T3 of 0.040-in (1 mm)-thick lap joints. They found that the plunge rate had a minor effect on the strength of the joint but that the rotation speed of the tool was very important. Dwell time and plunge depth were also key factors. Once the FSW tool reached a certain depth,

the strength of the joint changed only slightly for increasing the plunge depth, as shown in Figure 2.11, demonstrating that sufficient depth of probe penetration was achieved to produce a joint with consistently strong properties. As shown in Figure 2.12, for the material to be mixed adequately, the tool must be in the material for a certain amount of dwell time. Once the ideal point is reached, not only will more mixing not increase the strength of the joint, but longer dwelling may weaken the joint due to overheating [3, 30].

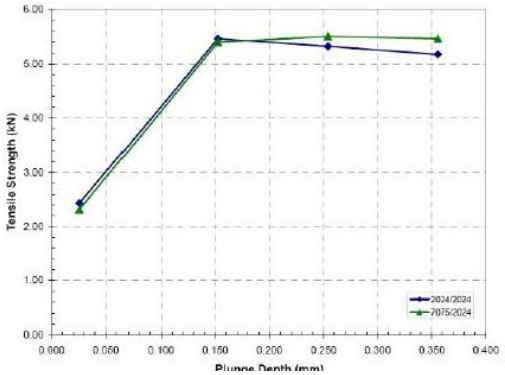

Figure 2.11. Effect of plunge depth [30].

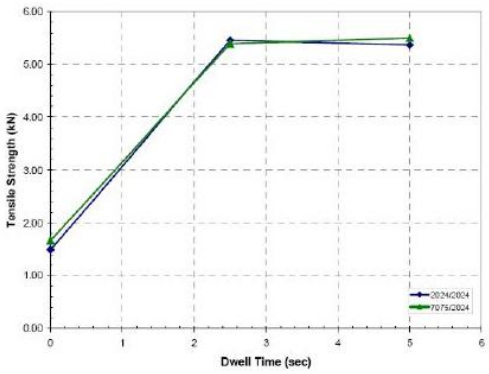

Figure 2.12. Effect of dwell time [30].

2.6.3.2 Refill Friction Spot Welding

As mentioned previously, refill friction spot welding was developed by the GKSS Research Centre and is currently being evaluated at the South Dakota School of Mines & Technology Advanced Materials Processing Center under license to the RIFTEC-GmbH company. In RFSW, a rotating pin tool with a separate shoulder and pin actuation system is used. During the first half of the cycle, the plasticized material initially displaced by the pin is captured or contained by the shoulder. During the second half of the cycle, the plasticized material is re-injected into the joint, as illustrated in Figure 2.13. This process refills the joint nominally flush to the original surface of the top sheet. In addition to RFSW being developed as a replacement technology for rivets in aerospace applications, it is also being expanded as a tacking technology to restrain and hold parts during over-welding by linear FSW [10].

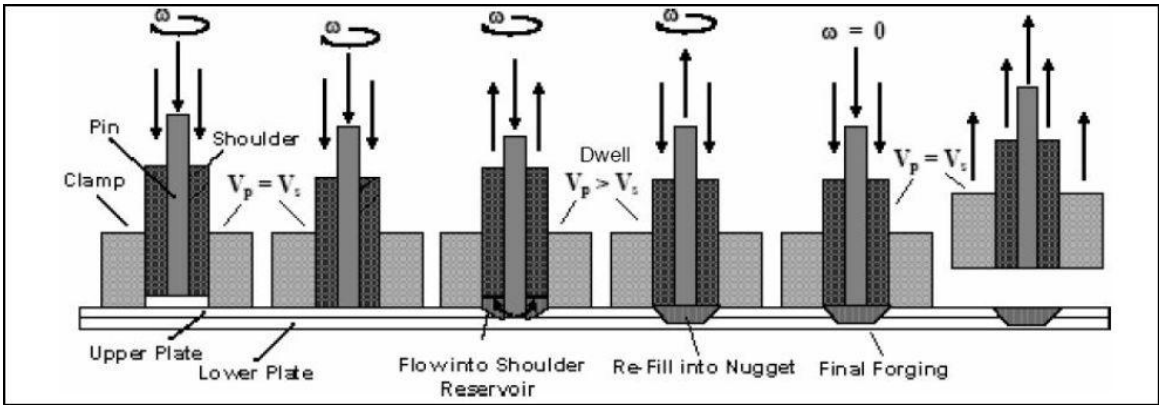

Figure 2.13. Schematic of refill friction spot welding [31].

2.6.3.3 Swept Friction Spot Welding

Swept friction spot welding is a type of FSSW which was introduced by TWI. The main advantage of this technique, compared to the traditional plunge FSSW, is the increased joint strength that results from increased shear area and the elimination of sheet thinning and hooking [32]. Typically during the formation of spot welds, the vertical translation of the joint interface occurs, causing a change in surface between the bottom and top sheets, which forms a downturned or upturned interface, and as a result, the effective sheet thickness decreases. Both results are negative effects in linear lap welds. This translation of the interface is normally consumed during a swept spot weld. The resulting interface will have no downturn or upturn [3, 30].

The Octaspot™ swept FSSW pattern involves five basic steps, as shown in Figure 2.14. The first step is a plunge (poke) into the material. In the second step, the tool is moved out to the perimeter of the tool path. In the third step, the tool is traversed around the perimeter for no less than 360 degrees. The fourth step occurs when the orbit is completed, and the tool is moved back to the center of the spot weld. In the fifth step, the tool is retracted. Swept FSSW has been shown to be up to 250% stronger than other types of joints, such as rivets and resistant spot

welds in a single-spot lap shear [35]. As shown in Figure 2.14, swept FSSW is different than plunge and refill FSW. In swept FSSW, there is an additional closed-loop translation movement, which increases the joint shear area and has been shown to have better mechanical properties compared to plunge and refill FSW [30, 33, 36].

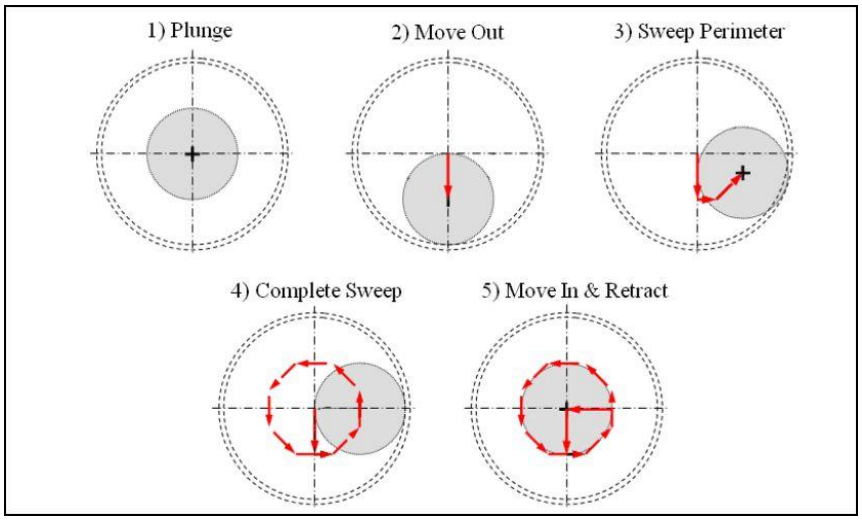

Figure 2.14. Schematic of swept friction stir spot welding [3].

Burford et al. investigated crack growth rates in 2024-T3 lap joint panels with AA7075-T6 stiffeners joined with swept FSSW. In that study, fatigue crack growth rates in flat, stiffened edge-crack panels were examined to evaluate the performance of weld joints produced by riveted and FSSW joints. According to the results, lower crack-growth rates were initiated in FSSW pre-crack panels than were observed in panels joined with rivets and unstiffened panels. By testing stress-relieved panels, it was observed that a beneficial residual stress field is presented around swept Octaspot™ joints. It was also observed that the pad-up effect, resulting from mechanically forming discrete integral joints between the stiffener and sheet, contributes to the observed lowered crack-growth rates in FSSW panels to a lesser amount than does the residual stress effect. In that study, it was concluded that the swept FSSW welds provide an effective

method for reducing the stress concentration associated with drilled holes required for installing conventionally installed fasteners [33].

2.6.3.4 Swing and Stitch Friction Spot Welding

Swing FSW was developed by the Hitachi Company, and stitch FSW was developed by the GKSS Research Center. In conventional friction stir spot welding, the tool plunges into the sheet and creates the weld, and then it retracts. In swing and stitch FSW technique the tool either translates or rotates a short distance after plunging and then it retracts, therefore it creates a larger contact area that leads to a higher strength which is considered an advantage [9].

In Figure 2.15, the difference between swing and stitch FSW is illustrated.

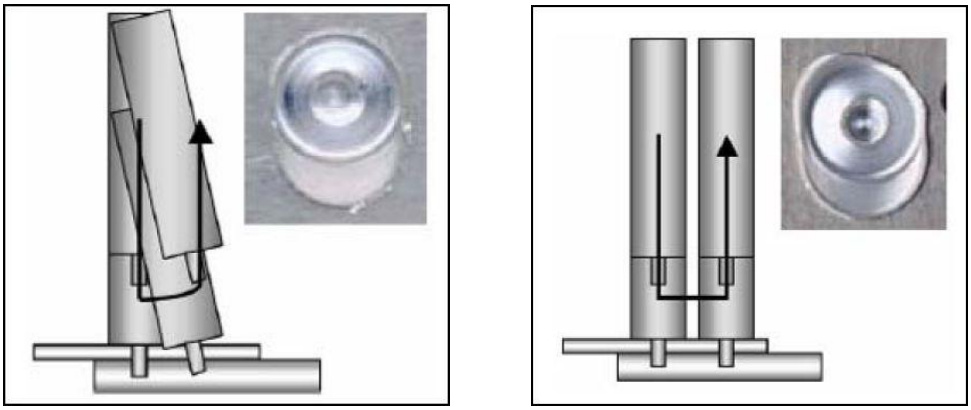

Figure 2.15. Swing FSSW (left) and stitch FSSW (right) [34].

2.7 Corrosion

2.7.1 Description

Corrosive oxidation occurs when oxygen bonds to metal atoms to form a surface oxide layer. In other words, the metal combines with the oxygen in the air and becomes a non-metallic material. The earth's crust has been approximated to be about 8% aluminum, the majority of which is often found in the form of an oxide called bauxite. Since aluminum is the second most plentiful metal element on the planet, it is also one of the most highly used non-ferrous metals.

Although aluminum is less expensive per volume than other metals, it is more expensive on a tonnage basis, due to its low density. Figure 2.16 represents a corrosion attack on the cross section of an FSW nugget.

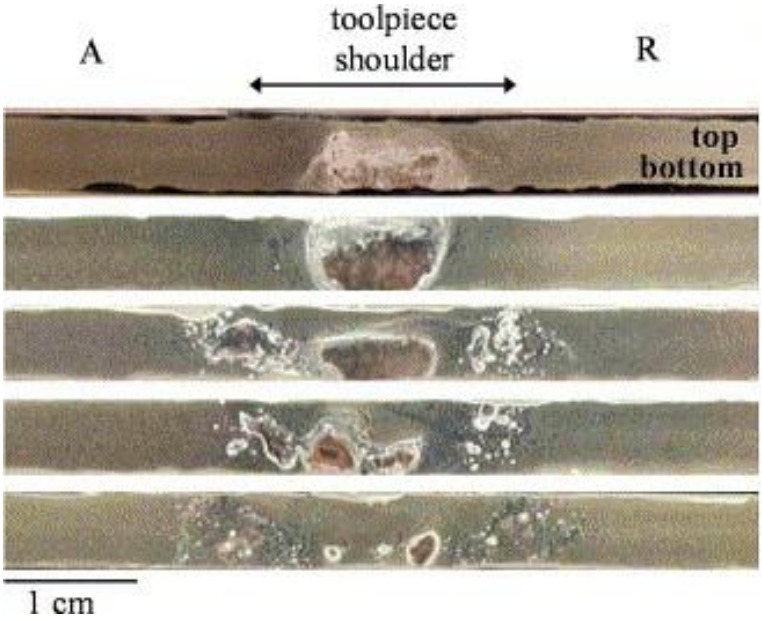

Figure 2.16. Corrosion attack on cross section of FSW nugget: A is advancing side and R is retreating side [43].

Aluminum alloys are separated into two broad classes—heat-treatable and non-heat-treatable—and into different product forms, including wrought (mechanically worked) and casting products [37, 38]. The condition of the environment (acidity or alkalinity) considerably affects the corrosion behavior of aluminum and its alloys. At higher and lower pH, aluminum is likely to corrode, but not always. If an aluminum specimen is submerged into concentrated nitric acid, then the specimen would be resistant to the acid. However, if the same specimen is placed in a more alkaline solution, then the accelerated corrosion is due in part to a more rapid rate of "attack," which results in pitting of the specimen surface. In a highly acidic condition, a more general attack should result, since the oxide is more susceptible to attack than the aluminum [37, 38]. Aluminum's resistance to corrosion is dependent upon a protective oxide film. When the pH

is between 4.0 and 8.5, the film is stable in an aqueous media. The film is self-renewing, and accidental abrasion or other surface film mechanical damage is repaired quickly. The environment that promotes the corrosion of aluminum and aluminum alloys, therefore, must be one that continuously abrades the oxide film mechanically or contributes to conditions that locally degrade the protective oxide film, thus reducing the availability of oxygen to rebuild it [37, 38].

2.7.2 Types of Corrosion

Corrosion is a significant issue for the majority of welded joints. Since corrosion is potentially present in every application, it must be considered when evaluating the useful life of a structure. Several different types of corrosion exist:

Uniform corrosion is described by corrosive attack occurring uniformly over the entire surface or a large fraction of it. It is relatively uniform in depth of influence over this area [36, 39].

Galvanic corrosion basically occurs between different metals or between different areas of the same metal when in electrical contact with each other. The galvanic corrosion attacks the anodic member.

Pitting corrosion is limited to a small area of the surface defined by holes or "cavities" that are formed in the material. Since the smaller area can be described as anodic and the larger surrounding area described as cathodic, a reaction between the two takes place, resulting in pitting on the surface of the corrosion specimen. The damage caused by pitting corrosion is more of a problem than uniform corrosion because it is more complicated to predict, detect, and design against [40].

Crevice corrosion occurs when there is an electrolyte at the faying surface of a joint. The term "crevice corrosion" explains the position of the attack rather than a form of corrosive action. Also, other types of corrosion, such as pitting corrosion, may be taking place at the faying surface [3].

Intergranular corrosion is a localized form of corrosion occurring at the grain boundaries of the material. This form of corrosion is normally associated with specific phases precipitated on the grain boundaries or chemical segregation effects. In this process, the grains act as a cathode in contact with the grain boundary that acts as an anode. Thus, a specific form of galvanic corrosion occurs [40].

Exfoliation corrosion is a particular form of intergranular corrosion that is associated with very high-strength aluminum alloys. Those type of alloys that have been worked heavily or extruded, with a microstructure of elongated, flattened grains, are particularly prone to this damage. Corrosion products building up along these grain boundaries apply pressure between them, and the end result is a lifting or leafing effect. The damage frequently initiates at end grains encountered in machined edges, holes, or grooves and as a result can progress through an entire section [41].

Stress corrosion cracking is the result of interaction between stress and corrosive reactions. These stresses could be either applied externally or exist as residual stresses. Stress corrosion cracking may explain any crack propagation that is assisted by the environment [42].

2.8 Aluminum Alloys

2.8.1 General Information

Aluminum can be described as having a silver-white surface color, with a sheen that can vary greatly from dull to shiny. This non-ferrous metal alloy has very good corrosion resistance

when compared to other metals. With a specific gravity of 2.7 lb/ft^3, these metal alloys are often lighter than metals with comparable properties, such as copper, steel, and nickel. Aluminum alloys also have very good machinability, workability, and thermal and electrical properties. The typical alloying elements are manganese, silicon, copper, and zinc. Aluminum alloys having a wide range of properties are used in many engineering structures in the aerospace and automotive industries due to their high strength-to-weight ratio. For example, they are widely used inside automotive engines like crankcases and cylinder blocks. In addition, stiffer and lighter designs can be achieved with aluminum alloys rather than other alloys like steels [44, 45].

2.8.2 Characteristics

The characteristics of aluminum alloys can vary greatly depending on the type of alloy. In general, precipitation-strengthened aluminum alloys subjected to extremely high temperatures, typically between 200°C and 250°C, tend to lose a percentage of their strength. The opposite occurs at subzero temperatures—their strength increases while there is no noticeable change in their ductility. This makes aluminum an extremely useful low-temperature alloy. Aluminum alloys have a strong resistance to corrosion, which is the result of a stable oxide skin that forms as a result of reactions with the atmosphere. This corrosive skin is impervious to most chemicals, weathering conditions, and even many acids, thus protecting the aluminum that it encompasses. However, these alkaline substances are known to penetrate the protective skin and corrode the metal [44, 45].

Although copper has an electrical conductivity of approximately 161% of aluminum, aluminum is still a very valuable material in terms of electrical conductivity. The electrical properties of aluminum make it a good cost-efficient replacement for building wire. One

problem, however, is the fact that aluminum connectors become loose after repeated use. This sometimes results in arcs or fires [45].

Aluminum is a very versatile metal and can be cast in any known form. It can be rolled, stamped, drawn, spun, roll-formed, hammered, and forged. The metal can be extruded into a variety of shapes, and can be turned, milled, and bored in the machining process. It can also be riveted, welded, brazed, or resin-bonded. For most applications, aluminum needs no protective coating because it can be finished to look good; however, it is often anodized to improve color and strength [44, 45].

2.8.3 Classification

Basically the classification of aluminum alloys is based on their available strengthening mechanisms. The International Alloy Designation System is the most widely accepted naming scheme for wrought alloys. Each alloy is given a four-digit number, where the first digit indicates the major alloying elements, as shown in the sections that follow [44, 45, 46, 47].

2.8.3.1 AA 1xxx Series

The AA 1xxx series denotes a pure aluminum alloy with a minimum 99% aluminum content by weight. This alloy can be work hardened. In comparison to the other alloy series, it has a lower strength, easier plastic deformation leading to very high formability, superior corrosion resistance, highly reflective and decorative character, and very high thermal and electrical conductivities. The combination of different mechanical properties make 1xxx aluminum alloys a very good option for applications such as packaging (food containers), electrical devices (high conductivity for electrical cables, dielectric oxide layer for capacitors), heating equipment (radiator tubes, heat exchanger strip), decoration (design appearance and high reflectivity for furniture fitting), and lighting (laser mirrors).

2.8.3.2 AA 2xxx Series

AA 2xxx series alloys are generally alloyed with copper. They can be precipitation hardened and have shown strengths comparable to steel. Also known as duralumin, this series was once the more predominate aerospace alloy. However, this series is susceptible to stress corrosion cracking and is increasingly replaced by the 7000 series in new designs. In general, 2xxx series alloys have spot weldability, good corrosion resistance, and sufficient formability. They are used primarily for high-strength applications such as aircraft fittings and wheels, and forgings for trucks, bridges, and military vehicles. They are also used for hard-extruded and machined-part applications such as bolts, screws, machinery components, and fittings.

2.8.3.3 AA 3xxx Series

AA 3xxx series alloys are medium-strength alloys that are alloyed with manganese (range 1–2 wt%). They can be work hardened. Manganese makes the alloys ductile, resulting in decent formability, while the mechanical properties still remain in a wide range through various strain-hardened tempers. They have a good combination of formability and strength properties, anodizing behavior, weldability, and corrosion resistance. They can be used in roll forming, drawing, packaging, building (architectural sheet), and home appliance applications. They are also used in heating equipment such a heating tubes and brazing sheet. The high thermal conductivity, medium strength, and good corrosion resistance allows 3xxx series aluminum alloys to perform very well.

2.8.3.4 AA 4xxx Series

AA 4xxx series alloys are known as silumin, since they are alloyed with silicon and have low ductility properties as well as very low formability. They are mostly used in casting products where lower ductility and higher rigidity is required. AA 4xxx series alloys are widely used in

the foundry industry because of their high fluidity while casting. Also, the added silicon decreases the amount of shrinkage during freezing and the coefficient of thermal expansion of the cast product. The higher level of silicon causes lower ductility in these alloys.

2.8.3.5 AA 5xxx Series

AA 5xxx series alloys use magnesium as the alloying element (up to 6 wt%), which causes solute hardening of the alloy and an increase in strength. This series derives most of its strength from work hardening and is well suited for cryogenic applications due to low thermal conductivity. In general, the medium strength of this series is stronger than AA 3xxx series alloys. A combination of favorable properties such as good formability, medium strength, excellent corrosion resistance, high anodizing ability, and weldability make these alloys very popular for the following outdoor exposure applications: scaffolding, marine applications such as platforms and shipbuilding, and press-formed body parts and chassis components in the automotive industry.

2.8.3.6 AA 6xxx Series

AA 6xxx series alloys have very good machinability, formability, and weldability. They are alloyed with magnesium and silicon (mostly in the range 0.3–1.5 wt% Si and Mg), and can be precipitation hardened by heat treatment. The strengths are not as high as the 2xxx and 7xxx series alloys, but still they have high-strength properties. Due to their decent combination of corrosion resistance, formability, high strength, and weldability, AA 6xxx series alloys are used in a vast variety of applications in industries such as transportation (railcars, automotive outer-body panels), marine (offshore structures), building (ladders, doors, windows), and heating (brazing sheets). AA 6xxx series extrusion alloys are used for machined products by adding elements like lead and bismuth, which are low-melting phase elements, because their restricted

solubility in aluminum forms a soft, low-melting phase that alleviates chip breaking and aids in tool lubrication.

2.8.3.7 AA 7xxx Series

AA 7xxx series alloys can be precipitant hardened to exceed any other aluminum alloy. They are alloyed using zinc (mostly in the range of 4–6 wt%) and magnesium (1–3 wt%). They are heat treatable and can be strengthened in this way. These alloys do not have a good corrosion resistance and mostly tend to stress corrosion. They are used in aerospace, space exploration, nuclear, military, building structures, and sport attributes applications due to their high superior strength. The addition of magnesium to AA 7xxx series alloys causes them to maximize their age-hardening potential, which provides medium strength but easy weldability.

2.8.3.8 AA 8xxx Series

The AA 8xxx series generally denotes lithium-alloyed alloys. Lithium has a lower density and higher solubility than aluminum, and by using this element in aluminum, the fatigue crack growth increases at intermediate stress levels. Due to the attractive combination of 8xxx series properties, these alloys have become of considerable interest in aerospace applications. They are also used as foils and closures as well as heat-exchanger fin stock. Alloys in the 8xxx series, such as AA8280 and AA8081, are bearing alloys, which are used in truck and car applications.

2.9 Aluminum Alloy 6082 (AA6082)

Aluminum alloy 6082 is a precipitation-strengthened alloy (.1 Si–0.65 Mg–0.2 Fe–0.52 Mn), with a high manganese content to increase ductility. The results of fusion welding in AA6082 show a significant loss of mechanical properties. Due in part to its alloyed elements,

AA6082 is one of the high-strength Al-Mg-Si alloys with a decent toughness. Its chemistry is shown in Table 2.1 [49].

Table 2.1. Chemical Composition of AA6082 [49]

Chemical Composition Limits (Component Wt. %)									
Silicon	Iron	Copper	Manganese	Magnesium	Chromium	Zinc	Titanium	Aluminum	Others
0.7-1.3	0.5	0.1	0.4-0.1	0.6-0.1	0.25	0.2	0.1	95.2-98.3	0.15

Hardness properties for friction stir-welded AA6082 in T4, T5, and T6 tempers can be found in a number of publications. The hardness profile conducted by Karlsson et al. on 0.2-in.-thick AA6082-T6 shows the characteristic "W"-shaped curve with the minimum amount of hardness in the HAZ, which is 45% less than the parent material hardness. Hardness in the nugget zone is a little higher, with 36% reduction compared to the base metal hardness (see Figure 2.17) [1, 48].

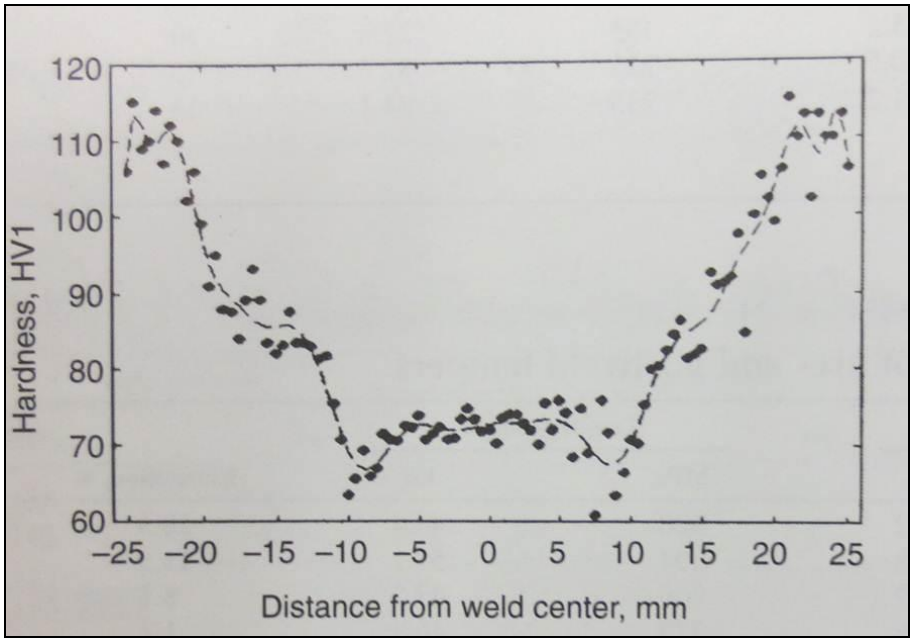

Figure 2.17. Hardness profile across FSW AA6082-T6 [1, 48].

Ericsson et al. conducted a study of the mechanical properties, such as hardness, in 0.23-in.-thick FSW AA6082 in different temper conditions. Optimized weld parameters of 1,000 rpm,

13.8 ipm, and 0.79-in. shoulder diameter were selected. For the as-welded T6 condition, the hardness profile across the joint was basically the same as shown in Figure 2.17, which indicated no difference between the HAZ and the base material. Fatigue testing and tensile testing were also conducted and the results compared for two conditions (T4 and T6), but the authors never published their results. The ultimate tensile strength and yield strength obtained higher values in the T4 condition (post-weld treatment) in comparison to the T6 condition (as-welded). Fatigue testing was conducted in the form of S-N curves with a ratio of 0.5 and a range of 10^5–10^7 cycles. The as-welded T6 coupons resulted in higher fatigue strengths than the T4 coupons with post-weld treatment [21, 50].

Mroczka and Pietras found that the application of the FSW technique allowed for good-quality welds of the AA6082-T6 at 710 rpm and 244–900 mm/min. Also, the welds for AA6082-T6 obtained by FSW retained plastic properties of the matrix material as confirmed by the ductile fracture of broken tensile samples [52]. Larsson et al. showed that FSW may help to retain the high mechanical properties of the AA6082-T6 alloy in the final product [53]. Also, a number of research studies for a variety of tempers for different thickness were undertaken to determine the mechanical properties of AA6082, as shown in Table 2.2. However, considering different weld procedures, natural aging times, tool design, material thickness, and thermal boundary condition, the mechanical properties were found to be almost the same [1]. AA6082 sheet and plate materials have a wide array of applications in the aircraft and automotive industries where high-stress applications are required. A few of these applications include trusses, bridges, cranes, transport applications, ore skips, beer barrels, and milk churns. They can also be used in supplied forms such as square bars, square box sections, rectangular box sections, channels, tee sections, equal angles, unequal angles, flat bars, tubes, and sheets.

Table 2.2. Tensile Properties of FSW AA6082 for Pre- and Post-Weld Tempers [1]

Temper	Postweld age	Yield strength		Tensile strength		Elongation, %	Thickness		Ref
		MPa	ksi	MPa	ksi		mm	in.	
Base T4	...	149	21.6	260	37.7	22.9	4	0.16	61
Base T6	...	291	42.2	303	43.9	11.3	4	0.16	61
MIG T4(a)	...	129	18.7	163	23.6	3	5	0.20	65
Friction stir welded									
T6	...	...	...	226	32.8	...	10	0.39	32
T6	...	...	...	254	36.8	...	5	0.20	32
T6	...	135	19.6	220	31.9	...	5.8	0.23	64
T6	...	160	23.2	254	36.8	4.9	4	0.16	61
T6	185 °C (365 °F) for 3 h	274	39.7	300	43.5	6.4	4	0.16	61
T5	...	125	18.1	198	28.7	7.8	3.5	0.14	60
T5	...	125	18.1	196	28.4	9.8	3	0.12	62
T4	...	144	20.9	239	34.7	...	5	0.20	65
T4	...	138	20.0	244	35.4	18.8	4	0.16	61
T4	185 °C (365 °F) 3 h	221	32.1	246	35.7	5.7	3.5	0.14	60
T4	185 °C (365 °F) 3 h	285	41.3	310	45.0	9.9	4	0.16	61
T4	185 °C (365 °F) 3 h	260	37.7	289	41.9	...	5.8	0.23	64
T4	185 °C (365 °F) 3 h	227	32.9	250	36.3	7.6	3	0.12	62

2.10 Aluminum Alloy 6063 (AA6063)

Aluminum alloy 6063 is one of the most-used 6xxx series aluminum alloys. Also known as the Japanese alloy, it has excellent welding characteristics in all tempers and is used in road transportation, rail transportation, and extreme sports equipment. It is typically used in architectural applications, extrusions, window frames, doors, shop fittings, and irrigation tubing. The chemical composition of AA6063-T6 is provided in Table 2.3.

Table 2.3. Chemical Composition of AA6063-T6 [49]

Chemical Composition Limits (Component Wt. %)										
Component	Silicon	Iron	Copper	Manganese	Magnesium	Chromium	Zinc	Titanium	Aluminum	Others
AA6063-T6	0.2-0.6	0.35	0.1	0.1	0.45-0.9	0.1	0.1	0.1	98.9	0.15

Singh et al. investigated the mechanical properties of 6-mm-thick FSW AA6063-T6. The results of this tensile testing showed lower properties and lower elongation for FSW AA6063-T6 than its base material, but these were still much better than other conventional methods such as fusion welding. The joint efficiency, or ratio of tensile strength of the FSW joint to the parent material tensile strength, was about 69% [51].

Moreira et al. found that for FSWAA6063-T6 joints, hardness drastically decreased in the weld zone, as shown in Figure 2.18. An increase in the hardness profile was identified at the side surface due to the different grain-size diameters [54]. The tensile strength properties decreased during the welding process. Yield and rupture stress were determined to be lower values for FSW specimens than unwelded specimens. Also, the welded specimens presented longer fatigue lives for all stress levels (see Figure 2.19) [53].

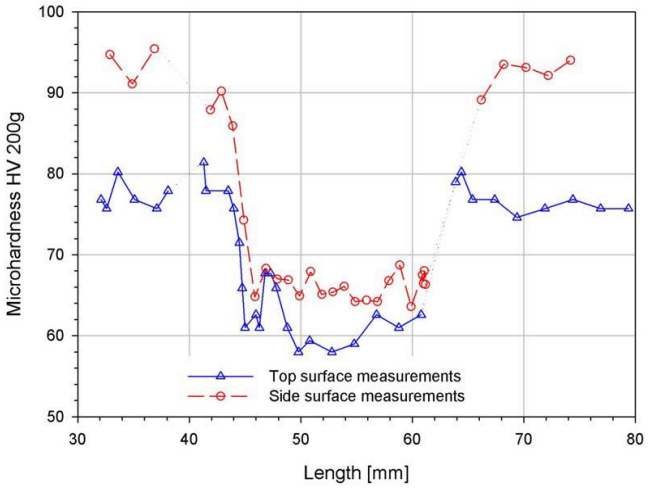

Figure 2.18. Hardness profile across FSW AA6063-T6 [54].

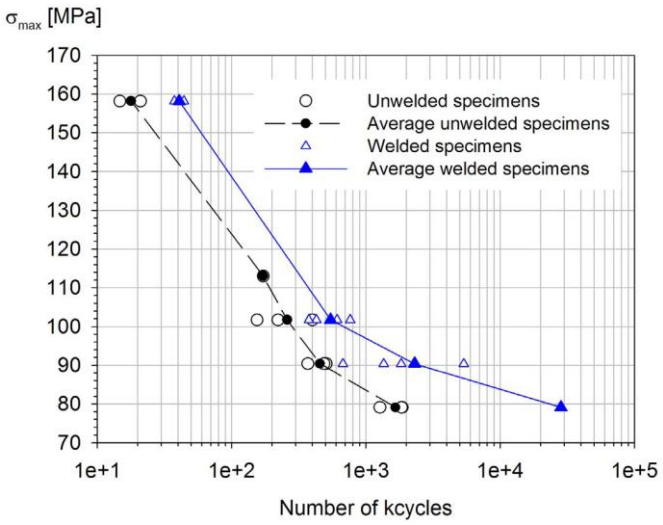

Figure 2.19. Fatigue testing results of FSW AA6063-T6 compared to unwelded specimens [54].

2.11 Applications

Currently there are many instances of friction stir welding being used in several industries, including the aerospace and automotive industries. In 1995, FSW was introduced to the U.S. market and since then has been developed a great deal. The technology readiness level for FSW of aluminum alloys is high, with successful industrial implementations. As development efforts and property characterizations have shown, FSW can be used to process iron, stainless steel, nickel, copper, and titanium alloys [9, 10].

The metalworking nature of the FSW process has led to plunge and refill FSSW methods, with properties comparable to riveted and resistance spot-welded joints. Many applications today rely on friction stir processing of already joined materials via welds or castings. By modifying the microstructure by FSP, a weld can have increased strength and improved fatigue life, and also remove unwanted defects. FSP can be successfully used to create and join new material or combinations of surfaces. Using FSP to stir particulate materials into the surface has shown increased wear resistance by creating particulate-reinforced surface layers [9, 10].

The environmentally friendly and cost-effective FSW process has been shown to reduce costs in a wide variety of applications, as shown in Figures 2.21 to 2.24. Since this process does not involve a phase change while joining metals and also produces a higher-strength joint, this application has enabled the formation of new products. A variety of government, university, and industry collaboration projects are underway to accelerate the implementation of FSW into new productions [9, 10].

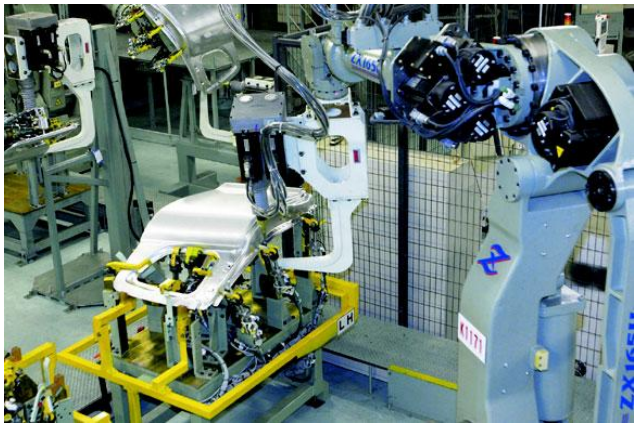

Figure 2.20. Weld being made by Mazda's new friction stir welder on body assembly [54].

Figure 2.21. Eclipse 500 business-class jet with FSW lap joint [9].

Figure 2.22. Mazda RX-8 with FSSW on door [55, 56].

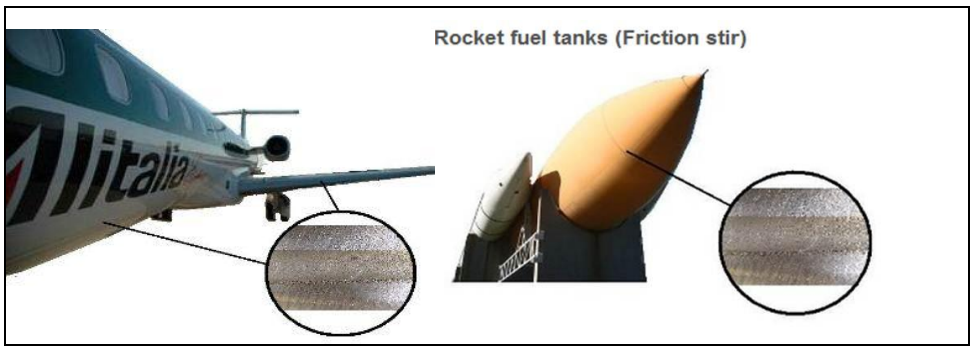

Figure 2.23. FSW aircraft paneling (left), and FSW rocket fuel tank (right) [57].

During the last decade, the defense and aerospace sectors have taken the lead in implementing FSW. Due in part to recent advances in tool designs and optimizing parameters for specific materials, many FSW and FSSW applications in the marine and transportation industries have excelled. Further development of low-cost equipment, industrial standards, and a trained work force will allow FSW to be implemented by a broader industry [9, 10].

CHAPTER 3

OBJECTIVES AND METHODS

3.1 Objectives

Advancements in weld tool and joint designs for friction stir welding have enabled the development and testing of a lightweight automotive bumper-beam/crash-box assembly. Advancements were used previously in the development of a test fixture to dynamically (crash) test the functionality of the advanced bumper assemblies fabricated by FSW. In addition to drop tower testing, assemblies fabricated with both FSW and GMAW were subjected to crash sled testing at General Motors (GM) to provide a comparison in performance under dynamic loading conditions. That FSW development work included microstructural examination and static mechanical testing. Results from coupon-level development were compared against results from component-level testing of prototype articles using micrographs and an advanced electronic (signal/frequency analysis) non-destructive evaluation technique in order to detect weld anomalies primarily in the form of voids. Due to the geometry of the welded part joint, conventional mechanical testing methods (tensile and peel test) were not applicable. Therefore, a wedge test was devised to test the relative toughness of the FSW joint. From recorded data, toughness plots were calculated to evaluate and select the best joint from three weld tools, each having the same basic threaded probe and Wiper™ shoulder designs. The tools differed only in probe features. In addition to the base configuration tool, the second tool had a set of partial CounterFlow™ grooves, and the third tool had a set of partial straight flats. Each tool also had a special geometrical feature added to the tip of the tool probe, referred to as a concentrating tip, to improve metal flow at the end of the probe in order to inhibit void formation. Traditional sled testing for low-speed bumper requirements was performed at the GM research and development

(R&D) facility in Detroit, Michigan, and drop tower tests were performed using an FSW test fixture in the Dynamic Impact Laboratory of the National Institute for Aviation Research (NIAR) at Wichita State University (WSU) in Wichita, Kansas. These dynamic tests were performed using both FSW and gas metal arc-welded (GMAW) bumpers. An analysis of the collected data gathered from both sled and drop tower tests is reviewed in this study. A validated finite element analysis (FEA) was used to compare the predicted damage to the actual damage sustained by the bumpers fabricated by GMAW and FSW, respectively. It is assumed that the crash behavior of this model represents the same behavior of the testing of the parts in reality.

In general, the objectives of this study, also shown in Figure 3.1, are as follows:

- FSW development of AA6082-T6 and AA6063-T6 in lap weld and butt weld configurations for 3.5-mm-thick aluminum sheets (coupon level) through a design of experiments (DOE) process.
  - ✓ Microstructural examination and static mechanical testing.
  - ✓ e-NDE testing.
- Conduction of component level (bumper and crash box) testing using results from the previous step.
  - ✓ Microstructural examination and static mechanical testing.
  - ✓ e-NDE testing.
- Evaluation of the proper FSW pin tool for either butt or lap joints.
- Gas metal arc weldong some of the crash boxes and bumpers together for comparison purposes.
- Impact crash dynamic testing of FSW and GMAW crash boxes and bumpers for comparison purposes.

- ✓ Sled testing.
- ✓ Drop tower testing.

- Finite element analysis of FSW parts.

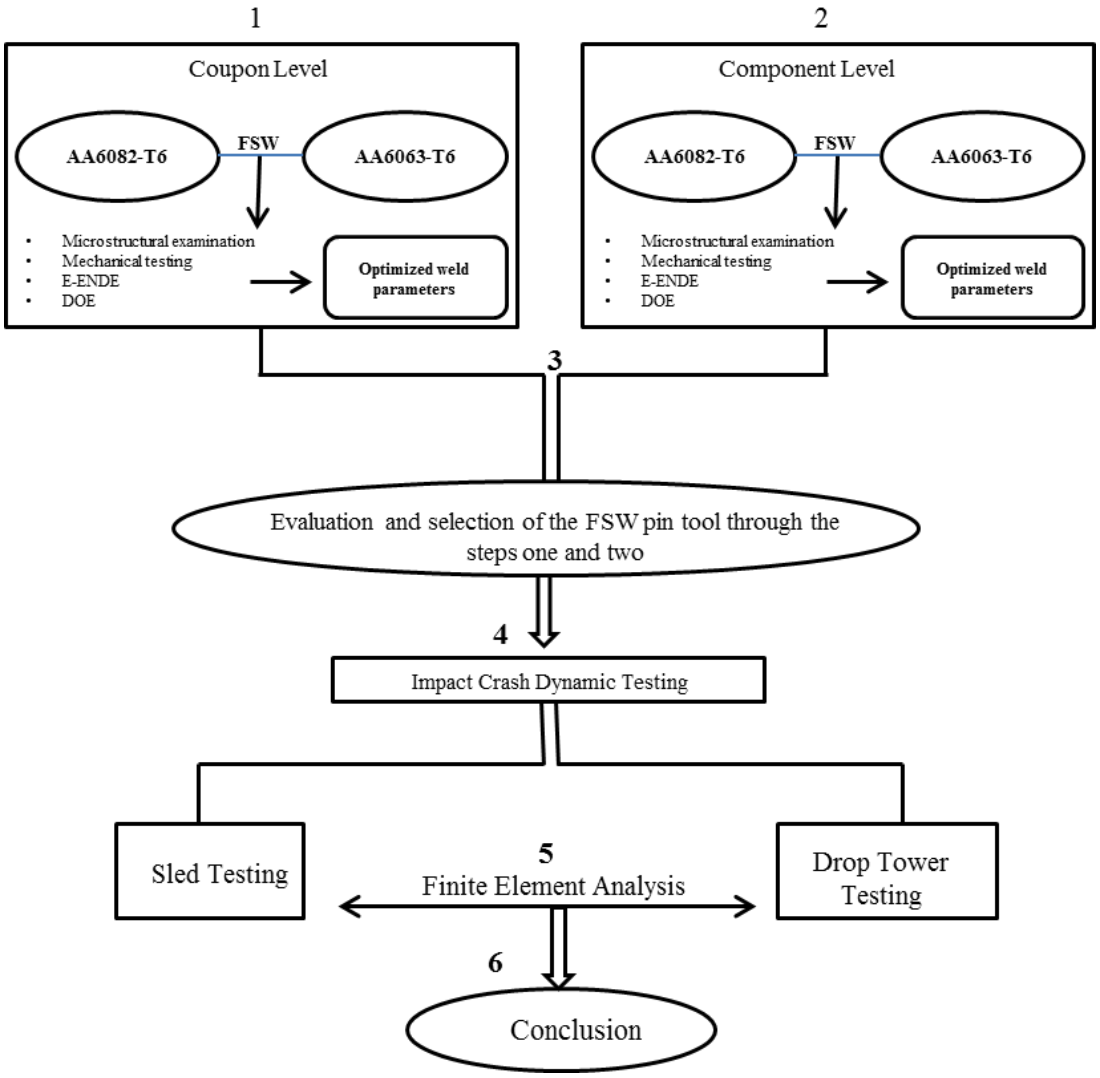

Figure 3.1. Diagram of project objectives.

3.2 General Welding Practices

The welding of all coupons took place in NIAR's Advanced Joining and Processing Lab (AJPL) at WSU. The discontinuous friction stir welds were carried out on a five-axis MTS I-Stir™ Process Development System (PDS) to perform the complex movement in the lap and

linear welds, as shown in Figure 3.2. All clamps were torqued to 54.2 N-m (40 ft.lbs.), and 180-grit sand paper was used to clean the oxide film on the sheets before being clamped. A methyl ethyl ketone (MEK) wipe was used for cleaning the workpiece.

Figure 3.2. Five-axis MTS I-Stir™ PDS machine at Wichita State University.

The next three chapters provide a detailed discussion of the DOE for the coupon-level and component level studies. These chapters were submitted in 2011 and 2012 as conference papers at the friction stir welding conferences of The Minerals, Metals & Materials Society (TMS) and The Welding Institute.

CHAPTER 4

MICROSTRUCTURAL AND MECHANICAL PROPERTIES OF FRICTION STIR WELDED JOINTS OF AA6082-T6 WITH AA6063-T6*

4.1 Introduction

This chapter discusses the investigation of microstructure and mechanical properties of friction stir-welded butt joints in a AA6082-T6 and AA6063-T6 coupons. To perform the study, a modified Tri-Flute™ FSW tool was designed and used to fabricate coupons for developing optimized process parameters through the DOE methodology. Once an optimized set of processed parameters was identified, 3.5-mm-thick sheets of each alloy were friction stir welded for the investigation. In this study, the capability of FSW to join dissimilar alloys using a butt weld configuration was investigated. The mechanical and metallurgical characterization of friction stir welds between aluminum alloys 6082-T6 and 6063-T6 was carried out. For comparison, three different post-weld conditions (as-welded, naturally aged, and heat-treated) of AA6063-T6 parent material were investigated and compared with AA6082-T6, which has less strength. This work included microstructure examination, microhardness testing, tensile testing of the butt joints, and feedback signal analysis. In addition, the weld tool feedback forces, in particular drag force and transverse force, were studied using the e-NDE software package that is being developed by the AJPL at WSU. Also, e-NDE was used for detecting weld anomalies primarily in the form of voids.

---

*The contents of this chapter was published entirely in 2011 as "Microstructural and Mechanical Properties of Friction Stir Welding Joints of AA6082-T6 with AA6063-T6" in *Friction Stir Welding and Processing VI*, The Minerals, Metals and Materials Society. The literature review part of this paper has been merged into the Literature Review section in Chapter 2 of this dissertation.

4.2 Methodology

4.2.1 Experimental and Welding Procedures

AA6082-T6 and AA6063-T6 are high-strength Al-Mg-Si alloys that have manganese added to increase some of the mechanical properties, such as toughness and ductility. The chemical composition for both aluminum alloys is shown in Table 4.1.Welding was carried out on a five-axis MTS I-Stir™ PDS at NIAR. Friction stir welds in 3.5-mm-thick plates were performed along the grain direction. Each alloy was welded in the T6 condition. The weld parameters in this study were developed based on DOE methodology using Statgraphics™, a statistics software package.

Table 4.1. Chemical Composition (%) of AA6063-T6 and AA6082-T6 [6- 58]

Component	**Component Weight (%)**	
	AA6063-T6	**AA6082-T6**
Silicon	0.2–0.6	0.7–1.3
Iron	0.35	0.5
Copper	0.1	0.1
Manganese	0.1	0.4–0.1
Magnesium	0.45–0.9	0.6–0.1
Chromium	0.1	0.25
Zinc	0.1	0.2
Titanium	0.1	0.1
Others	0.15	0.15
Aluminum	98.9	95.2–98.3

This study used the following techniques: (1) visual inspection to analyze the weld surface, (2) macrographs to investigate defects, and (3) tensile tests to optimize the mechanical properties. Selected weld parameters included a rotation speed of 1,000 rpm, travel speed of 317 mm/min, and tilt angle (lead angle) of 1°. The AA6082-T6 material was placed along the advancing side of the weld, and AA6063-T6 material was placed along the retreating side of the weld. The weld tool, shown in Figure 4.1, had the following geometry: right-hand (RH) threads

and RH twisted flats, flat shoulder diameter of 10.16 mm, pin length of 3.25 mm, and probe diameter at the base of the shoulder of 3.9 mm.

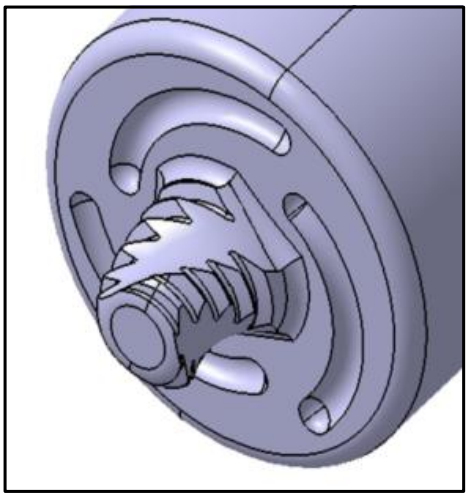

Figure 4.1. Pin tool configuration with right-hand threads and right-hand twisted flats.

Specimens 3.5 mm in thickness were prepared transverse to the weld direction by following ASTM B557 [59] to measure the ultimate tensile stress (UTS) of the welded specimens and parent material. A 370 MTS servo-hydraulic load frame with 50-mm gage length and 1.3-mm/min cross-head speed was used for the mechanical testing. The overall length of the specimen was 200 mm, the nominal width of the grip section was 20 mm, the nominal length of the reduced section was 60 mm, and its width was 12.5 mm. The entire specimen was profiled using a TensileKut™ machine. Microhardness maps provided an understanding of the mechanical as well as microstructural properties of the weld by characterizing the hardness profile in the vicinity of the different zones of the weld cross section (e.g., heat-affected zone). Specifically, microhardness tests were performed on cross sections of selected welds perpendicular to the weld line direction and in rows along the bottom, middle, and top sections across the weld zone by using a Leco AMH43 automatic microhardness tester with a Vickers scale of 500-gf load, 13-second dwell, and 550-micron spacing.

4.2.2 Feedback Signal Analysis

In FSW, time series data of the tool feedback forces can be used for characterizing the physical interactions between the material flow and the weld tool [8]. While feedback signals might be distorted by FSW machine-dependent noises, the indications of stable and/or erroneous material flow have been found to be retained in the time series data of the feedback forces [8]. In this study, feedback force signals, including drag force and transverse force, were captured during each welding experiment at the sampling rate of at least 3.5 times the tool spindle speed. Afterwards, the captured signals were analyzed using the e-NDE software described in the work of Burford et al. [7] and Boldsaikhan et al. [8].

4.3 Results and Discussions

4.3.1 Tensile Test

The tensile test results of welded and parent material specimens are presented in Figure 4.2, and Table 4.2 presents the average value of ultimate tensile stress and standard deviation for FSW specimens as well as parent material for each test set (three specimens each).

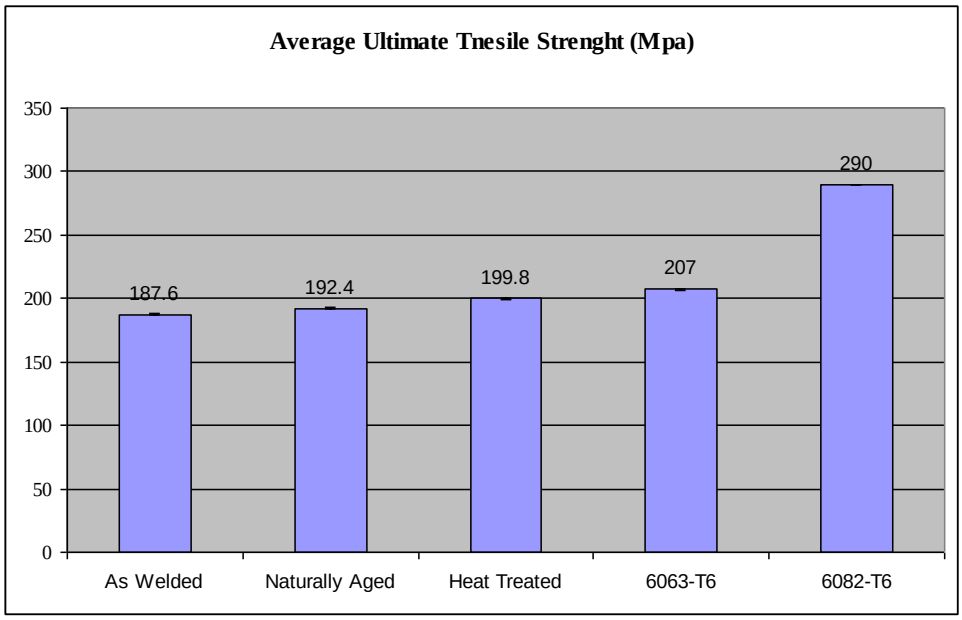

Figure 4.2. Average ultimate tensile strength for welded material and parent material specimens.

Table 4.2. Material Properties and Tensile Test Results for FSW Specimens [61].

FSW	UTS (Mpa)	Standard Deviation	Elongation (%)	Joint Efficiency (%)	
As-Welded	187.6	0.16	2.3	91 (6063-T6)	64.7 (6082-T6)
Naturally Aged	192.4	0.22	2.1	93 (6063-T6)	66.4 (6082-T6)
Heat-Treated	199.8	0.12	1.5	97 (6063-T6)	70 (6082-T6)
AA6082-T6 Parent Material	290	0.13	10.5	-	-
AA6063-T6 Parent Material	207	0.21	12	-	-

As indicated previously, results are shown for three specimen conditions: as-welded, naturally aged, and heat-treated. As-welded specimens were tested one day after the welding process was completed, whereas the naturally aged specimens were left at room temperature for 120 hours before testing. Heat-treated specimens were obtained by artificial aging at approximately 180°C for 6 hours to produce roughly a T6 temper in the stir zone [60]. The highest UTS was observed in the parent material specimens for AA6082-T6, followed by AA6063-T6. For welded specimens, it was observed that dissimilar joints resulted in more than 90% joint efficiency relative to the AA6063-T6 parent material, meaning that this UTS was very close to the UTS of AA6063-T6 parent material. Considering joint efficiency as the ratio of the UTS of welded joints divided by the UTS of the base material, all three conditions were analyzed. These results are also shown in Table 4.2. Joint efficiency for the as-welded, naturally aged, and heat-treated specimens was 91%, 93%, and 97%, respectively.

4.3.2 Microhardness

A Vickers hardness profile for one of the FSW specimens is presented in Figure 4.3. The hardness for AA6063-T6 parent material was lower than the hardness for AA6082-T6 parent material. A hardness decrease was observed closest to the nugget. The average hardness of the three rows (bottom, middle, and top) was significantly lower than the hardness of the parent material in the dissimilar butt welded joints, due to the variation of the microstructures between the weld zone and parent material.

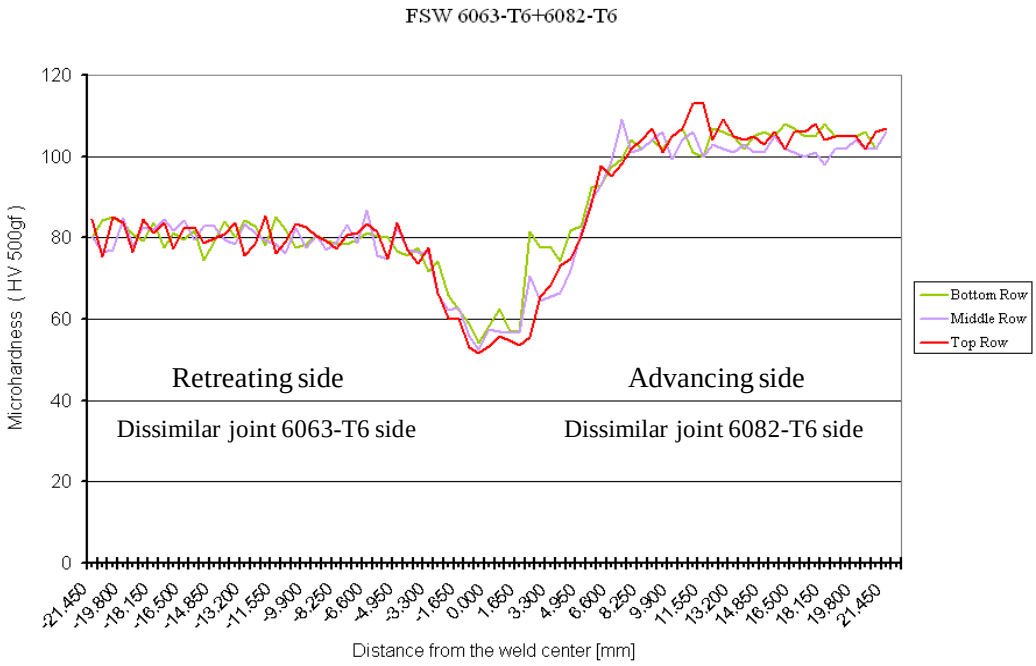

Figure 4.3. Microhardness profile of FSW specimens (data obtained at bottom, middle, and top rows of cross section taken perpendicular to weld line).

As can be seen, Figure 4.3 shows the microhardness results obtained in the AA6063-T6 + AA6082-T6 weld zone. The lower value of the hardness was observed in the AA6063-T6 alloy plate where the retreating side is located. The fracture surface for tensile specimens was coincident with this zone due to the lower value of the hardness, whereas in some of the similar published works, it was found that a zone outside of the nugget, called the thermomechanically affected zone, is where the lowest value of hardness occurred. Moreira et al. found that hardness is always higher in the nugget area than in the transition area between the TMAZ and the HAZ [54, 62].

4.3.3 Metallographic Analysis

Figure 4.4 shows the macrostructure of a friction stir weld of a dissimilar joint alloy. In the macrostructure profile, some important weld joint regions, including the nugget, TMAZ, and HAZ, are identified. Additional elements include the deformed grains or swirl marks underneath

the shoulder, identification of the advancing and retreating sides, weld flash, and onion ring pattern (nugget). The onion ring pattern essentially represents the banded microstructure brought together by the stirring action of the pin. In the TMAZ, grain growth and plastic deformation without recrystallization occurs, and there is a distinct boundary between the TMAZ and weld nugget. The HAZ is only affected by the heat generated during the welding process. In the HAZ, there may be slight grain growth, but there is no plastic deformation [12].

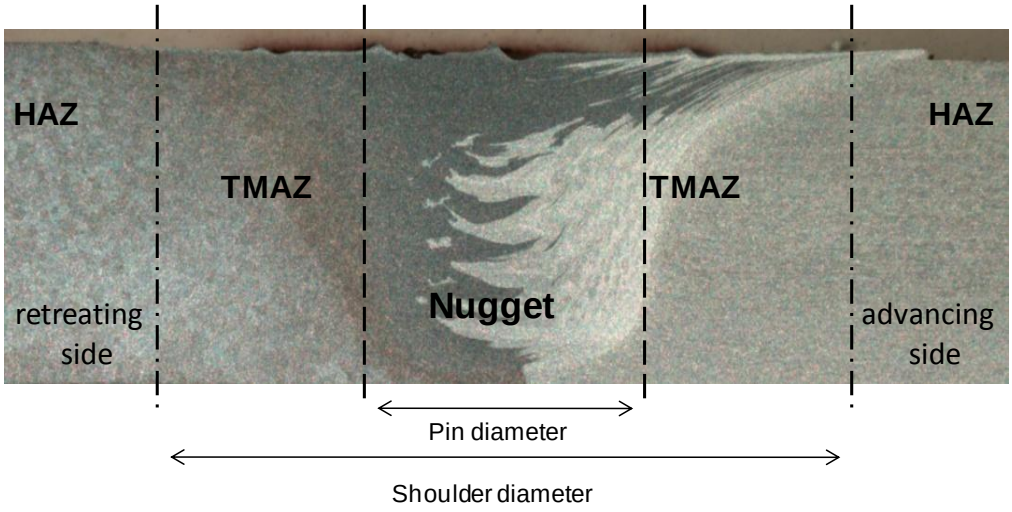

Figure 4.4. Macrostructure of dissimilar weld.

As can be seen in Figure 4.4, the left-hand side of the macrostructure is the retreating side where AA6063-T6 is located and more flash is typically observed. The level of hardness in this zone is lower than the advancing side. The right-hand side of the macrostructure is the advancing side where AA6082-T6 is located, and less flash and higher hardness were obtained in this zone. The mixture and material flow of the two dissimilar alloys are shown in the nugget or stir zone of the weld.

4.3.4 Results of Feedback Signal Analysis

According to the analysis, the oscillations of feedback forces were evidently changed as the process heat input decreased from “hot” conditions (low travel speed and high tool rotational

speed) to "cold" conditions (high travel speed and low tool rotational speed). The "cold" welding condition makes the material less plasticized and helps the joint retain its parent material strengths [7]. However, if the heat input becomes too cold, the welding process may result in lack-of-fill defects, as shown in Figure 4.5.

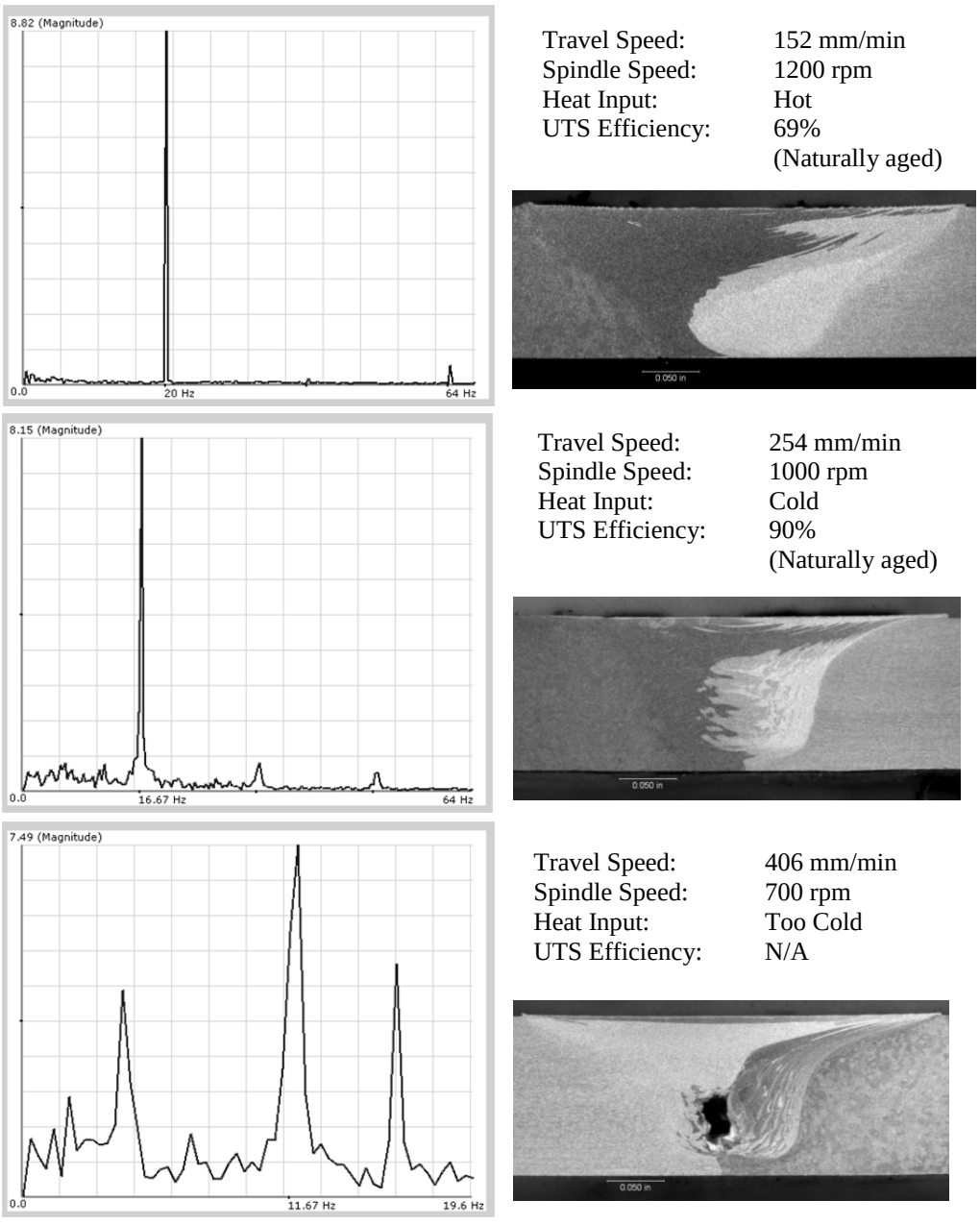

Figure 4.5. Frequency spectra of transverse force feedback (oscillations of transverse force change as process heat input drops off from "hot" condition to "cold" conditions; the highest peak of each frequency spectrum corresponds to spindle frequency oscillation).

4.4 Conclusion

Friction stir butt weld joints between AA6082-T6 and AA6063-T6 were produced through optimized weld parameter results of a DOE process. FSW joints of the dissimilar material showed lower ultimate stress properties compared to the parent material of both alloys. In tensile tests, failure occurred in the nugget of the weld where the minimum amount of hardness was observed. Also, according to the joint's hardness profile, the lowest value was obtained in the center of the weld zone (nugget), corresponding to location of the failure when tensile testing the dissimilar butt weld joints. The joint efficiency for T6 heat-treated specimens increased 4% over naturally aged specimens and 6% over as-welded specimens, and is a marked improvement over that found in other published papers that were reviewed [53]. Microstructural properties and dissimilar joint analysis, including the material flow and mixture of the two alloys, was clearly identified. The oscillations of the feedback forces were changed as the process heat input decreased, which provides evidence that the feedback forces can be used for evaluating mechanical and metallurgical qualities of welded joints.

CHAPTER 5

FRICTION STIR LAP WELDS OF DISSIMILAR ALUMINUM ALLOYS OF AA6082-T6 WITH AA6063-T6*

5.1 Introduction

An investigation of the microstructure and mechanical properties of friction stir-welded lap joints between AA6082-T6 with AA6063-T6 was carried out because of the similarity of this combination of alloys in automotive industry applications. To perform the study, a modified FSW tool with right-hand threads and left-hand CounterFlow™ flats was designed and used to fabricate coupons for developing optimized process parameters through DOE methodology. Once an optimized set of processed parameters was identified, 3.5-mm-thick sheets of each alloy were friction stir lap welded for the investigation. The FSW development work included microstructural examination, microhardness testing, lap shear testing, and the e-NDE technique in order to detect weld anomalies primarily in the form of voids. For comparison purposes, specimens were tested at the following conditions: as-welded, naturally aged, and post-weld heat-treated. The finite element model (FEM) created was used to verify the types of displacements seen in lap shear testing of friction stir welds in a lap joint configuration as well as to examine the distribution of stresses in the weld region during lap shear testing.

5.2 Methodology

5.2.1 Experimental and Welding Procedures

Dissimilar friction stir lap welds were produced in aluminum sheets of AA6082-T6 and AA6063-T6 as the top and bottom sheets, respectively, of the lap joints. This decision was made

---

*The content of this chapter is to be published as "Friction Stir Lap Welds of Dissimilar Aluminum Alloys of AA6082-T6 with AA6063-T6" in *Science and Technology of Welding and Joining*. The literature review part of this paper has been merged into the Literature Review section in Chapter 2 of this dissertation.

based on the geometry of a previous case study regarding friction stir welding an aluminum crash box to an aluminum bumper [63]. AA6082-T6 and AA6063-T6 are high-strength Al-Mg-Si alloys that contain manganese to increase their mechanical properties, such as strength, toughness, and ductility. The chemical composition for both alloys is presented in Table 5.1. The welding was carried out on a five-axis MTS I-Stir™ PDS at NIAR. All welds were made on a steel anvil in the position control mode. Friction stir welds were performed along the grain direction. Each alloy was welded in the T6 temper. The weld parameters in this study were developed based on DOE methodology using Statgraphics™, a statistics software package in order to analyze the observations and data.

Table 5.1. Chemical Composition (%) of AA6063-T6 and AA6082-T6 [6, 58].

Component Wt. %										
Component	Silicon	Iron	Copper	Manganese	Magnesium	Chromium	Zinc	Titanium	Aluminum	Others
AA6063-T6	0.2-0.6	0.35	0.1	0.1	0.45-0.9	0.1	0.1	0.1	98.9	0.15
AA6082-T6	0.7-1.3	0.5	0.1	0.4-0.1	0.6-0.1	0.25	0.2	0.1	95.2-98.3	0.15

This study employed the following techniques: (1) visual analysis of the weld surface, (2) macrographs to investigate defects and anomalies, (3) overlap shear testing to optimize the mechanical properties, (4) microhardenss testing to determine hardness in the weld zone, and (5) e-NDE to detect anomalies primarily in the form of voids. The selected weld parameters were a rotation speed of 1,000 rpm, travel speed of 508 mm/min, tilt angle (lead angle) of 1°, and forge force of 7,118 N.

The weld tool, shown in Figure 5.1, had the following geometry: RH threads and LH CounterFlow™ flats, wiper shoulder of 12.70 mm in diameter, pin length of 4.62 mm, and pin diameter at the base of the shoulder of 5.45 mm.

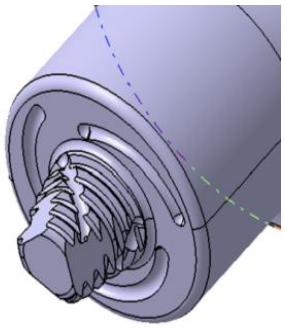

Figure 5.1. Weld tool configuration with right-hand threads and left-hand CounterFlow™ flats.

As shown in Figure 5.2, 3.5-mm-thick test specimens were prepared transverse to the weld using two different types of coupon configurations (Type A and Type B) to measure the failure load of the welded specimens as well as parent material. Type A refers to the regular shear lap specimens [64], and type B refers to dog-boned specimens [65]. The failure load for AA6063-T6 parent material was 17.79 KN, which was used to calculate the joint efficiency of the welds. Surfaces of the aluminum sheets were cleaned using MEK to remove oil and grease.

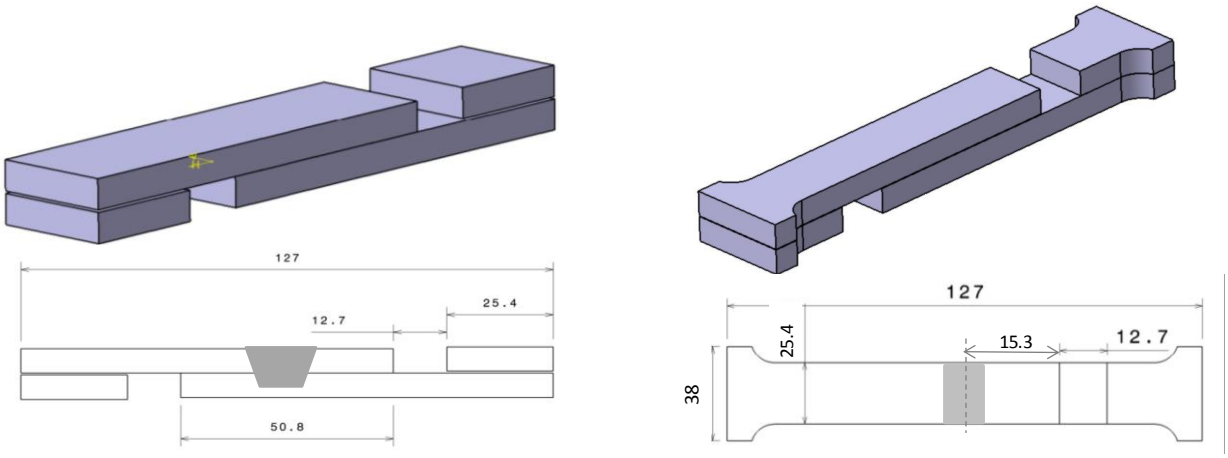

Figure 5.2. Schematic of overlap shear coupon configurations attached by spacer:
Type A (left) and Type B (right).

All weld specimens were tested in two different loading manners—advancing side and retreating side—for comparison purposes, as shown in Figure 5.3. Advancing side refers to the condition where tool tangential velocity is in the same direction as the tool travel direction, and

retreating side refers to the condition where tool tangential velocity is in the opposite direction as the tool travel direction [66]. A 370 MTS servo-hydraulic load frame with 50-mm gage length and 1.3-mm/min cross-head speed was used for the mechanical testing. The overall length of the specimen was 127 mm for both specimen types, and the nominal width of the grip section was 25.4 mm for specimen Type A and 38 mm for specimen Type B. Also, the nominal length of the reduced section (dog-boned) was 50.8 mm and its width was 25.4 mm. The Type B specimen was profiled using a TensileKut™ machine. Microhardness maps provided an understanding of the mechanical properties as well as microstructural properties of the weld by characterizing the hardness profile in the vicinity of the different zones of the weld cross section (e.g., heat-affected zone). Specifically, microhardness tests were performed on cross sections of selected welds perpendicular to the weld-line direction and in rows along the bottom, middle, and top sections across the weld zone by using a Leco AMH43 automatic microhardness tester with a Vickers scale of 500 gf load, 13-second dwell, and 550-micron spacing.

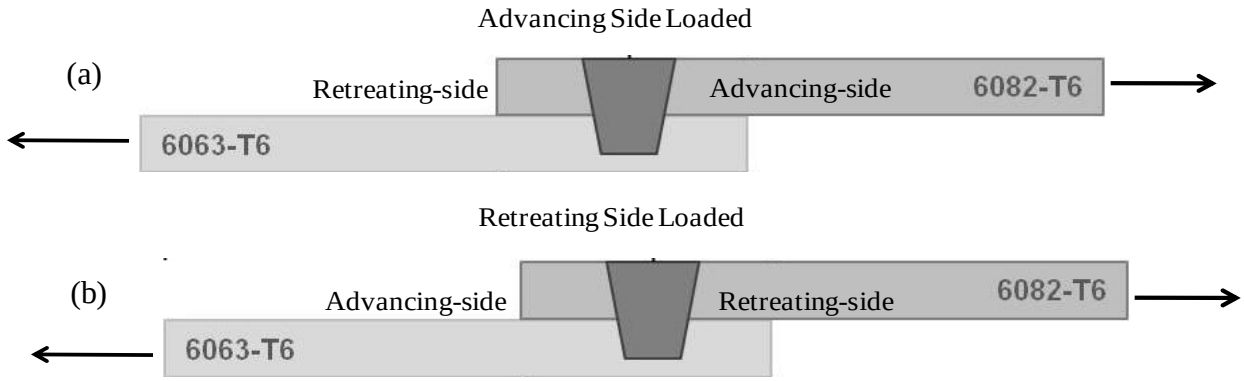

Figure 5.3. Loading configurations for shear lap testing of specimens:
(a) advancing side and (b) retreating side.

5.2.2 Feedback Signal Analysis

Mechanical properties of the friction stir joints improved when the heat input of the process decreased. Correspondingly, the dynamics of the feedback forces changed when the heat

input of the process increased. The feedback signals were analyzed by a tool developed by Boldsaikhan et al. [67]. Figures 5.4 and 5.5 show the frequency spectra of transverse force feedback. The heat input shown in the Figure 5.4 weld is lower than the heat input shown in the Figure 5.5 weld, whereas the tool Z load is lower in the Figure 5.4 weld than in the Figure 5.5 weld. The tool feedback force signal shown in Figure 5.5 contains a noticeable low-frequency peak compared to the spindle frequency peak. This is because the tool is experiencing more resistance from the plasticized material when the plunge depth of the tool increased due to the higher Z load. As reported by Arbegast [68], Morihara [69], and Boldsaikhan et al. [67], the feedback force signals contain more low-frequency oscillations, while material resistance in response to the tool motion increases.

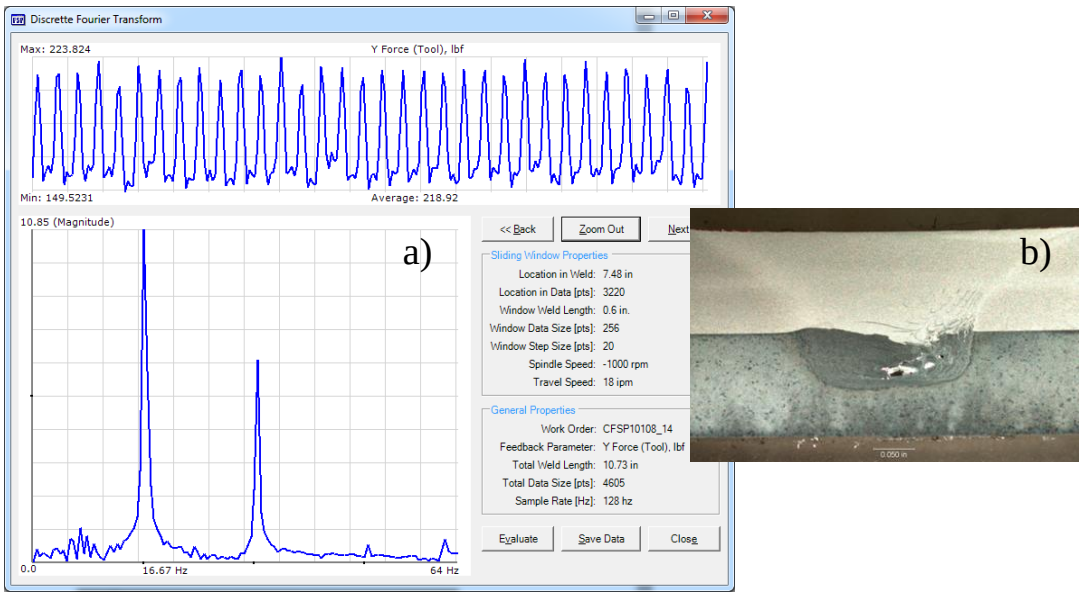

Figure 5.4. (a) Frequency spectra of transverse force feedback for lower heat input and lower Z force; spindle frequency peak at 16.67 Hz, and (b) CFSP10108_14_M1 with 70% average joint efficiency (tool Z load: 6.34 Kn (1,425 lbf)).

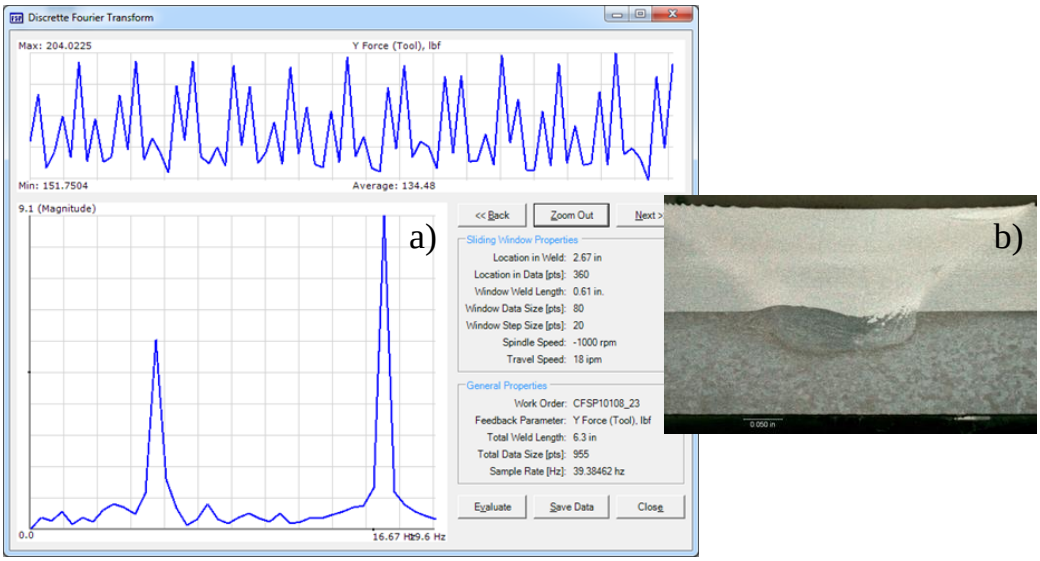

Figure 5.5. (a) Frequency spectra of transverse force feedback for higher heat input and higher Z force; spindle frequency peak is 16.67 Hz, and (b) CFSP10108_23_M1 with 70% average joint efficiency (tool Z load: 7.34 Kn (1,650 lbf)).

5.3 Results and Discussion

5.3.1 Overlap Shear Testing

Since lap joints are primarily loaded with shear force, it was decided to determine the strength of the weld using overlap shear testing methodology. Also, due to the asymmetric nature of friction stir welding, a lap weld specimen can be loaded with either the advancing side loaded on the top sheet or the retreating side loaded on the top sheet (see Figure 5.3 previously). The overlap shear testing results is presented in Figures 5.6 and 5.7.

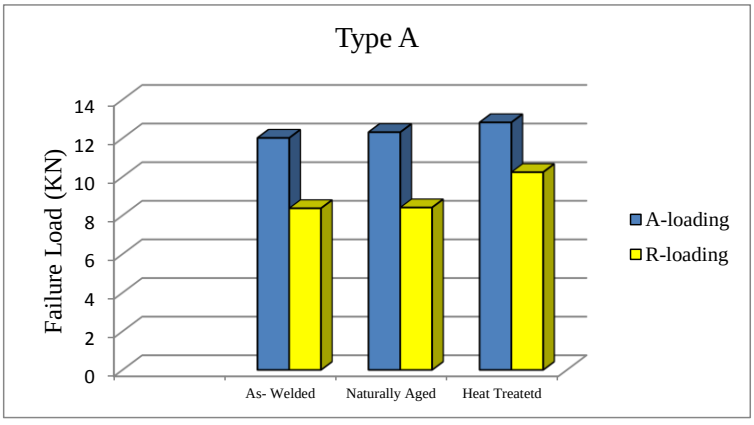

Figure 5.6. Shear lap testing results for Type A specimens.

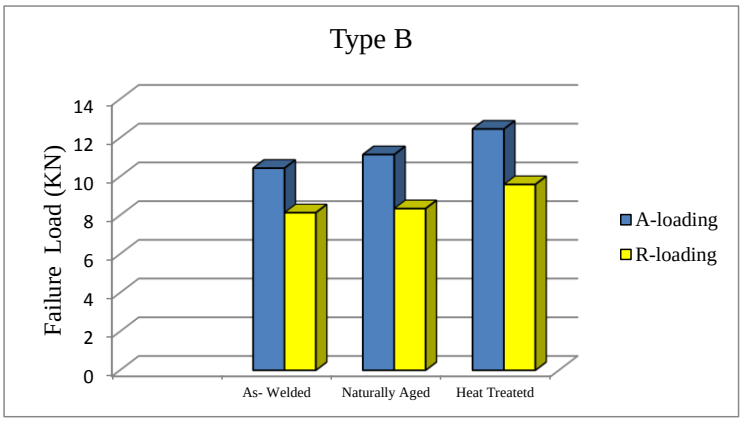

Figure 5.7. Shear lap testing results for Type B specimens.

All Type A and B welds were tested in as-welded, naturally aged, and heat-treated conditions. The heat-treated cycle used was 177°C for 6 hours to produce roughly a T6 temper in the stir zone. As-welded specimens were tested one day after the welding, whereas naturally aged specimens were left at room temperature for 120 hours before testing [60]. To align the specimens during overlap shear testing, 3.5-mm-thick spacers of the same materials as AA6082-T6 and AA6063-T6 were adhered to the end of the specimens. Tables 5.2 and 5.3 present the average value of joint efficiency and failure load for the FSW specimens (three specimens each). The highest joint efficiency was observed in the heat-treated specimens for both Types A and B. The amount of joint efficiency was increased from the as-welded condition through the heat-treated condition. For the welded specimens, it was observed that dissimilar joints resulted in almost 70% joint efficiency relative to the AA6063-T6 parent material, while shear loading was applied to the advancing side. However, the failure load drastically decreased to almost 55% for specimens with retreating-side loading.

Table 5.2. Shear Lap Testing Results for Type A FSW Specimens.

Overlap Shear Test Data for Type A Specimens						
FSW	WS (mm/s)	RS (rpm)	F Load (KN) A-Loading	Joint Efficiency (%)	F Load (KN) R-Loading	Joint Efficiency (%)
As-Welded	508	1000	12.015	67.60	8.370	47.10
Naturally Aged	508	1000	12.312	69.20	8.411	47.30
Heat-Treated	508	1000	12.820	72.10	10.240	57.56
WS = welding speed ; RS = rotational speed ; F = failure; A = advancing side; R = retreating side						

Table 5.3. Shear Lap Testing Results for Type B FSW Specimens.

Overlap Shear Test Data for Type B Specimens						
FSW	WS (mm/s)	RS (rpm)	F Load (KN) A-Loading	Joint Efficiency (%)	F Load (KN) R-Loading	Joint Efficiency (%)
As-Welded	508	1000	10.440	58.98	8.141	45.99
Naturally Aged	508	1000	11.141	62.94	8.352	47.19
Heat-Treated	508	1000	12.462	70.04	9.598	54.22
WS = welding speed ; RS = rotational speed ; F = failure ; A = advancing side ; R = retreating side						

Considering joint efficiency as the ratio of the failure load of the welded joints divided by the failure load of the base material, it was also determined that the failure load decreased in Type B specimens due to the net load transfer between the top and bottom sheets as well as the geometry of the specimens, in comparison to Type A specimens. In general, the failure load was generally larger for advancing-side loading specimens than retreating-side loading specimens due to the strong texture of the grains in the advancing side as well as the existing sharp boundary between the different zones of the weld area, including the nugget, HAZ, and TMAZ, while the retreating side had a more complex microstructure, with no clear boundary between the weld zones.

5.3.2 Microhardness Testing

A Vickers hardness profile (HV) with 0.5 kgf for a lap weld specimen is presented in Figure 5.8. A microhardness profile interprets the microstructure of the weld and its mechanical properties in the vicinity of the weld-affected zone in the FSW specimens. The microhardness test was performed in different rows of the specimens through the thickness after polishing the specimen. The hardness for AA6082-T6 parent material presented higher values of hardness than AA6063-T6 parent material, varying between 122 and 58 and between 88 and 46 for the top and bottom sheets, respectively. The parent material hardness was 118 for the top sheet (AA6082-T6) and 80 for the bottom sheet. Microhardness results indicate that hardness drastically decreased in the weld (nugget) zone, where the average hardness was significantly lower than in the parent material. This was due to the variation of the microstructures between the weld zone and parent material as well as different grain sizes of these two regions.

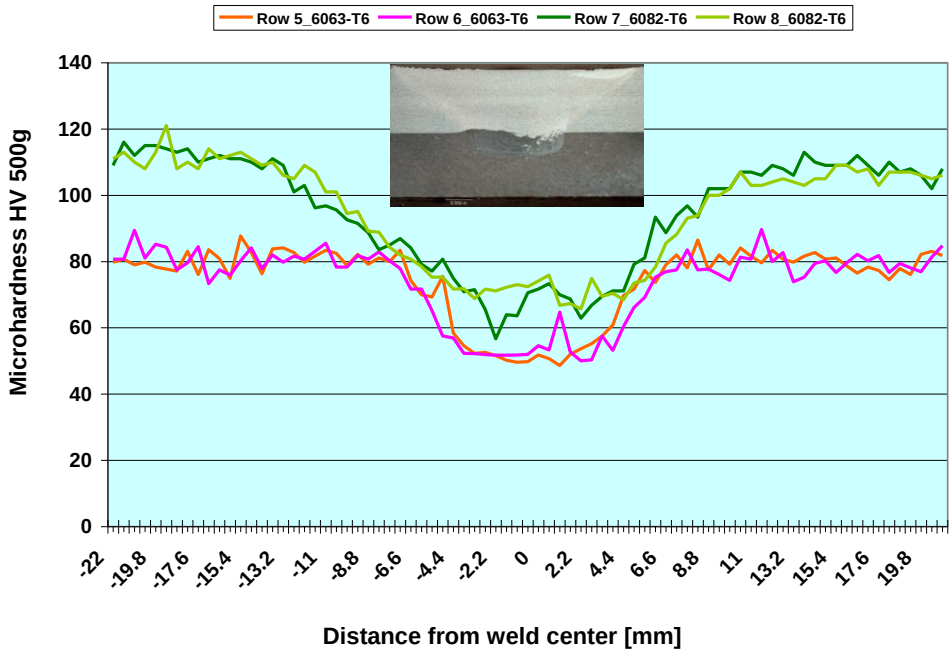

Figure 5.8. Microhardness profile of FSW specimens (data obtained at top and middle rows of cross section taken perpendicular to weld line).

5.3.3 Metallographic Analysis

Figure 5.9 shows the macrostructure of a friction stir weld of a dissimilar joint alloy. In this profile, some important weld joint regions, including the nugget, TMAZ, and HAZ, are identified. Additional elements include the deformed grains or swirl marks underneath the shoulder, advancing and retreating sides, weld flash, and onion ring pattern (nugget).

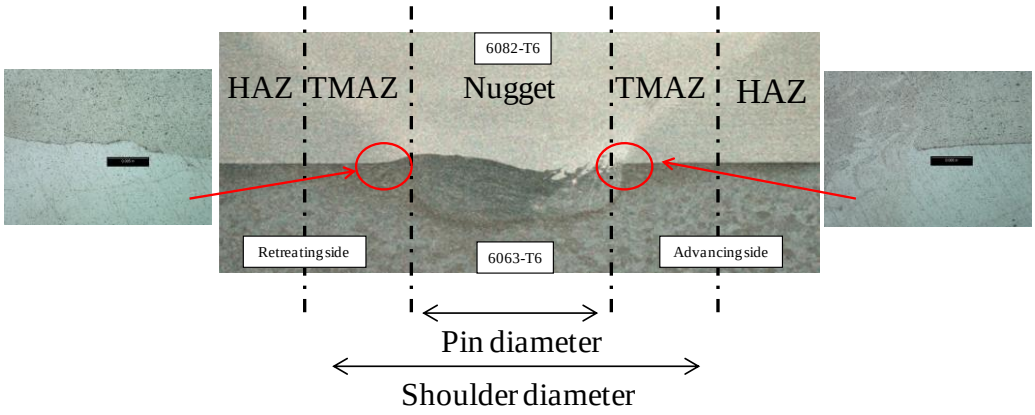

Figure 5.9. Macrostructure of dissimilar joint presenting weld regions, and close-up of advancing and retreating sides with no hook defect.

The onion ring pattern is essentially the representation of a banded microstructure brought together by the stirring action of the pin. In the TMAZ, grain growth and plastic deformation without recrystallization occurs, and a distinct boundary occurs between the TMAZ and weld nugget. The HAZ is only affected by the heat generated during the welding process. In the HAZ, there may be slight grain growth, but there is no plastic deformation [12].

In general, the material affected by the welding process presents a fine stir grain structure, and the material near the HAZ presents regular grains. Also, in the FSW, zone very fine recrystallized grains are present due to the high deformation and high temperature during the process. Based on macroscopic examination, the weld cross section is defect free and does not include any voids and flaws. One of the most common defects observed in FSW lap joints is a hooking defect, which results in a decrease of mechanical properties in the weld when found in

the load path [12, 70]. Using a CounterFlow™ pin tool in lap weld applications helps to draw the joint material at the probe together and thereby circumvent void formation and the hooking defect at the weld joint. According to the macrograph of the lap joint shown in Figure 5.10, it is obvious that there was minimal-to-no hooking in the nugget of the weld, especially in the advancing side versus the retreating side, which tends to increase the strength of the weld [71].

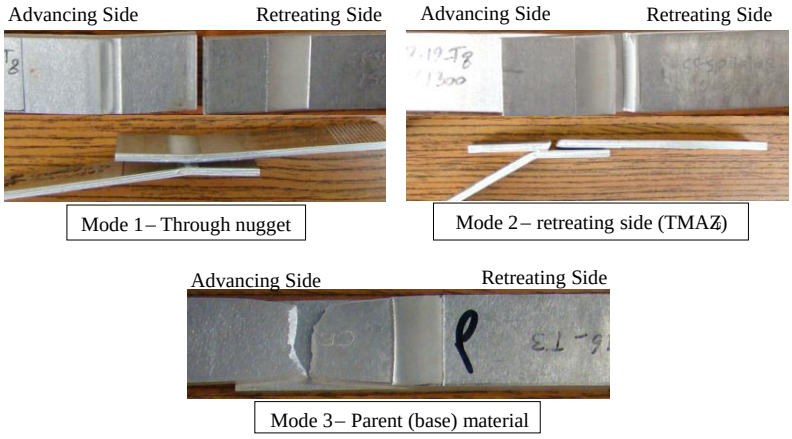

Figure 5.10. Separation location in FSW lap weld specimens: Mode 1—through the nugget, Mode 2—retreating-side top sheet (TMAZ), and Mode 3—base material.

5.3.4 Failure Locations

As shown in Figure 5.10, three failure mode locations were observed for as-welded, naturally aged, and heat-treated specimens. Also, the results for failure analysis were combined, based on both advancing side and retreating side loading.

Mode 1 is where the fracture initiation location starts from the interface of the top and bottom sheets and then passes through the nugget. Further analysis on the tested specimens showed that the amount of Mode 1 failure was higher in as-welded specimens than in post-weld specimens, due to less grain recrystallization. In Mode 2, failure is associated with the retreating side (TMAZ) of the top sheet, where a small hook was observed (refer to Figure 5.8 previously). All heat-treated specimen's survived Mode 2 failure. Mode 3 indicates the most promising failure in lap weld joints, which was initiated in the parent (base) material. However, the

maximum average of joint efficiency is 70%, with some exception. Few of the heat-treated specimens exhibited a very-high weld strength, which resulted in separation in this area. As discussed previously, the joint efficiency for each category was calculated based on the average of the three specimens.

5.3.5 Finite Element Analysis

The finite element model created was used to verify the types of displacements seen in lap shear testing of friction stir welds in a lap joint configuration as well as to look at the distribution of stresses in the weld region during lap shear testing. Finite element analysis was performed on Type A of the specimens. Figure 5.11 is a graph obtained from mechanical shear testing, where its peak indicates the maximum applied load. After about 1,125 lbf or 5,000 Newton, the specimen experienced elastic-plastic strain rather than linear-elastic strain. For lap shear testing, the samples were clamped on the grip section of each side, and a shear load was applied in one direction. To properly model this, a pressure load was applied in the positive x-direction, resulting in all clamped nodes allowed to move in only the positive x-direction. The clamped nodes at the other end of the sample were constrained from displacements and rotations ($\sum D = 0$ and $\sum R = 0$). The model contained 2592 HEX8 elements and 3978 nodes.

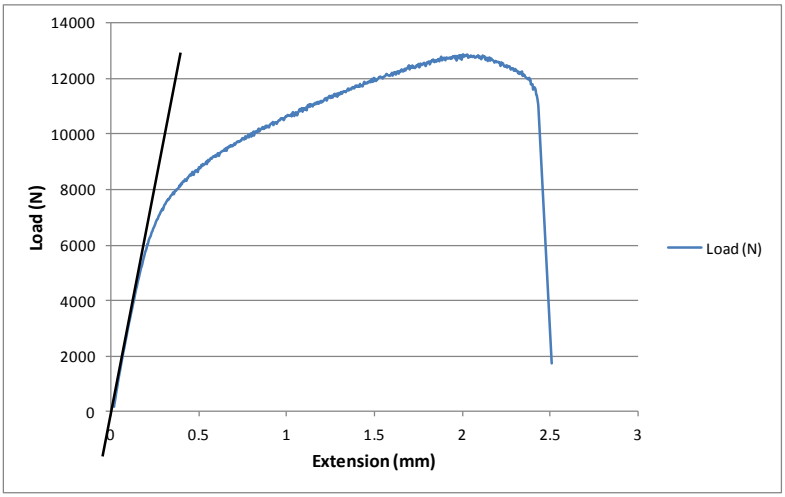

Figure 5.11. Load versus extension of FSW lap weld specimen during shear testing.

The displaced mesh was analyzed to ensure that the specimens deformed in the same manner as seen during shear testing, which is shown in Figure 5.12 (a). Also, a von Mises stress (VMS) contour was conducted to determine the stress distribution through the weld region. As shown in Figure 5.12 (b), the stress distribution is uneven on both sides and varies more in the vicinity of the weld zone where the top and bottom sheets join together.

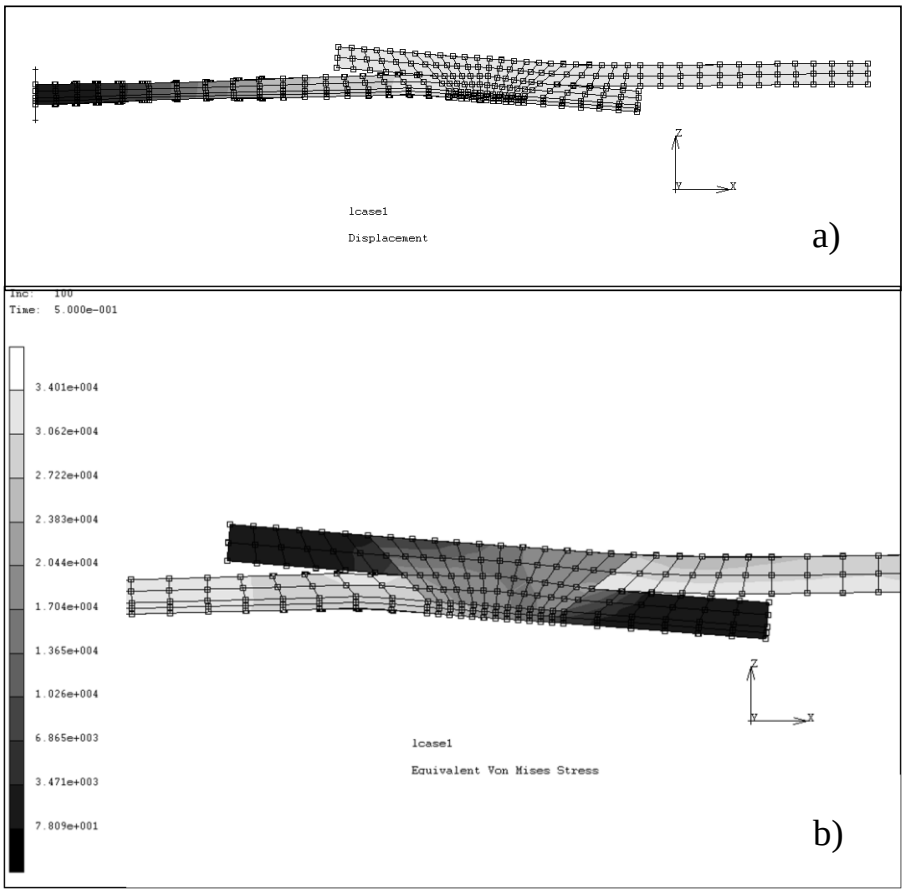

Figure 5.12. Finite element analysis: (a) deformed mesh model behaving in same manner as real shear test specimens, and (b) von Mises stress contour plot for shear lap test specimens 3.5 mm thick and 25.4 mm wide.

As can be seen, the non-welded material a short distance from the end of the lapping face experienced the greatest amount of stress, in comparison to the weld zone itself, which was due to the fact that the overlap of the weld was not fully welded and automatically became a site for crack initiation. This is evidenced by looking at the failure location in most of the lap shear weld

testing (see Figure 5.10 previously). Other reasons such as the existence of the possible hooking effect, geometry of the specimens, and mechanical properties of the 6xxx series aluminum alloys influence the high stress concentration in these zones. The hooking defect propagates the crack further into the weld zone and degrades the strength of the weld [71, 72].

5.4 Conclusions

Friction stir lap-welded joints between AA6082-T6 and AA6063-T6 were produced through the optimized weld parameters as a result of the DOE process. Also, according to the hardness profile of the joint, the lowest value of hardness was obtained in the weld zone, which corresponds to the location of the weld separation when shear testing the dissimilar lap weld joints. In the shear lap tests, separation occurred in three different modes: nugget of the weld where the minimum amount of hardness was observed (Mode 1), TMAZ of the weld on the retreating side where the possible hooking effect influences separation of the weld as well as where the highest amount of stress distribution is observed (Mode 2), and the base (parent) material of the specimens (Mode 3). The joint efficiency for T6 heat-treated specimens increased 3% over naturally aged specimens and 5% over as-welded specimens for advancing-side loading of Type A specimens. Also, the joint efficiency for T6 heat-treated specimens increased 7% over naturally aged specimens and 11% over as-welded specimens for advancing-side loading of Type B specimens. Microstructural properties and the analysis of dissimilar lap joints including material flow, mixture of the two alloys, and absence of the hooking effect are clearly identified. It was also ascertained that advancing-side loading performed at a higher strength than retreating-side loading, which is evidence that the retreating-side loading is not a good application in FSW due to the weaker weld strength on this side. Oscillations of the feedback forces were changed as the process heat input decreased, which provides evidence that the

feedback forces can be used for evaluating mechanical and metallurgical qualities of welded joints. Also, it was determined that the feedback force signals contained more low-frequency oscillations, while material resistance in response to the tool motions increased. Finally, an FEA was run to determine the displacement and stress distribution that a lap weld sample undergoes during a shear test. As observed previously in Figure 5.12 (a), the model deformed in the same way that actual specimens deformed during shear testing. Also, the maximum amount of stress distribution based on the von Mises contour plot was obtained at the interface of the top and bottom sheets.

CHAPTER 6

FRICTION STIR WELD DEVELOPMENT OF BUMPER-BEAM/CRASH-BOX ASSEMBLIES MADE FROM AA6082-T6 AND AA6063-T6 EXTRUSIONS*

6.1 Introduction

The application of friction stir welding to aluminum is not new, but the application of FSW to the bumper-beam/crash-box assembly, as shown in Figure 6.1, provided benefits that are unique to FSW.

Figure 6.1. Bumper-beam/crash-box assembly.

Loading on the joint required a significant nugget size, which precluded resistance spot welding. Gas metal arc welding would have been feasible but introduces a significant heat input and dimensional distortion from end to end of the bumper beam, which needs to be minimized in order to reduce any residual stress when attaching the bumper assembly to the front rail face pads. Therefore, in this study, in order to produce a feasible solution, advancements were used to build an experimental bumper-beam/crash-box assembly having partial FSW butt joints between dissimilar alloy extruded components. Previously, an initial process window with a given tool design was evaluated on a coupon level [49].

---

*The content of this chapter was published entirely as "Friction Stir Weld Development of Bumper Crash Box Assemblies Made from AA6082-T6 and AA6063-T6 Extrusions" in *Proceedings of the 9th International Friction Stir Welding Symposium*, The Von Braun Center, Huntsville, AL, May 15–17, 2012. The literature review part of this paper has been merged into the Literature Review section in Chapter 2 of this dissertation.

A significantly different thermal loading occurred when welding these extruded parts such that the original tool was not found to be capable of producing void-free (sound) joints at the test article (assembly) level. The previous weld tool had a tapered probe with RH threads and RH twisted flats, and a 10.16-mm-diameter flat shoulder. The probe length was 3.25 mm, the taper angle was 10 degrees, and the probe diameter at the shoulder end was 3.9 mm.

Response variables were derived from microstructure testing, microhardness testing, and the e-NDE technique (employed to identify void formation from feedback force data). As shown in Figure 6.2, perfectly sound and acceptable joints (over 90% joint efficiency) were produced in this phase of the work [49].

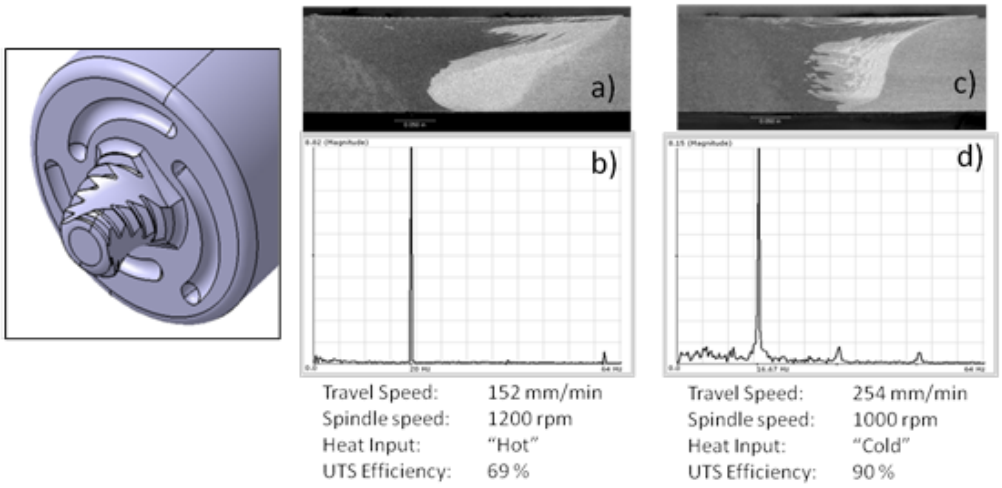

Figure 6.2. Initial weld tool with RH threads and RH twisted flats, and transverse cross-section macrographs and corresponding e-NDE maps for two coupon-level FSW joints between 3.5-mm (0.138 in.)-thick AA6082-T6 and AA6063-T6: (a) and (b) "hot" weld; (c) and (d) "cold" weld.

The frequency spectra of the feedback forces shown in Figure 6.3 indicate the dominant spindle frequency peaks with minimal "low" and "high" frequency contents for the fully consolidated friction stir joints, whereas the "low" and "high" frequency contents refer to the lower and higher frequency oscillations relative to the spindle frequency of the weld tool. Once the coupon-level results were applied to the actual parts, voids and defects were observed in the

weld zone at the end of the probe, as shown in Figure 6.3 (a). These joints were produced using the coupon-level weld tool and corresponding parameters. The following observations were made from these welding trials: (1) welds were produced under position control and had an acceptable surface appearance based on visual inspection; (2) welds produced between the assembled extrusion parts had a lack of consolidation and poor surface finish, and consequently, the DOE coupon welds were not shown to be directly representative of the assembly application; and (3) frequency spectra of the feedback forces shown in Figure 6.3 (b) revealed significant "low" and "high" frequency events (relative to the spindle frequency), indicating the detection of possible voids based upon feedback forces.

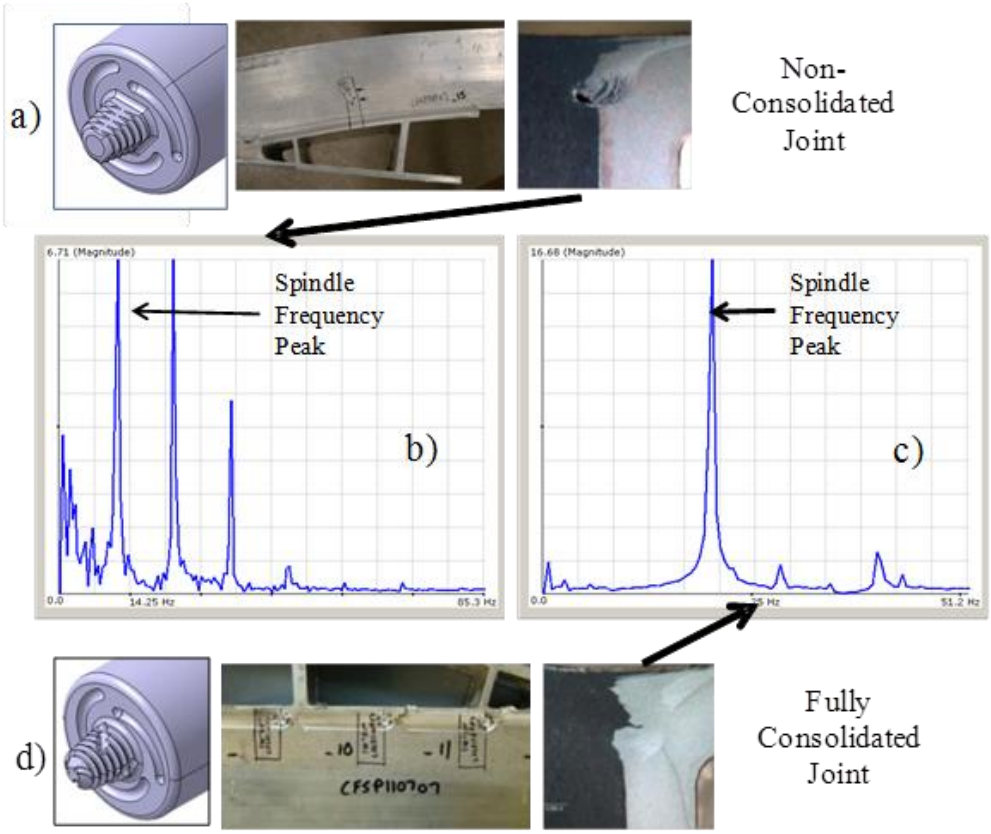

Figure 6.3. (a) Previous (coupon-level) probe design, macrograph of bumper-beam/crash-box weld, and cross section of weld exhibiting porosity; (b) frequency spectra of transverse force feedback for coupon-level probe design; (c) frequency spectra of transverse force feedback for component level probe design; and (d) new (component level) probe design, macrograph of bumper-beam/crash-box weld, and cross section of solid weld.

6.2 Methodology

6.2.1 Experimental and Welding Procedures

Based on these observations, three new weld tools, shown in Figure 6.4, were designed and tested in order to eliminate the formation of the voids near the tool probe tip. A "concentrating tip" consisting of a set of tapered scrolls was included on the end of each probe, in order to increase and centralize the downward flow of the joint material at the tool tip. Several features were added to the length of the threaded probe to evaluate various approaches for lowering pressure on the probe as it passed along the joint line. These included a set of partial straight flats and a set of partial CounterFlow™ grooves. Each was extended only partially along the probe length in order to lessen the propensity to form a void at the probe tip. To establish a baseline for comparison, a tool with just threads was also tested. The Wiper™ shoulder design used in the coupon phase of the program remained unchanged. A range of weld parameters was tested to determine the best weld tool design solution.

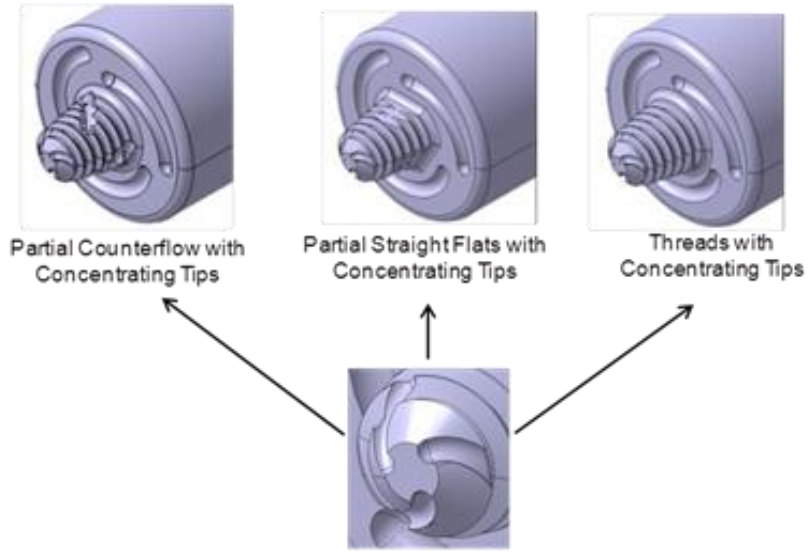

Figure 6.4. New weld tool design modification with concentrating tip.

6.2.2 Wedge Test

Due to the geometry of the welded parts, the mechanical properties of the joints could not be evaluated using conventional mechanical testing methods, such as tensile testing an ASTM B557 coupon, due to the lack of material for the grip section [59]. Therefore, a wedge test using a machined steel wedge (35°) was devised, as shown in Figure 6.5. From each weld, one sample was extracted near the end of a 38.1-mm weld for testing. Test samples were cut and polished to similar dimensions, which were nominally the same width (14.0 mm ± 1.25) with the basic geometry shown in Figure 6.5.

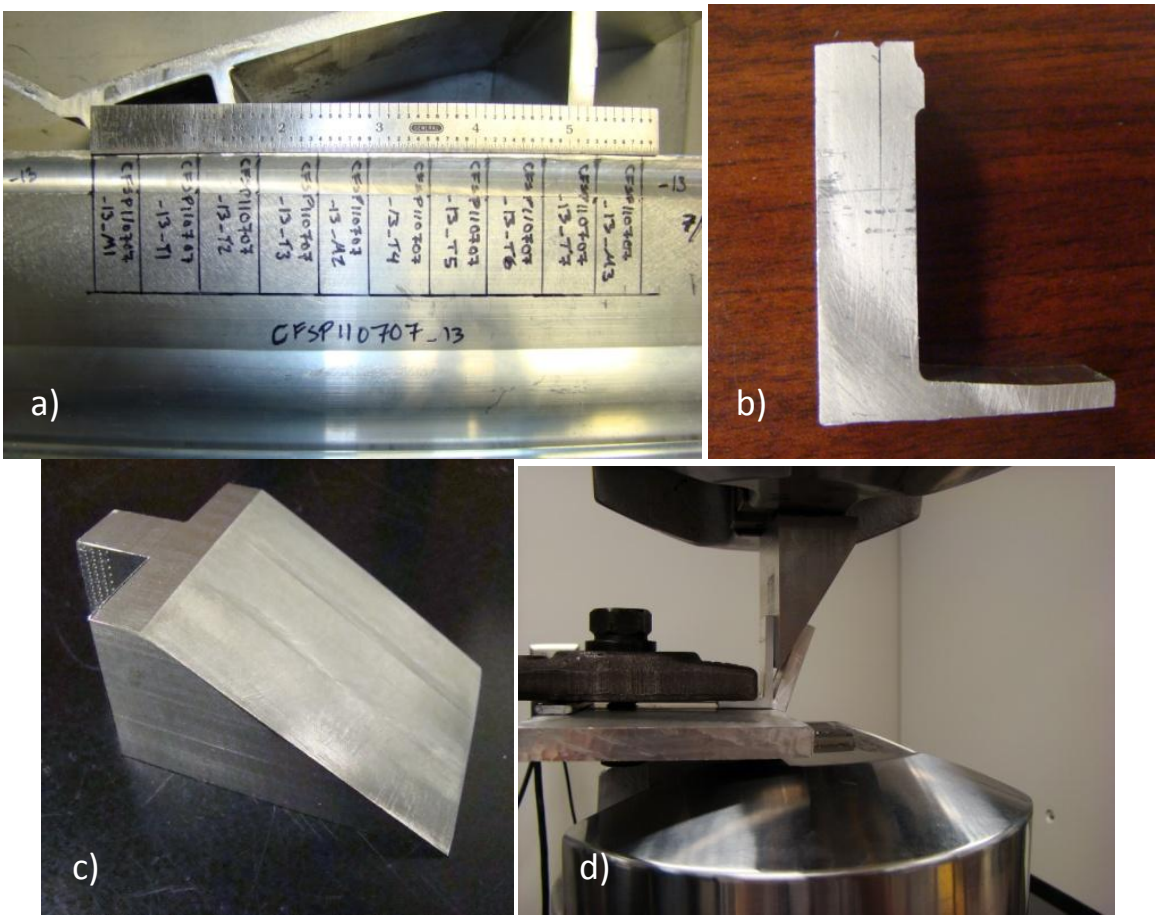

Figure 6.5. Sample test and wedge testing configuration: (a) cut plan for bumper-beam/crash-box welded assembly; (b) cut and polished sample awaiting testing; (c) 35^0 machined steel wedge; and (d) clamped sample undergoing wedge testing.

The testing was conducted on a 22-kip MTS Landmark load frame. During testing, the 35° wedge was displaced at a constant rate while the load was recorded at 10 Hz as a function of displacement, as shown in Figure 6.6. The wedge was set at a fixed initial position that remained constant for all specimens and traveled a distance of 38.1 mm for each run. The load-displacement plots were numerically integrated to calculate the area under the curve as a relative measure of toughness and normalized by the sample width.

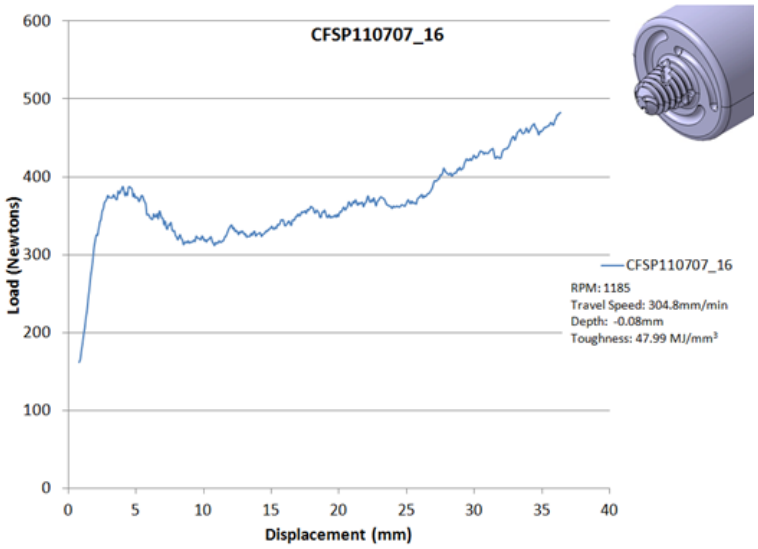

Figure 6.6. Wedge test load-displacement plot for measuring relative joint toughness.

6.2.3 Feedback Signal Analysis

In friction stir welding, the time series data of the tool feedback forces can be used for characterizing the physical interactions between the material flow and the weld tool [8]. While the feedback signals might be distorted by FSW machine-dependent noises, the indications of stable and/or erroneous material flow have been found to be retained in the time series data of the feedback forces [8]. In this study, feedback force signals, including drag, transverse, and forge, were captured during each welding experiment at a sampling rate of at least 3.5 times the tool spindle speed. Afterwards, the captured signals were analyzed using e-NDE software [7, 8].

6.3 Results and Discussion

6.3.1 Wedge Testing Results and Tool Selection

After wedge testing the specimens for all three tools (refer to Figure 6.4 previously), the weld tool with a partial CounterFlow™ probe having a concentrating tip consistently produced tougher welds. Therefore, this tool was chosen for the subsequent process window evaluation in order to define the weld schedule for the final bumper-beam assemblies. After selecting parameters based on a review of the macrographs and wedge test results, three weld parameters displaying the highest toughness per mm of weld (ranging from 2.860 to 3.336 MJ/mm4) were re-run at full length (203.2 mm) in order to further validate the integrity of the test and the consistency of the sample results. Seven samples and three macrographs were extracted near the beginning, middle, and end of each weld and evaluated (refer to Table 6.1).

Table 6.1. Wedge Test Results from Specimens Welded Using Partial CounterFlow™ Tool with Concentrating Tip

RPM	Travel Speed	Average Toughness per Millimeter of Weld	Std. Dev. Of Toughness per Millimeter of Weld
	(mm/min)	(MJ/mm^4)	(MJ/mm^4)
1185	76.2	2.756	0.6349
1185	152.4	2.584	0.1415
1185	304.8	2.519	0.3819

Although there were not statistically significant differences in the toughness values for the three weld schedules, an analysis was necessary to choose the final schedule. The highest average toughness per meter of weld used the slowest linear speed at 76.2 mm/min, which likely

ran at the hottest temperature. But it is important to point out that this parameter set also had the largest standard deviation. Therefore, this parameter set was omitted from further consideration. The coldest parameter set, which was also the fastest linear speed at 304.8 mm/min, had the smallest average toughness per meter of weld. This average toughness was only slightly less than that for a linear speed of 152.4 mm/min parameter. An analysis of variance table was constructed with $\alpha = 0.05$ for the remaining two parameters, and a p-value of 0.583 was obtained. Since the p-value > α, it was determined that there was no significant difference in the resulting mean toughness per millimeter of weld. Since production rates are of great importance, the process parameters associated with a travel speed of 304.8 mm/min were used to weld the final bumper-beam assemblies.

According to the toughness plot shown in Figure 6.6, the selected tool probe was a partial CounterFlow™ using weld parameters of a rotation speed of 1,185 rpm, travel speed of 305 mm/min, and tilt angle (lead angle) of 1°. The AA6082-T6 material was placed along the advancing side of the weld, and the AA6063-T6 material was placed along the retreating side. Figure 6.7 shows the entire FSW bumper-beam/crash-box assembly.

Figure 6.7: Tooling for friction stir butt weld.

As can be seen, the new tool design with the concentrating tip feature generated fully consolidated friction stir joints by eliminating the void formed by regular weld tools. The e-NDE indications of feedback forces were in a good agreement with this joint quality, whereas the frequency spectra of the feedback forces contained minimal “high” and “low” frequency events (refer previously to Figure 6.3(c)).

CHAPTER 7

DYNAMIC CRASH TESTING OF FSW AND GMAW CRASH BOXES AND BUMPERS*

7.1 Introduction

In order to evaluate the strength of the welded assemblies in a dynamic condition, traditional sled testing for low-speed bumper requirements and drop tower testing were performed. The drop tower test fixture was fabricated using friction stir welding, and testing was carried out at the Dynamic Impact Laboratory of NIAR at WSU. These dynamic tests were performed using both FSW and GMAW bumpers. An analysis of the collected data gathered from both the sled and the drop tower tests is provided. FEA was used to compare the predicted damage to the actual damage sustained by the bumpers fabricated by GMAW and FSW, respectively.

As an alternative, according to the objective of this case study, a set of FSW bumpers was manufactured to evaluate the impact (crash) performance of FSW joints during a low-speed bumper test. The established criteria for success was that the FSW bumper should perform as well as or better than the fusion-welded bumper design. To evaluate the bumpers, impact tests were performed both on the crash sled at the GM R&D laboratory in Detroit, Michigan, and on the drop tower fabricated using FSW at WSU.

---

*The content of this chapter was published entirely as "Friction Stir Weld Development of Bumper Crash Box Assemblies Made from AA6082-T6 & AA6063-T6 Extrusion" in the *Proceedings of the 9th International Friction Stir Welding Symposium*, The Von Braun Center, Huntsville, AL, May 15–17, 2012. The literature review part of this paper has been merged into the Literature Review section of this dissertation in Chapter 2.

7.2 Bumper Testing Procedures

For each test condition, four welded bumper-beam assemblies—three FSW and one GMAW—were tested using the GM R&D impact sled (Figure 7.1). Also, for each test condition, three weld specimens—two FSW and one GMAW—were tested using an FSW drop tower [75, 76] at WSU (Figure 7.2).

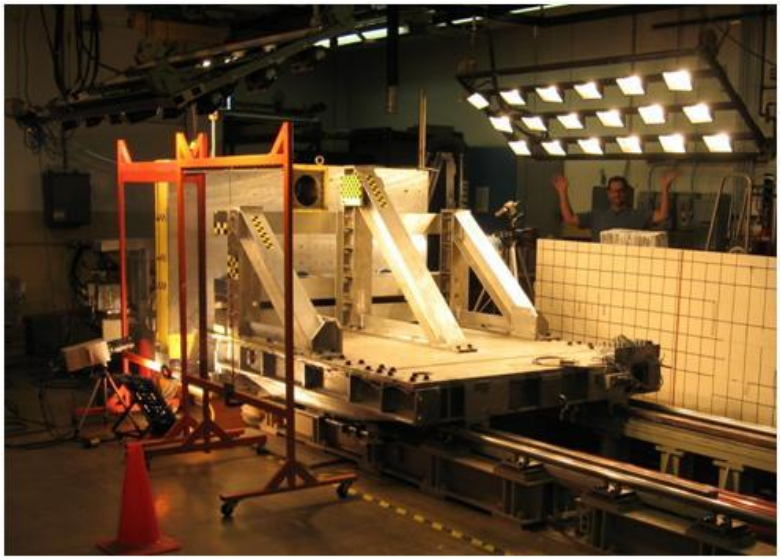

Figure 7.1. GM R&D impact sled.

Figure 7.2. FSW drop tower.

Four speed levels (energy levels) representing 7, 10, 15, and 20 kilometers per hour (kph) using a 1,368 kg mass were applied, as defined by the New Car Assessment Program (NCAP) Federal Motor Vehicle Safety Standard (FMVSS) 208 Part 581 [77]. Since the GM sled mass was fixed at 1,140 kg, the FMVSS test requirements allowed the sled speeds to be modified to 1.52 m/s, 3.04 m/s, 4.56 m/s, and 6.08 m/s, using the kinetic equation of motion ($KE = \frac{1}{2} mv^2$, where KE is the kinetic energy, m is the mass, and v is the velocity). The sled tests were monitored for target speeds to verify that the speed at the instant of impact was equivalent to four predefined energy levels, as mentioned previously. A total of 19 bumpers was used during sled testing. This included the four specimens tested at each speed, one FSW and one GMAW specimen for backup, and one non-data bumper used for setup verification. The gauged bumpers were left at GM and not measured following testing. However, on-site photos, videos, and MS Excel test files were retained for each test. Spreadsheets with acceleration, velocity, load-cell forces, and strain-gauge output were recorded by the system, along with videos. Pictures were taken at loading before the test, and still pictures were taken after testing, either at GM or in the Advanced Joining and Processing Laboratory at WSU.

The 1.52 m/s target was below the minimum obtainable speed by the sled; therefore, 2 m/s, representing a 7.2 kph impact energy, was used for the slowest sled speed. Drop tower energy heights were determined for the four speeds by equating the calculated sled energy to the standard potential energy equation ($PE = mgh$, where PE is potential energy, m is mass, g is gravitational acceleration, and h is altitude) using a tower mass of 1,424 kg and solving for h. The height was adjusted downward, based on FEM analysis, to account for the increase in drop tower velocity after impact, due to the acceleration caused by gravity. Strain measurements were taken for all FSW drop tower specimens and for one FSW sled specimen at each speed.

7.3 Dynamic Impact Tests

7.3.1 Sled Test Setup

Figure 7.3 shows the way that all FSW and GMAW bumpers were mounted for sled testing. Prior to testing the bumper-beam assemblies, each crash box foot attachment was predrilled with eight holes, as shown in Figure 7.4.

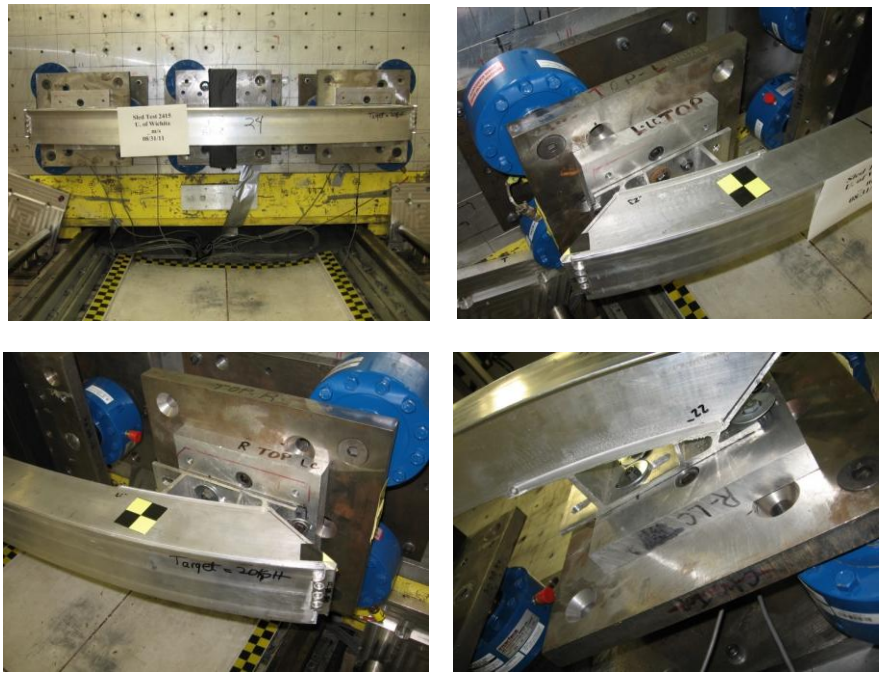

Figure 7.3. Sled testing setup.

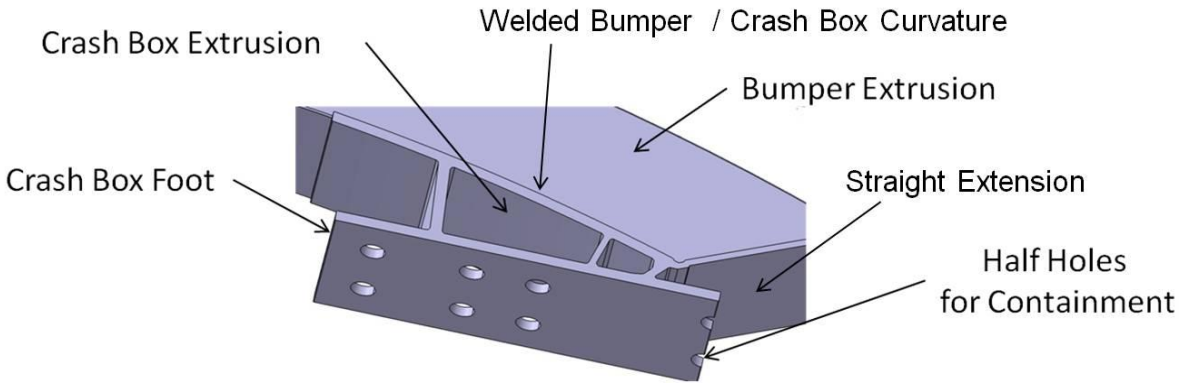

Figure 7.4. Predrilled attach holes (sled test locations circled).

The eight holes were then slotted to accommodate deviations between the bumpers and the mounting-plate-attachment locations. Instead of the full set of eight holes, only the middle two holes and two containment holes, shown in Figure 7.4, were used during the sled tests. As a result of not including bolts in the remaining four holes of the bolt pattern, the crash box feet bent or lifted away from the loading block in between the bolts that were installed. This effect was predicted with FEA of the test setup, as illustrated in Figure 7.5. This lifting caused a stress concentration to build up in the joint corners where the butt weld stopped and the angled portion of the crash box extension began. It was at this corner that the most severe crack damage was observed from tests performed at all speeds. The drop tower, however, utilized all attachment locations, and video results indicated no significant lifting of the foot during testing.

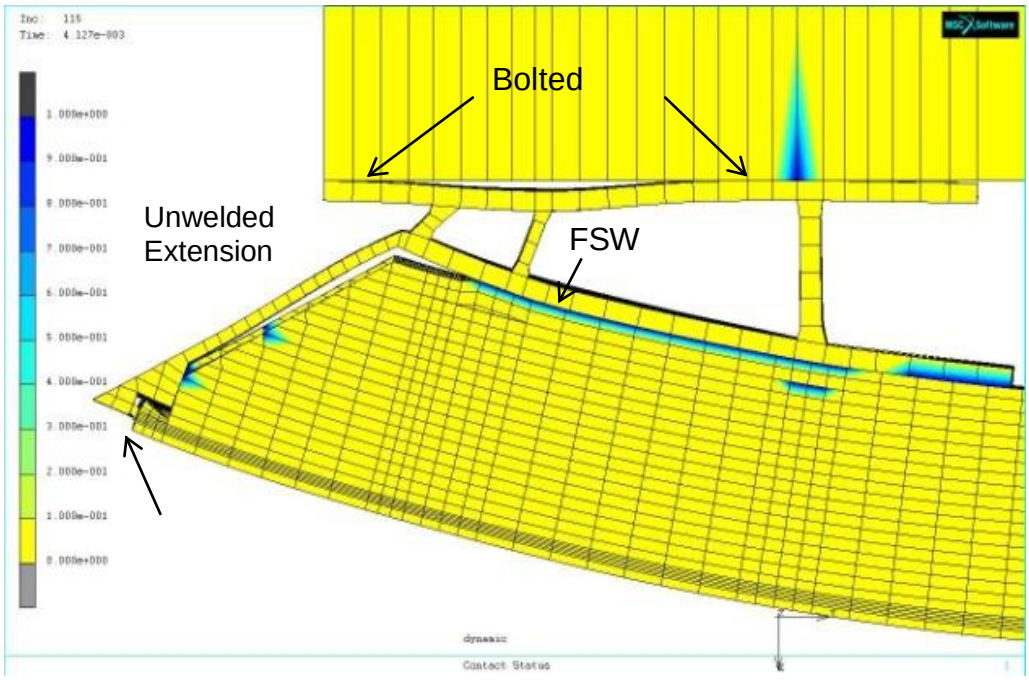

Figure 7.5. FEM of lifting crash box foot in FSW sled simulation at 20 kph [76].

As noted, a high-speed video record of each test was taken for documentation. A video taken from the overhead position for a specimen (2413) tested at 10 kph shows the raised foot as the sled impacted the stationary mounted bumper on the impact wall. This video was linked to the fall 2011 CFSP (IAB) meeting presentation for this project and is available upon request. Strain gauges were used for one set of friction stir-welded bumpers at each speed. However, an error in scaling range was not discovered until testing was complete, which resulted in the loss of data associated with the failure in the specimens

7.3.2 Drop Tower Test Setup

The drop tower testing setup is shown in Figure 7.6. At each test speed, two FSW specimens and a single GMAW specimen were tested and the results compared. Strain measurements were taken for all FSW specimens at each speed.

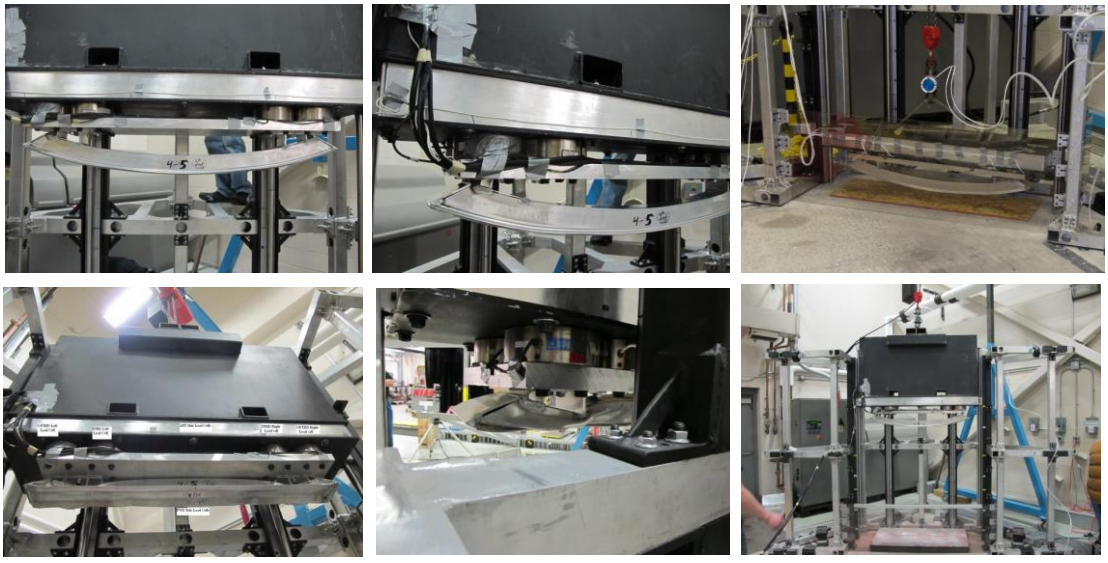

Figure 7.6. Drop tower testing setup.

As mentioned previously, the four energy levels defined by the NCAP FMVSS 208 Part 581 [77, 78] were 7, 10, 15, and 20 kph using a 1,368 kg mass. The tower mass was 1,424 kg (3,137 lbm). Therefore, using the potential energy equation (PE = mgh), the calculated sled

energy was equated to the potential energy to obtain the corresponding drop height. The drop tower height was adjusted downward, based on FEM analysis, so that the increase in velocity after impact, due to the acceleration caused by gravity, was accounted for in matching the sled target speeds. With three specimens at each speed and one test bumper for strain gage calibration, 13 bumpers were used during the drop tower testing. On-site photos, high-speed videos, and MS Excel spreadsheets with acceleration, velocity, load cell forces, and strain gage output were recorded using crash system instruments. Pictures were taken at loading and before testing, and still damage pictures were taken after testing at the WSU AJPL. Figure 7.6 shows the FSW drop tower unit used for this phase of the testing program.

7.4 Sled Test Results

Three weld separations were observed in GMAW welds: at the crash box curvature and at the straight extension corner. The weld separations, as shown in Figures 7.7 and 7.8, were in the 10 kph energy (3.05 m/s) test and the 20 kph energy (6.10 m/s) test. The FSSW joints located at the bumper closeout (see Figure 7.5 previously) showed deformation starting in the low-speed tests and weld separation in the high-speed tests. The geometry of the bumper-beam/crash-box assembly was noted as influencing these test results. Specifically, the inside leg of the crash box acted as the moment arm fulcrum for a force at the closeouts, which pulled away the foot from the ends. The closeout geometry overlapped from the crash box and allowed the separated FSSW joints to still hold at the 15 kph (4.50 m/s) energy tests but separated at the 20 kph (6.10 m/s) energy tests (Figures 7.9 and 7.10).

Damage resulting from 7 kph, 10 kph, 15 kph, and 20 kph energy tests of the FSW bumper was compared with fusion-weld test assemblies. The only complete weld failures were observed in the fusion welds at the corner crash box extension and in the FSSW welds at the

bumper-closeout location. The fusion-weld failures were found in two (top and bottom) corner welds of a 10 kph test. These failures were associated with the crash box foot that remained bolted during the impact (Figure 7.7). During the 10 kph test, a bolt broke on the side of the bumper in which the welds remained intact. Another joint failure occurred in one of the bottom-side (flanged) welds in a 20 kph test, as shown in Figure 7.8. Links to videos of these tests were included in the fall 2011 CFSP IAB meeting presentation for this project and are available upon request.

Figure 7.7. Complete separation in GMAW bumpers.

Figure 7.8. Failures in GMAW bumpers.

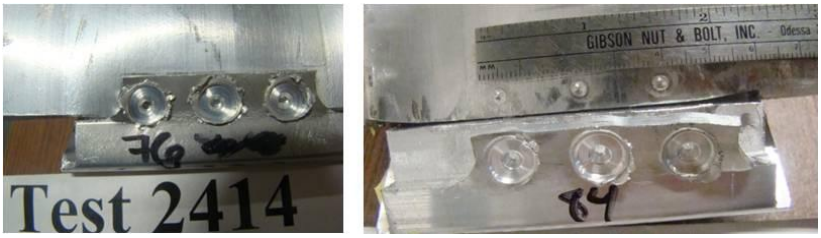

Figure 7.9. Spot weld separation with held joint at 35 kph energy (left), and complete spot weld and joint separation at 20 kph energy (right).

Figure 7.10. Deformation of spot weld at 7 kph (left) and 10 kph (right) energies.

The extent of cracking in the FSW bumpers remained nominally the same, independent of the increase of crash test speeds. No complete separations or unstable crack growth was observed in the FSW joints. Instead, the welded joints were observed to bend over on themselves and did not exhibit visible rupture or cracking within the weld zone. At the same time, long cracks were observed in the parent material associated with locations of extreme bending (Figures 7.11, 7.12, and 7.13).

Figure 7.11. Cracks at 7, 10, 15, and 20 kph energies for FSW (columns left to right, respectively).

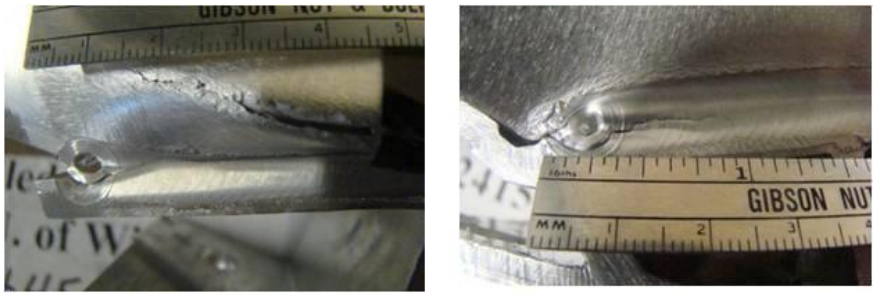

Figure 7.12. Cracks at FSW weld exit under ruptured bumper wall at 15 kph and 20 kph energies.

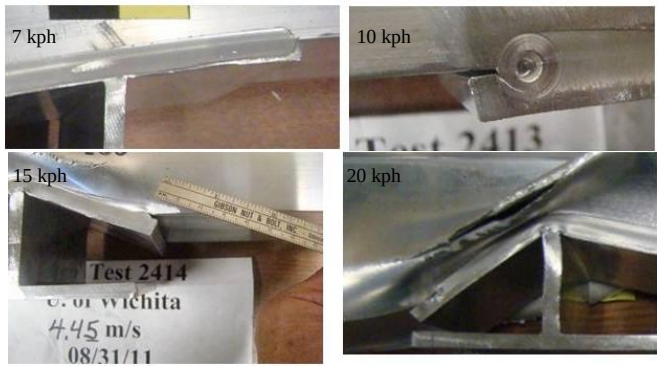

Figure 7.13. Cracks in ledge at 7, 10, 15, and 20 kph energies.

GMAW welds, in comparison, had less apparent ductility than the FSW joints. In FSW bumpers tested at 15 kph and 20 kph energies, the welded joints folded upon themselves, much like parent material, but did not exhibit visible rupture or cracking within the weld zone, while long cracks were observed in the parent material associated with locations of extreme bending. GMAW welds, in comparison, were observed to fail completely and therefore had less apparent ductility than the FSW joints. No failures or unstable crack growth were observed from the ends of the FSW joints opposite the crash box extension (Figures 7.13).

7.5 Drop Tower Test Results

Unlike the sled tests conducted at GM, the drop test bumper assemblies were attached to the crash system mounting plate using all eight holes in each crash box (see Figure 7.4 previously for bolt-hole pattern). The holes were predrilled and slotted for both ends to accommodate any deviations between the bumpers and the mounting-plate-attachment locations. Because the containment holes were only half holes, an extra half-hole plate was made for the last two bolts of each foot to prevent the foot from rotating back and rising up in the middle, as occurred during the sled test. Strain gauges were used for the two FSW bumpers. One test bumper was used to scale the strain output for 20% gages to read up to 200,000 micro strains. The test part configuration was simulated originally in an FEM model of the sled test. Figure

7.14 shows another FEM simulation of a 20 kph drop tower impact. This simulation incorporated two welded butt joints, one running along the curved interface and one running up the straight interface between the two extrusions and therefore is stiffer than the actual test part. Nonetheless, the strains obtained with this simulation still gave good agreement with the strains collected during testing (Figure 7.15).

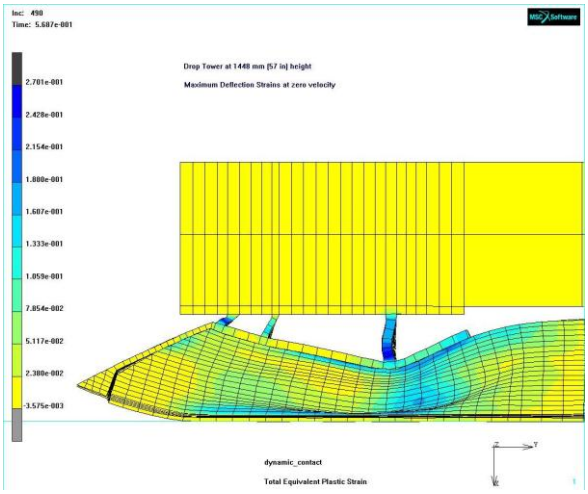

Figure 7.14. FEM of maximum plastic strains at zero velocity [76].

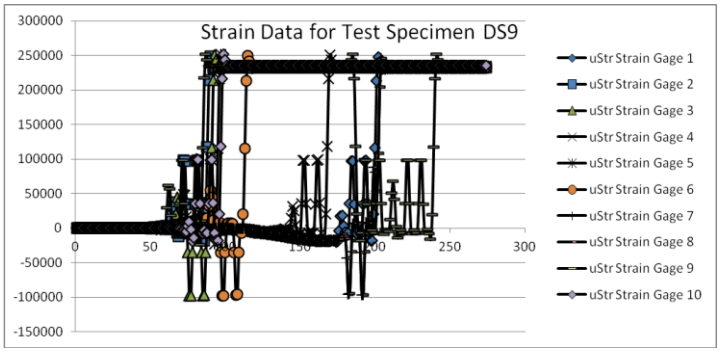

Figure 7.15. Micro strain data output.

The extent of damage resulting from testing the FSW bumpers at 5 kph, 10 kph, 15 kph, and 20 kph energy targets was documented and compared. A catch system to limit the impact to only one rebound was not incorporated in the test procedure due to time and funding constraints. As in the sled tests, the only FSW failures occurred at the closeout spot welds. Although the

FSW butt joint cracks exhibited longer lengths compared with the sled tests, no complete joint failures were observed. Further study should be performed by destructive means to document the actual amount of failure present in the FSW butt joints.

Fusion butt weld separations occurred at all test speeds, but no closeout weld separations were observed. The most common separation was in corner welds. This location was not always visible to the camera for the fusion bumpers. Since a catch system to limit the impact hits to only one rebound was not incorporated in the test procedure because of time and cost constraints, it is not known in all cases whether any crack propagation took place by cyclic loading from the multiple rebounds. The weld failure at 5 kph, shown in Figure 7.16, was on the unflanged side and, therefore, visible to the camera. From a review of the video recording, it was determined that the cyclic loading after impact did not play a part in this weld failure. Figure 7.17 shows the results of a low-speed GMAW test at 10 kph energy, which is representative of the type of separation seen.

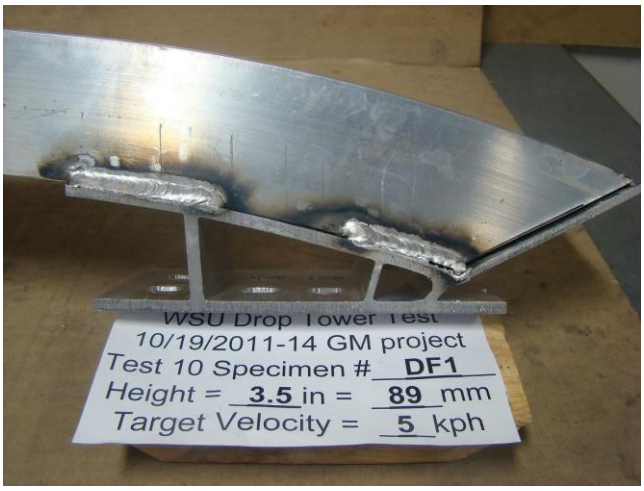

Figure 7.16. Damage at 5 kph energy (one broken weld).

Figure 7.17. Separated corner welds at 10 kph.

The closeout FSSW joints showed no deformation at low speeds, although some of the installed risers for mounting these strain gages were observed to debond during impact (right side of Figure 7.18). All FSSW joints separated at 15 kph and 20 kph energies, as shown in Figure 7.19. Fusion weld failure at 15 and 20 kph target speeds are shown in Figure 7.20 and Figure 7.21. At 15 kph, two corner welds broke but appeared to be pushed back together by the collapse of the bumper-beam. The bumper wall also appears to begin to tear open as a result of the test conditions. At 20 kph, two welds were shown to have broken, while the opposite side welds showed completed surface cracks. More investigation is warranted to determine conclusively if these cracked surface welds were actually broken at impact.

Figure 7.18. Spot welds at 5 kph and 10 kph energies (left to right).

Figure 7.19. Spot separations at 15 kph and 20 kph energies (left to right).

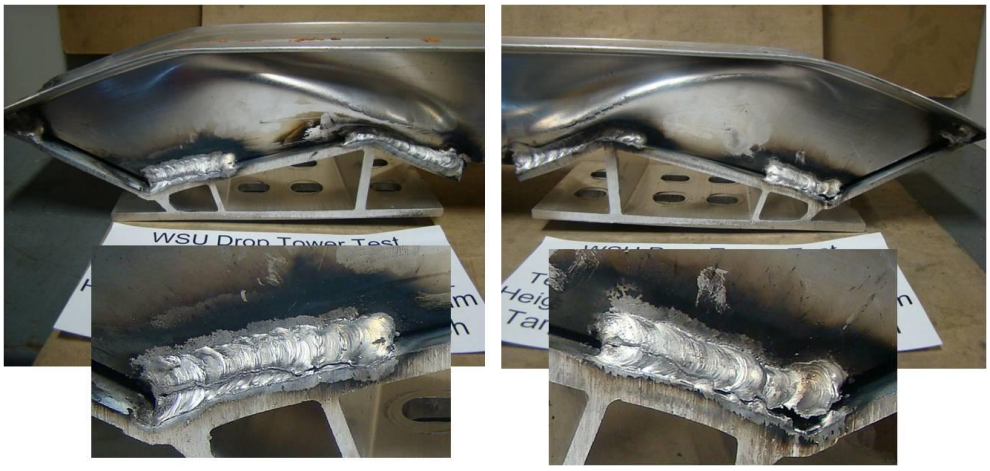

Figure 7.20: Damage in two broken welds at 15 kph energy.

Figure 7.21: Damage in two broken welds and two cracked welds at 20 kph energy.

Although the FSW butt joint cracks resulting from the drop tests were greater in length (2 cm to 10 cm) than those in the sled tests, no complete joint separations were observed. Ledge welds appeared to be more resistant to cracking at the 20 kph energy, compared to the 15 kph energy, allowing the weld to fold over under the degree of strain imposed on the joint. The parent material buckled and produced secondary cracks that ran into the HAZ weld zone. Examples of these cracks are shown in Figures 7.22, 7.23, and 7.24.

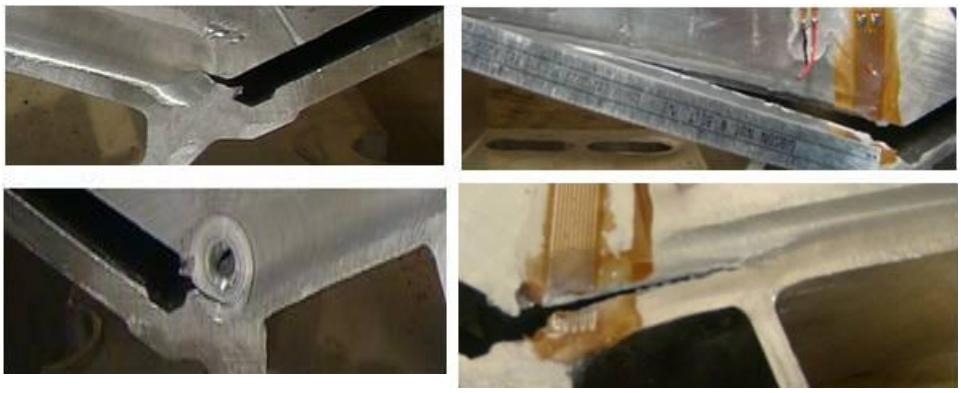

Figure 7.22: FSW cracks at 5 kph and 10 kph energies (left to right).

Figure 7.23: FSW cracks and deformation necking under ruptured bumper wall at 15 kph energy

.

Figure 7.24: FSW cracks under ruptured bumper wall at 20 kph energy.

7.6 Deflection Measurements

Bumper deflections using FSW and GMAW from the experimental full-frontal crash test are shown in Tables 7.1 and 7.2. The vertical deflection of the bumper was measured from the centerline or the outermost curvature of the bumper to the base of the crash box. Figure 7.25 shows the deflection comparison of the pre- and post-crash deformation of the bumper from experimental results. The post-crash deflection measurements indicate that the bumper deflection with FSW bumpers was generally lower than that of the GMAW bumpers. However, the experimental method failed to provide the instantaneous bumper deformation that will yield useful information, such as the deflection curve's rise time and peak deformations. This is accomplished with the use of FEA, which is discussed later.

Table 7.1. Experimental Results of Bumper Deflection Using GMAW

	Measured Bumper Velocity on Impact			
	7 km/hr	**10 km/hr**	**15 km/hr**	**20 km/hr**
Measured Bumper Deflection (mm)	14	29	46	84

Table 7.2. Bumper Deflection Using FSW from Experimental Results

Run #	Measured bumper velocity on impact (km/hr)	Measured bumper deflection (mm)
1	7.1	14.3
2	7.0	14.5
3	7.0	13.5
Average	***7.0***	***14.1***
4	9.8	29.3
5	9.7	26.3
6	9.7	26.0
Average	***9.8***	***27.2***
7	14.9	46.0
8	15.0	44.0
9	15.0	46.5
Average	***14.9***	***45.5***
10	20.1	83.0
11	20.1	76.5
Average	***20.1***	***79.8***

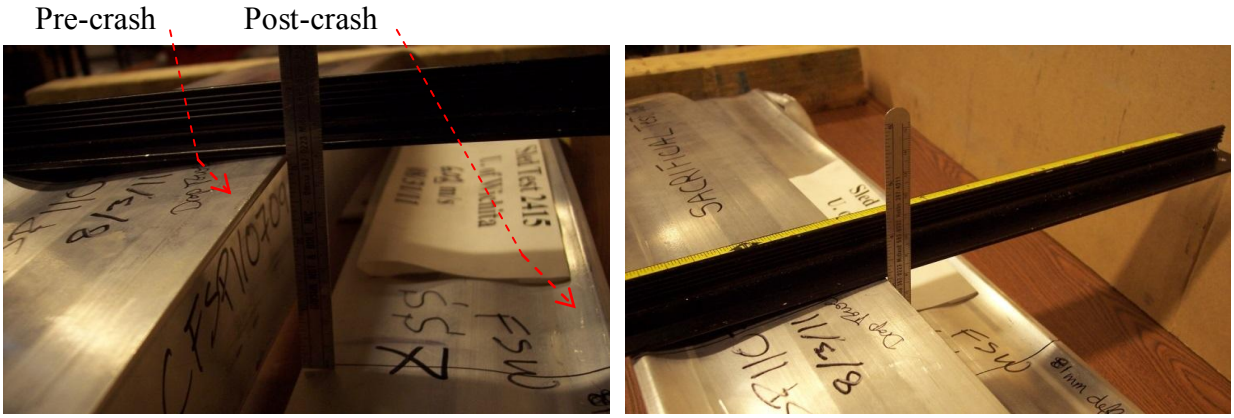

Figure 7.25. Deflection measurement method for all test assemblies, including both test and untested parts.

CHAPTER 8

FINITE ELEMENT ANALYSIS AND NUMERICAL INVESTIGATION INTO DYNAMIC CRASH TESTING OF VEHICLE BUMPER USING FRICTION STIR WELDING AND GAS METAL ARC WELDING

8.1 Introduction

In order to reduce the repeatability of tests and cost of the production, using the finite element model to analyze crash dynamics is increasing in the automotive industry. This has resulted in the improvement of FE models in terms of size, accuracy, and fidelity. LS-DYNA has been used to study and analyze this non-linear dynamic response. This very common finite element solver, which is based on explicit time integration, was released by Livermore Software Technology Corporation for simulating and analyzing many complex real-world problems. Some advantages of LS-DYNA in comparison to other FE software is the fully automatic definition of contact surfaces, a large library of element types and constitutive models, and special implementation for automotive problems like airbags, dummies, and seatbelts. LS-PREPOST is a new post processor for LS-DYNA simulations with a very friendly work environment that supports the latest standards in order to generate fast-rendering fringe plots and animation results. It is capable of generating contour plots, X-Y graphs, vector plots, overlay plots, movie formats (MPEG, AVI), printing formats (PS, TIFF, PNG), animations, input deck manipulation, and mesh manipulation [73, 74, 91].

---

*The content of this chapter has been submited in 2013 as "An Experimental and Numerical Investigation into the Dynamic Crash Testing of Vehicle Bumper using Friction Stir Welding and Gas Metal Arc Welding" in the *International Crashworthiness Journal*. The literature review part of this paper has been merged into the Literature Review section in Chapter 2 of this dissertation.

8.2 FE Model Development

In this study, the bumper beam and crash box were modeled using a computer-aided design (CAD) package and were meshed using Hypermesh. The bumper-beam/crash-box assembly was modeled in close relation with the experimental specimen to ensure accurate results. Figure 8.1 represents the partial CAD modeling of the bumper beam and crash box, and Figure 8.2 illustrates the finite element mesh of the assembly. In addition, the precise mechanical properties for the bumper, crash box, and weld joints were measured at the AJPL by using tensile testing, lap shear testing, and wedge testing. The finite element characteristics assigned to each component are tabulated in Table 8.1.

Figure 8.1. CAD modeling of bumper-beam/crash-box assembly.

Figure 8.2. Finite element mesh of bumper-beam/crash-box assembly.

Table 8.1. Summary of Vehicle Model

Component	Type of Element	Number of Elements	Number of Nodes
Bumper	Shell	68,334	68,258
Crash Box	Solid	3,550	3,534
Moving Deformable Barrier	Shell	22,913	34,116
FSW Weld Joint (approx.)	Solid	1,238	4,971
GMAW Weld Joint (approx.)	Beam	167	334

Similar to the experimental method, the bumper-beam/crash-box assembly was mounted onto the moving deformable barrier (MDB) for the full-frontal simulation. In order to replicate the experimental setup, an FMVSS 208 MDB was modified by replacing the FMVSS barrier to allow for mounting the GMAW and FSW bumpers. Figure 8.3 shows the complete numerical model. As can be seen, the distance between the barrier and the rigid wall was kept at the minimum to reduce computational time.

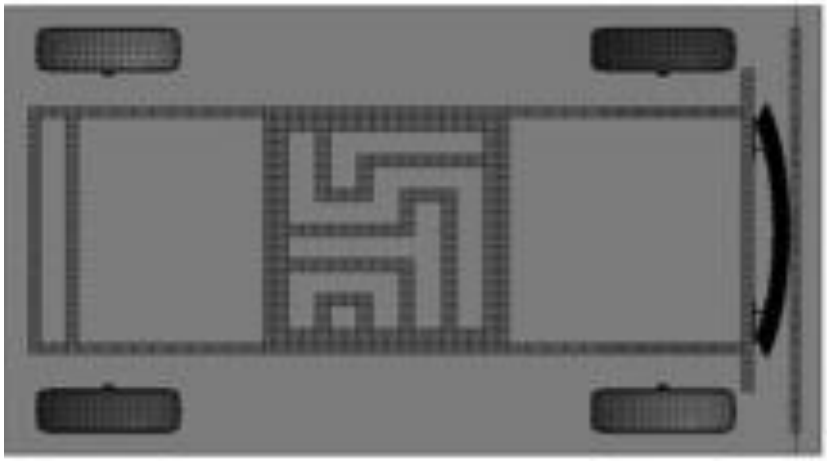

Figure 8.3. Full-frontal sled test setup using numerical method.

As mentioned previously, the FSW and GMAW processes of any dissimilar alloys are complex and would require an independent study. Therefore, in this dissertation, discussions on these processes are omitted because they fall out of this study's scope. The assumption made in this research was that FSW and GMAW were used to weld the bumper onto the crash box in an ideal condition. The mathematical model used to define the material properties of the FSW joint is the Johnson-Cook flow-stress model:

$$\sigma_y = \left(A + B\varepsilon_{pl}^{n}\right)\left[1 + C log\left(\frac{\varepsilon_{pl}^{n}}{\varepsilon_{o}^{n}}\right)\right](1 - T_H^m) \tag{8.1}$$

where A is the plastic strain constant, B is the strain hardening constant, C is the strain rate constant, n is the strain rate exponent, m is the thermal exponent, ε_{pl}^{n} is the plastic strain rate, and

ε_0^n is the reference plastic strain rate. The ε_0^n was set at $1.0s^{-1}$. Constants for the Johnson-Cook flow-stress model can be found in Tables 8.2, and the approximate technical specification used in this study are listed in Table 8.3 [91].

Table 8.2. Johnson-Cook Flow-Stress Model Constants.

Materials	A (MPa)	B (MPa)	C (MPa)	n	m	T_H(K)
AA6082-T6 [93]	428.5	327.7	0.0134	0.234	1.0	1733
AA6063-T6 [94]	261.2	126.8	0.0862	0.301	1.1	1140

Table 8.3. Approximate Technical Specifications.

Overall length (no deformation element mounted)	3632 mm
Track Width	1880 mm
Wheelbase	2591 mm
Tire	P 205/75 R 15
Crash Weight	1,361 kg
Position of center of gravity behind front axle	1,123 mm
Position of center of gravity left of longitudinal axis	7.6 mm
Position of center of gravity above roadway	500 mm
Moment of Inertia X-axis	508 kgm^2
Moment of Inertia Y-axis	2,263 kgm^2
Moment of Inertia Z-axis	2,572kgm^2

8.3 NCAP Test Procedure (Full-Frontal Impact Test)

In this test, the full width of vehicle was crashed into a rigid barrier (full-frontal impact), as depicted in Figure 8.4. The deformation of the car defined the pattern since the full-frontal width was crashed into the rigid barrier. Dummies were seated in the car (driver and passenger seats), and the amount of the impact on the dummy's head, chest, and legs was measured and evaluated. The full-frontal test provides a very-high deceleration force to the dummy [91]. One of the applications for this test is to evaluate the occupant resistant system, such as the air bag and seat belt.

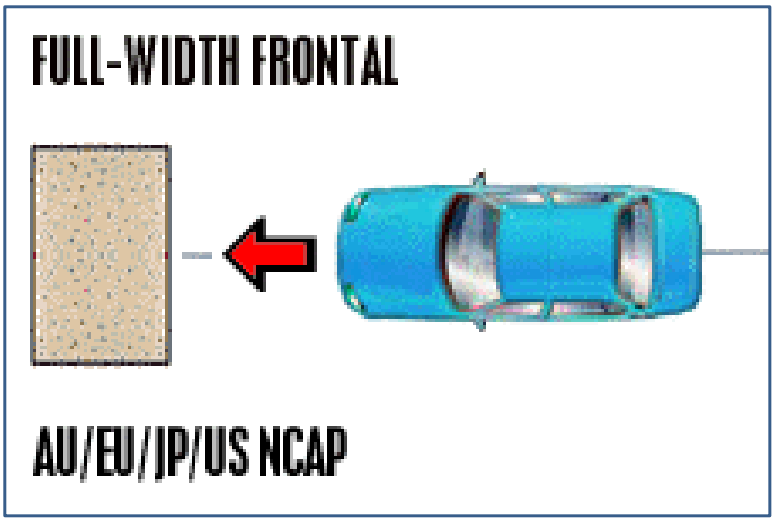

Figure 8.4. Depiction of full-frontal crash test [79].

8.3.1 Finite Element Analysis Results

The displaced mesh was analyzed to ensure that specimens deformed in the manner observed during the crash dynamic testing, as shown previously in Figure 7.14. It was confirmed that the model deformed in the same way that the specimens deformed when undergoing full-frontal impact. It was observed that deformation of the crash box and bumper was different than what occurred in the sled and drop tower testing at higher speeds (15 and 20 kph). As mentioned earlier, in actual sled testing, the crash box was mounted to the wall using four bolts passing through the crash box (two middle holes and two containment holes, see section 7.3.1). This caused the feet of the crash box to bend or be lifted away, so it was decided to consider a fully consistent contact surface between the crash box and the rigid wall for the FE model to avoid bending or lifting the crash-box feet. Hence, the deformation looks different than the actual tests at higher speeds. In addition, von Mises stress contours were plotted to visualize the stress distribution through the weld region, crash box, and bumper. Figure 8.5 shows the VMS distribution at the instant of impact for FSW bumpers at 7, 10, 15, and 20 kph energy targets.

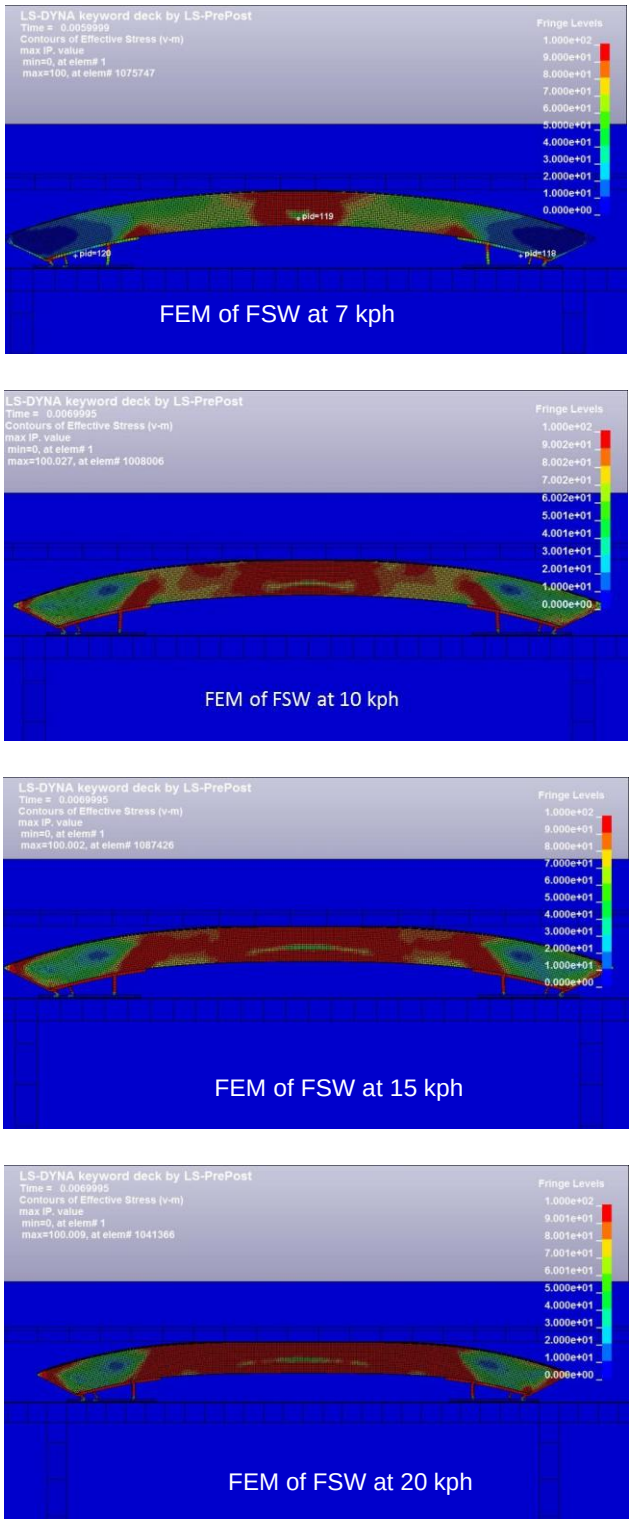

Figure 8.5. Von Mises stress distribution at instant of impact for FSW bumpers at 7, 10, 15, and 20 kph energy targets.

Failure of the bumper and crash box was analyzed using VMS to predict the failure or yielding of the numerical model. For comparison purposes, the VMS of the bumper and crash box at 20 km/hr crash velocity is shown in Figure 8.6. It can be seen that the blue region indicates a low-stress region that was more pronounced with the FSW bumper compared to the GMAW bumper. Based on the simulated model, the bumper with FSW had less deformation in comparison to the bumper with GMAW. In addition, the weld failure with GMAW promoted cracking, indicating that energy was not properly transferred to the crash box. Similar to the experimental results, crack growth was not observed at the FSW weld joint; therefore, kinetic energy that was efficiently transferred to the crash box resulted in less bumper deformation. The maximum VMS for the FSW and GMAW bumpers was 1.8G Pa and 2.12 GPa, respectively, showing that the GMAW bumper underwent an 18% higher maximum VMS than the FSW bumper.

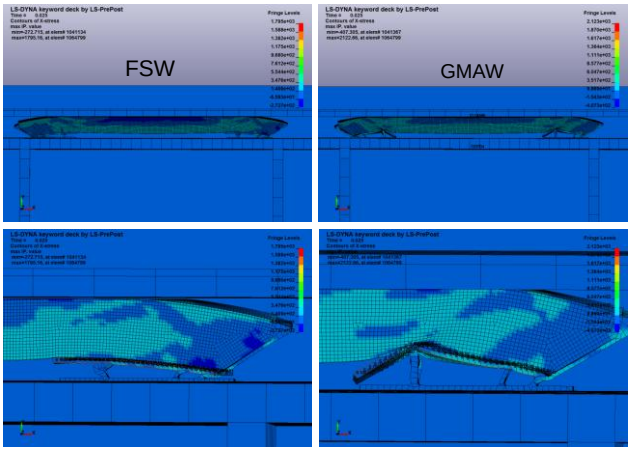

Figure 8.6. Stress comparison of FSW and GMAW bumpers at 20 kph energy target.

It should also be noted that obtaining these crack growths using the computer simulation posed considerable challenges. Parallel to the experimental results, the post-crash analysis of the FSW showed no separation at the weld joint. However, the crack in the GMAW weld joint could not be fully obtained from the computer simulation. According to the methodology section, it

was assumed that FSW and GMAW of the bumper-beam/crash-box assembly were conducted in an ideal situation. Therefore, the accurate crack growth at the weld joint should be referred to based on the experimental results.

Figure 8.7 shows the state of X-stress distribution for both FSW and GMAW bumpers at 20 kph. As can be seen, the amount of X-stress in GMAW bumpers was higher than the amount of X-stress achieved for FSW bumpers. According to Figure 8.7, the highest amount of stress was 42 MPa for FSW bumpers, where, for the same condition, this was about 124 MPa for GMAW bumpers. This proves that FSW bumpers absorb a higher amount of energy compared to GMAW bumpers.

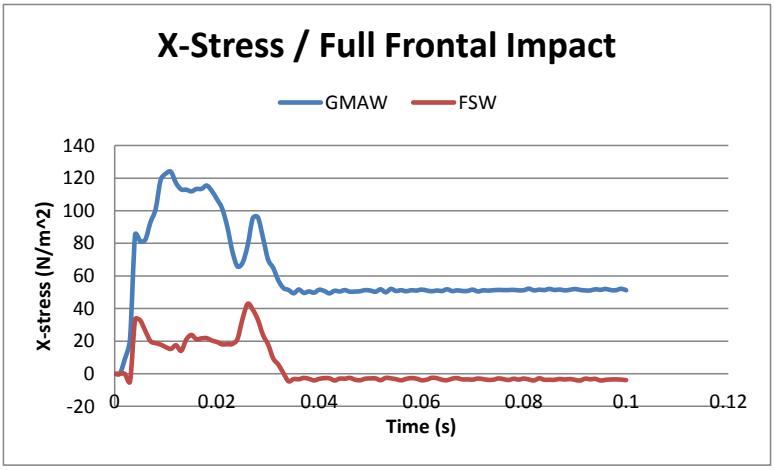

Figure 8.7. X-stress distribution for FSW and GMAW bumpers at 20 kph energy target.

In terms of energy absorption, the acceleration of the vehicle at the instant of impact was captured for both FSW and GMAW bumpers at 20 kph energy level (see Figure 8.8). The greatest magnitude of the barrier acceleration was about 3.8 G's for FSW bumpers and 5.1 G's for GMAW bumpers. As shown in Figure 8.8, the 26% reduction in peak acceleration was due to the ability of FSW to absorb higher kinetic energy, owing to the better weld quality (no weld separation or crack growth) of FSW compared to GMAW. Thus, the kinetic energy from the bumper was transferred efficiently to the crash box. Although occupant injuries were not within

the scope of this study, it is relevant to note, in broad terms, that acceleration has been used in many injury biomechanics studies as an important parameter in measuring occupant injuries. Therefore, the ability of lowering the MDB acceleration by using FSW may translate to lower occupant injury risks. This can be another reason proving that FSW increases the amount of energy absorption, in comparison to GMAW.

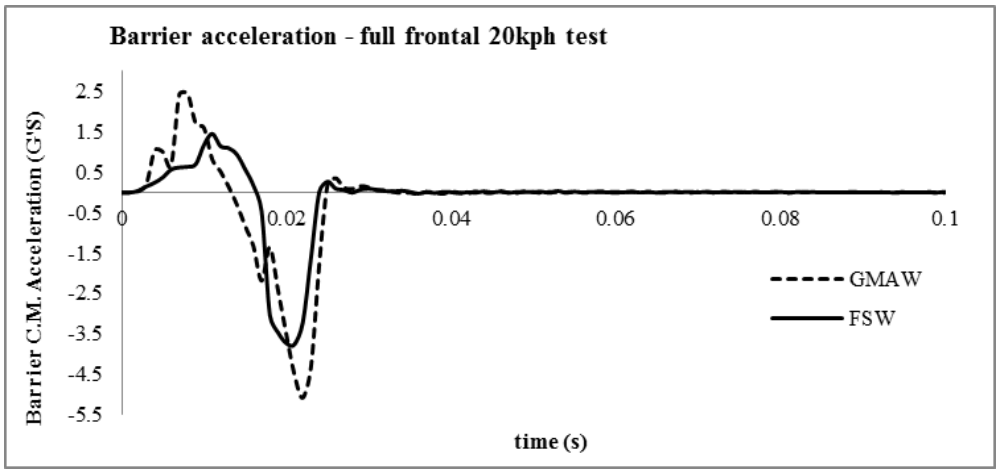

Figure 8.8. Barrier acceleration for FSW and GMAW bumpers at 20 kph energy target.

8.3.2 Deflection Measurement Results

A graphical comparison for bumper deflection in the full-frontal test using FSW bumpers is shown in Figure 8.9 for the 7, 10, 15, and 20 km/hr velocity levels.

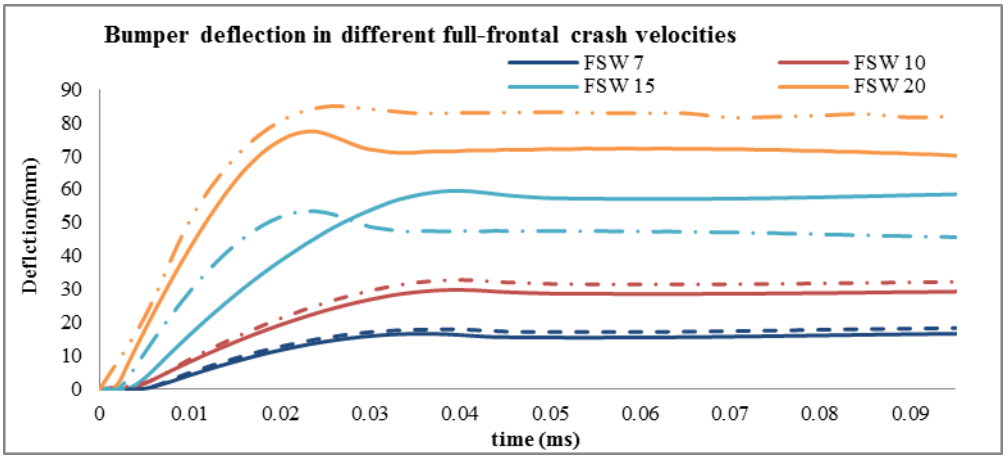

Figure 8.9. Deflection plot for FSW bumpers at 7, 10, 15, and 20 kph energy targets.

It is observed that as the crash speed increased, the rise time for the deflection curve increased due to less time needed to deflect the bumper at higher crash speeds. With the exception of the 15 km/hr crash speed, the bumper deflections using FSW bumpers were generally lower than that of GMAW bumpers. The contributing factor for this irregular observation at a 15 km/hr crash speed was due to the high percentage difference between the simulated and experimental bumper deflections. Accuracy of the simulation was determined by comparing the bumper deflection and failure at the weld joint of the simulation results with the experimental results. Table 8.4 shows a comparison of the experimental and simulated results for the FSW bumper. As can be seen, the percentage errors of the simulation with the experimental results are no more than 26%. Similarly, Table 8.5 shows a deflection comparison for GMAW bumpers, where it can be seen that the percentage of error is less than 20% for all cases. Overall, the simulated bumper deflection is in reasonable agreement with the experimental results. Thus, high confidence in the accuracy of the numerical method was achieved.

Table 8.4. Bumper Deflection Comparison of Experimental and Simulation Results for FSW Method

	Measured Bumper Velocity on Impact			
	7 km/hr	**10 km/hr**	**15 km/hr**	**20 km/hr**
Measured Bumper Deflection (mm)	14.1	27.2	45.5	79.8
Simulated Bumper Deflection (mm)	16.3	29.7	57.0	77.3
Percent Error	15.6	9.2	25.3	3.1

Table 8.5. Bumper Deflection Comparison of Experimental and Simulation Results for GMAW Method

	Measured Bumper Velocity on Impact			
	7 km/hr	**10 km/hr**	**15 km/hr**	**20 km/hr**
Measured Bumper Deflection (mm)	14.0	29.0	46.0	84.0
Simulated Bumper Deflection (mm)	16.4	32.7	53.4	84.1
Percent Error	17.1	12.8	16.0	0.1

8.3.3 Finite Element Model Validation

To evaluate the accuracy of the FE model, the simulation test results were compared with actual test results. In order for the simulation be fairly accurate, the profile of the deformed crash box and bumper data obtained from the simulation should closely match the profile of the deformed bumper and crash box from actual sled test results. Figure 8.10 shows a comparison of the deformation in the simulation and in the test results for all energy targets. As can be seen, the deformation configuration for the simulation was slightly different than actual deformation on the part. Based on the actual sled test, more deformation in the bumper walls was expected. As mentioned in the previous chapter, the assembled parts were mounted on the rigid wall for sled testing using only four bolts (see Figures 7.4 and 7.5 previously), where in the LS-DYNA simulation, the entire bottom of the crash box was constrained to the rigid wall. This might be one of the major causes for some variation between the simulated and actual test results. Another issue warranting further investigation would be the difference in deformation between the FE model and the actual test due to the possible reduction of mechanical properties between extruded materials compared to the sheet material used for coupon testing. Also, the type of elements used for the FE model could be considered for further investigation.

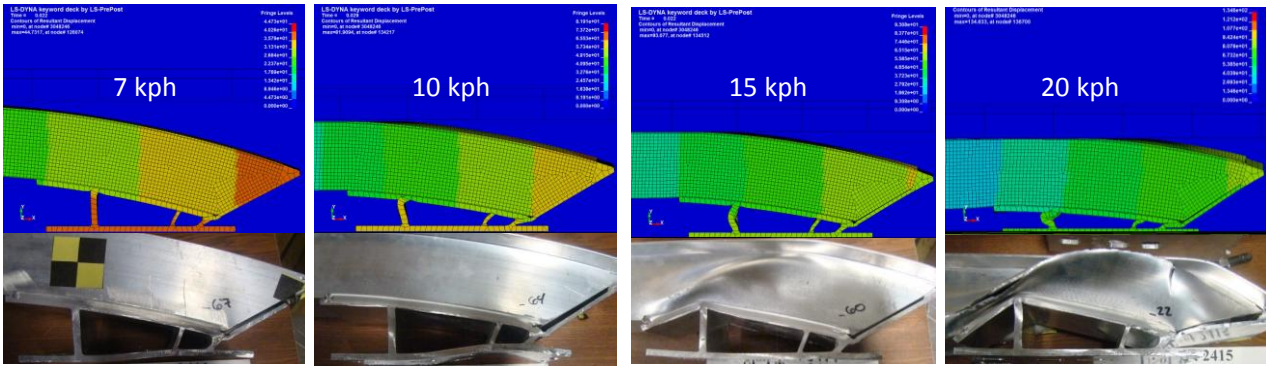

Figure 8.10. Comparison of deformation in actual test and LS-DYNA simulation.

8.4 Insurance Institute for Highway Safety Test Procedure (40% Offset Crash Test)

Based on confidence that the FE model worked properly and was validated against the actual test, this model could be expanded for different types of dynamic crash testing without the need for experimental runs. For example, a 40% offset crash test was conducted for the FE model. In the full-frontal impact test, force was distributed over the entire width of the car, which resulted in fewer intrusions and more integrity of the occupant compartment. Also, the deceleration level was lower in the offset test when compared to the full-frontal test. Like the full-frontal test, a rigid barrier was used with a 40% offset angle of the vehicle at 7, 10, 15, and 20 kph energy targets. This test led to the transfer of the entire impact load on one corner of the vehicle (bumper). Figure 8.11 represents a 40% right-side-driver offset crash test.

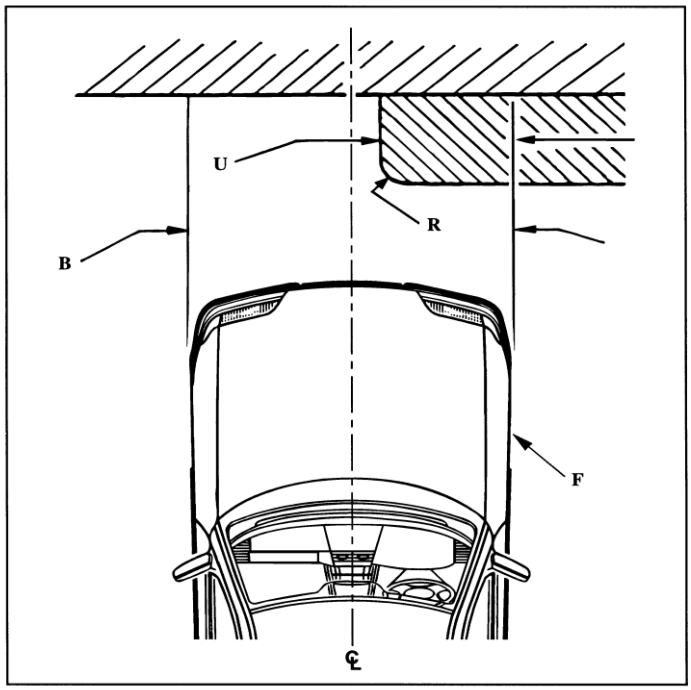

Right Hand Drive vehicle shown

Key:

U	=	Offset 40 %
B	=	Overall width of test vehicle (see 3.3)
V_F	=	15.0 + 1.0 - 0 km/h
R	=	150 mm constant radius
F	=	Test vehicle

Figure 8.11. 40% offset barrier crash test [92].

As shown in Figure 8.11, the vehicle is aligned with the barrier such that the left side of the vehicle centerline is offset to the right edge of the barrier. The vehicle model is replaced with the exact MDB used in the previous full-frontal test to ensure a fair comparison. This simulation setup evaluated the structural integrity and deflection of the occupant compartment because the impact forces were focused on 40% of the bumper area. In addition, the difference in performance between the FSW and GMAW methods was more pronounced due to a higher concentration of impact forces. Similar to the full-frontal experimental and numerical tests, the method of evaluating the performance of FSW and GMAW is through the measurement of bumper deflection and barrier acceleration.

8.4.1 Finite Element Analysis Results

A von Mises stress contour was plotted to visualize the stress distribution through the weld region, crash box, and bumper. Figures 8.12 and 8.13 represent the von Mises stress distribution at the instant of impact for FSW bumpers and GMAW bumpers at 7, 10, 15, and 20 kph energy targets. As can be seen, the amount of von Mises stress increased from the lower energy target to the higher energy target. In fact, in the offset test, the intrusions were intended to be higher, compared to the full-frontal test, due to the reduction of the area that absorbs energy with only 40% of the structure. It was ascertained that von Mises stress distribution for GMAW bumpers was greater than for FSW bumpers. It was also determined that the intrusions were higher for the bumper in the offset test due to the smaller energy-absorbing area. In general, the full-frontal impact test was more demanding on the restraints, where the offset test was more demanding on the structures.

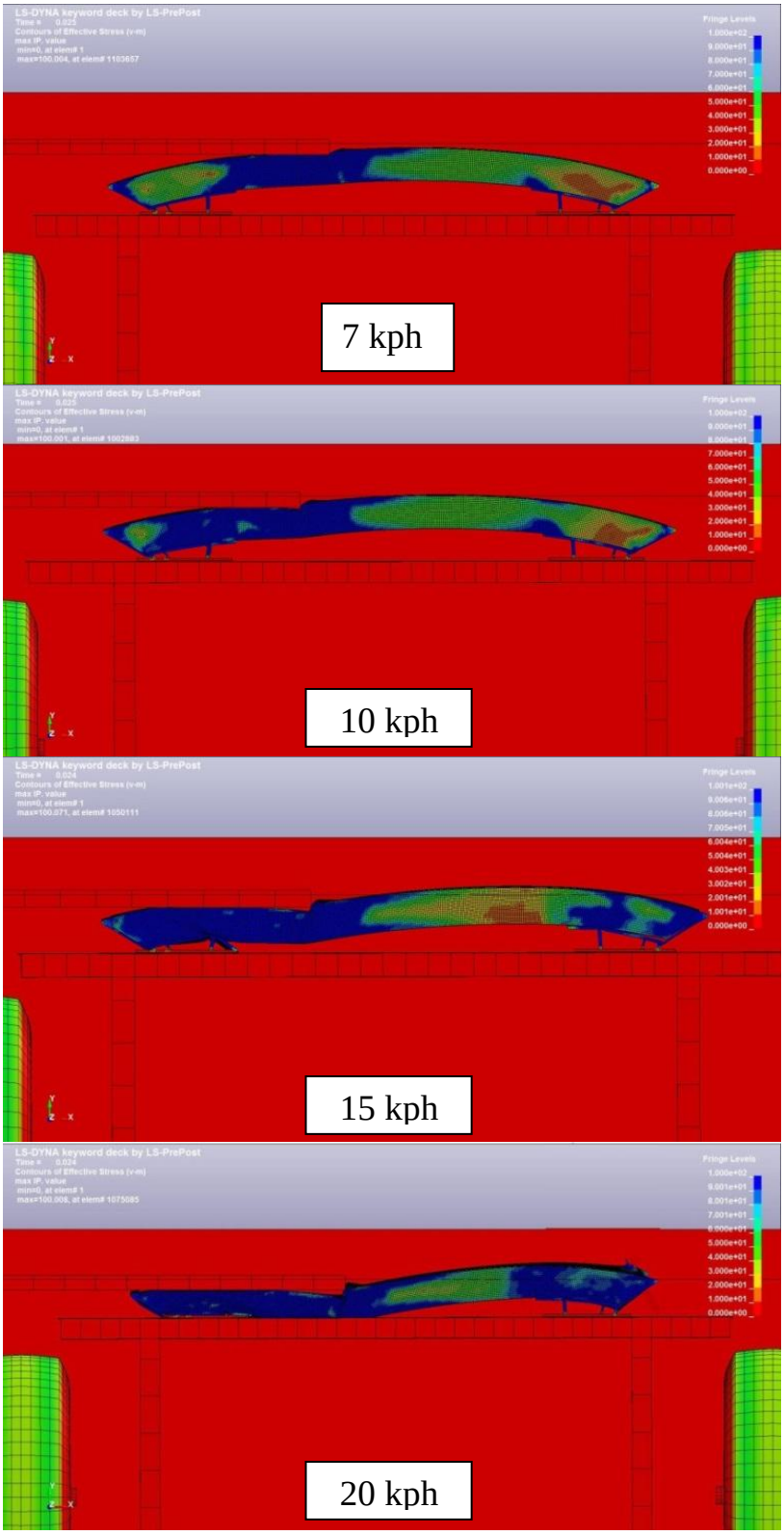

Figure 8.12. Von Mises stress distribution for 40% offset impact test at instant of impact for FSW bumpers at 7, 10, 15, and 20 kph energy targets.

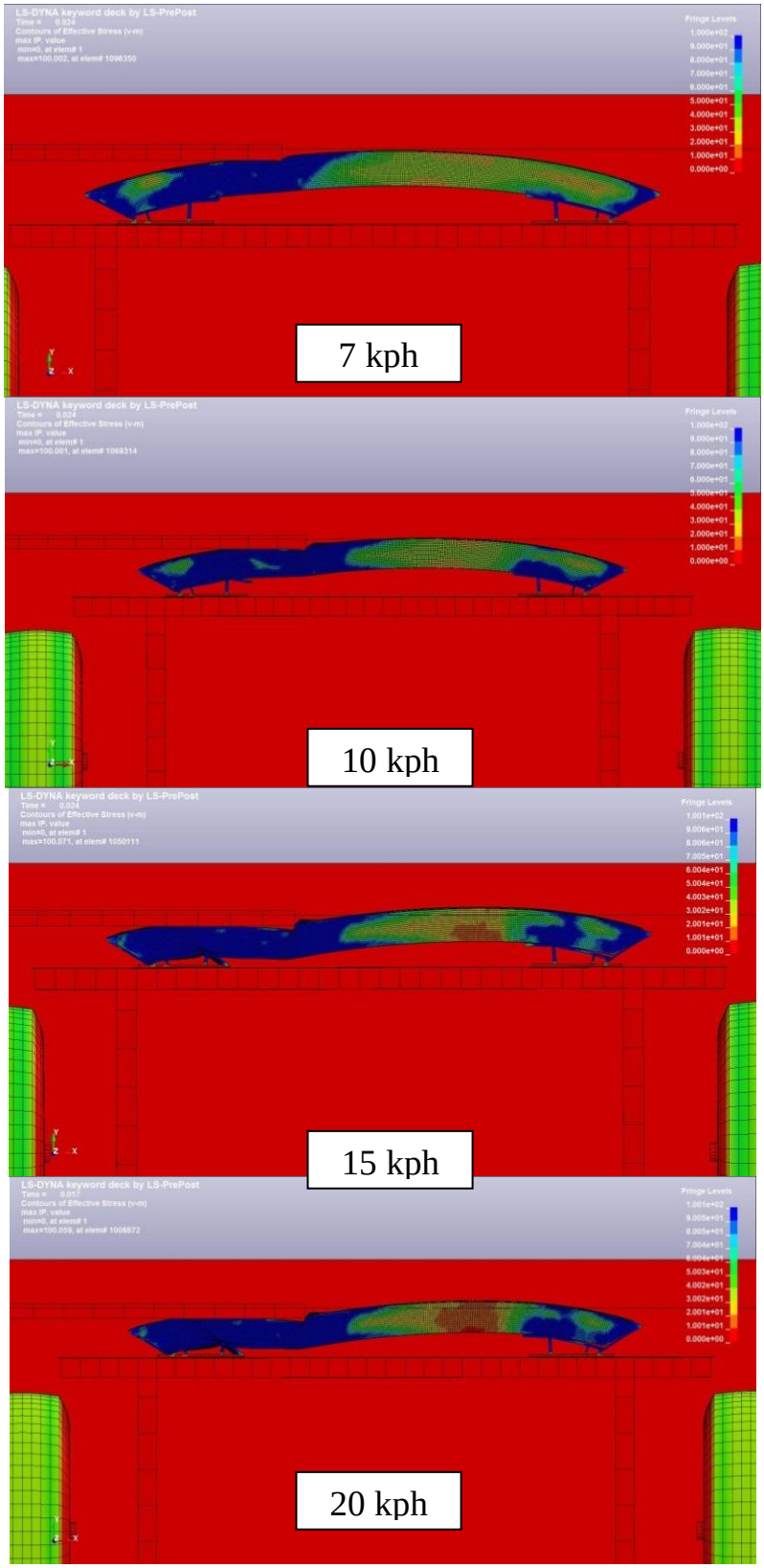

Figure 8.13. Von Mises stress distribution for 40% offset impact test at instant of impact for GMAW bumpers at 7, 10, 15, and 20 kph energy targets.

Figure 8.14 shows a stress comparison for FSW and GMAW bumpers at a 20 kph energy target. It is clearly evident that deformation for the 40% offset test was higher than that of the full-frontal test, due to the impact force concentrated on 40% of the barrier. In terms of weld quality, it can be seen that the FSW joint was mainly intact, while crack separation was visible in the GMAW joints. Furthermore, the FSW crash box was completely crashed, and the FSW bumper deformation was clearly less, in comparison to the GMAW bumper. Stress was shown to be evenly distributed with the FSW bumper, and a higher stress concentration was seen at the GMAW joint. Overall, based on these observations, the bumper deflection and stress distribution were better in the FSW joint.

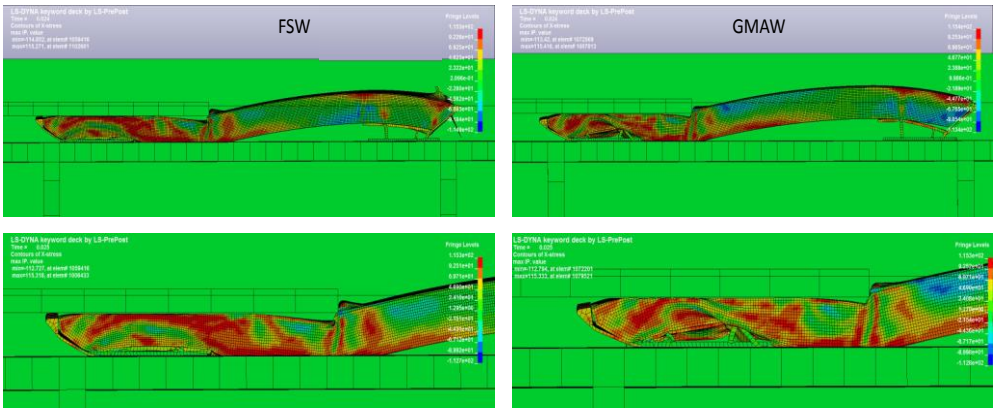

Figure 8.14. Stress comparison of FSW and GMAW bumpers at 20 kph energy target for 40% offset impact test.

Figure 8.15 shows the state of X-stress distribution for both FSW and GMAW bumpers at 20 kph. As can be seen, the amount of X-stress in GMAW bumpers was greater than the amount of X-stress achieved for FSW bumpers. Also, the highest amount of stress was 28 N/m^2 for FSW bumpers, where for the same condition, the greatest amount of the stress was about 67 N/m^2 for GMAW bumpers. This proves that FSW bumpers absorbed a higher amount of energy in comparison to GMAW bumpers.

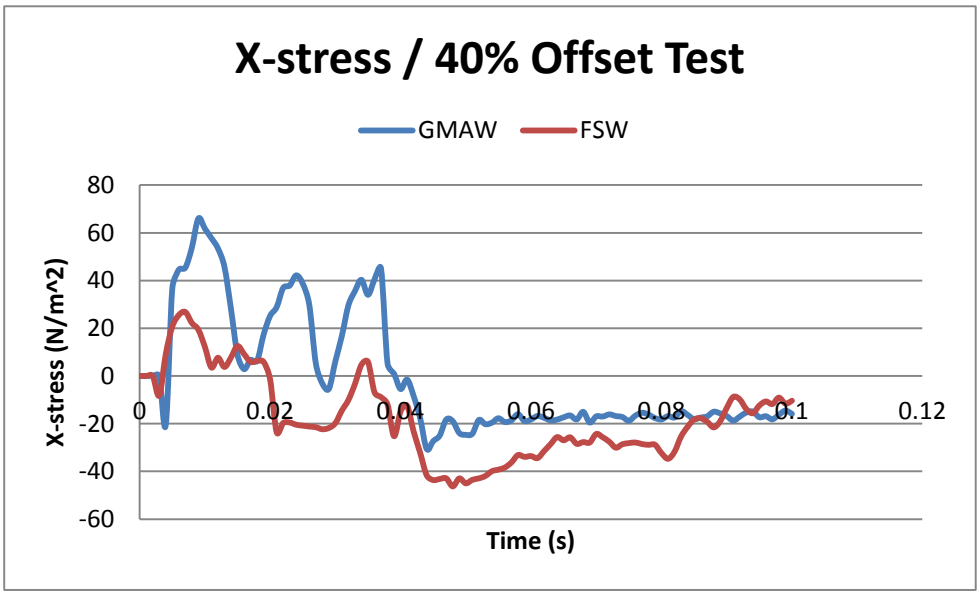

Figure 8.15. X-stress distribution for FSW and GMAW bumpers at 20 kph energy target.

The barrier acceleration for the 40% offset test is shown in Figure 8.16. Similar to the full-frontal test, acceleration with the FSW bumper was generally smoother and smaller in magnitude compared to the GMAW bumper. The peak acceleration with the FSW bumper was approximately 33% lower than that of the GMAW bumper. This 33% reduction in acceleration for the 40% offset test was even more significant than the 26% for the full-frontal.

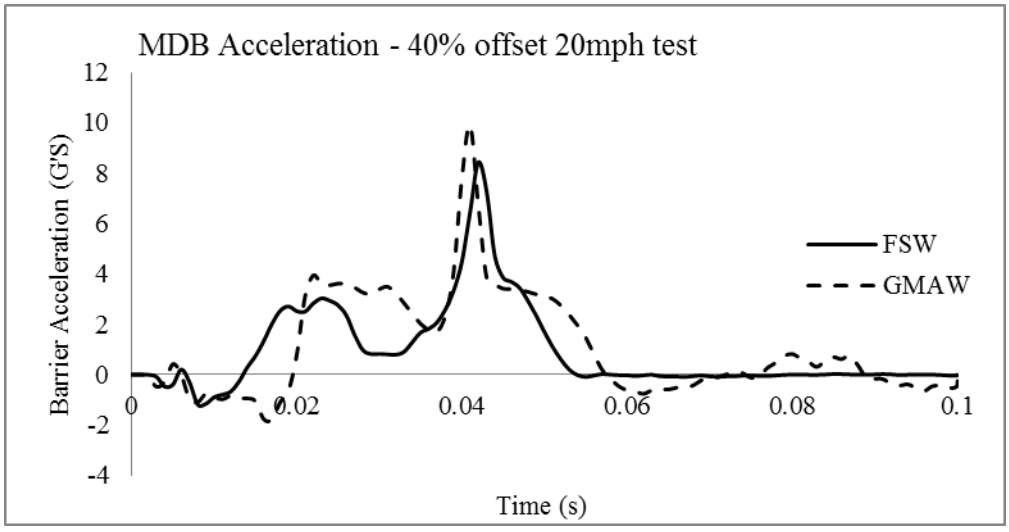

Figure 8.16. Barrier acceleration for FSW and GMAW bumpers at 20 kph energy target.

8.4.2 Deflection Measurement Results

The simulated bumper deflections at different crash velocities are summarized in Figure 8.17. It can be seen that FSW bumper deflections were constantly below that of GMAW bumpers for all crash velocities. However, the deflection differences between FSW and GMAW bumpers was less significant at lower crash velocities, namely, 7 and 10 km/hr. In terms of peak deflection, it is evident that the FSW bumper deflections at 7 and 10 km/hr were reduced by 18% and 17%, respectively, in comparison to GMAW. Hence, it is evident that the FSW bumpers were able to withstand higher crash velocities with lower deformations compared to GMAW bumpers.

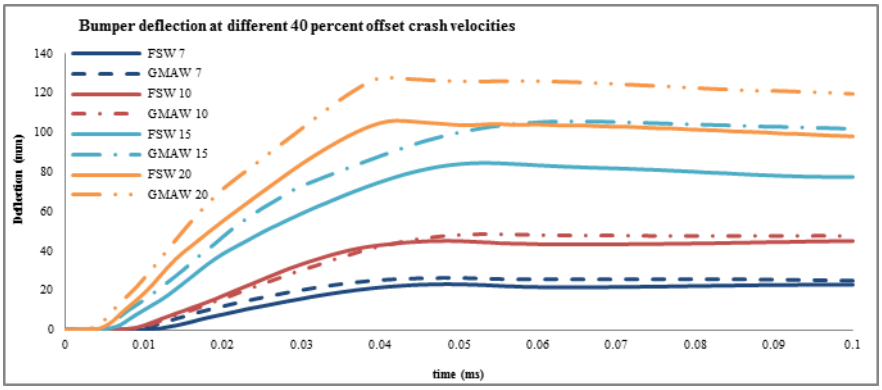

Figure 8.17. Deflection plot for FSW and GMAW bumpers at 7, 10, 15, and 20 kph energy targets.

CHAPTER 9

CONCLUSIONS

The primary objective of this study was to investigate the dynamic response of the FSW and GMAW bumper-beam/crash-box assembly using experimental and numerical methods. Friction stir-welded butt joints between AA6082-T6 and AA6063-T6 were produced from the results of optimized weld parameters using a DOE process. FSW joints of the dissimilar material showed lower ultimate stress properties compared to the parent material of both alloys. In the tensile tests, failure occurred in the nugget of the weld, where the minimum amount of hardness was observed. Also, according to the hardness profile of the joint, the lowest value of hardness was obtained in the center of the weld zone (nugget), corresponding to the location of failure when tensile testing the dissimilar butt weld joints. The joint efficiency for T6 heat-treated specimens increased 4% over naturally aged specimens and 6% over as-welded specimens. This joint efficiency was a marked improvement over the results in other published papers that were reviewed [79]. Microstructural properties and an analysis of the dissimilar joints, including the material flow and mixture of the two alloys, were clearly identified. The oscillations of the feedback forces were changed as the process heat input decreased, which provides evidence that feedback forces can be used for evaluating mechanical and metallurgical qualities of welded joints.

Friction stir lap weld joints between AA6082-T6 and AA6063-T6 were produced through the optimized weld parameters results of a DOE process. Also, according to the hardness profile of the joint, the lowest value of the hardness was obtained in the weld zone, corresponding to the location of the weld separation when shear testing the dissimilar lap weld joints. In the shear lap tests, separation occurred in three different modes: nugget of the weld where the minimum

amount of the hardness was observed (Mode 1), TMAZ on the retreating side where the possible hooking effect influenced separation of the weld and the highest amount of stress distribution was observed (Mode 2), and the base (parent) material of the specimens (Mode 3). The joint efficiency for T6 heat-treated specimens increased 3% over naturally aged specimens and 5% over as-welded specimens for advancing side loading of the Type A specimen configuration. Also, the joint efficiency for T6 heat-treated specimens increased 7% over naturally aged specimens and 11% over as-welded specimens for advancing side loading of Type B specimens. Microstructural properties and an analysis of the dissimilar lap joint, including material flow, mixture of the two alloys, and absence of the hooking effect, are clearly identified. It was also determined that advancing-side loading performed at a higher strength than retreating-side loading, which is evidence that retreating side loading is not a good application in FSW due to weaker weld strength on this side. The oscillations of feedback forces were changed as the process heat input decreased, which provides evidence that the feedback forces can be used for evaluating mechanical and metallurgical qualities of welded joints. Also, it was ascertained that feedback force signals contain more low-frequency oscillations, while material resistance in response to the tool motions increases. Finally, finite element analysis was used to determine the displacements and stress distribution that a lap weld sample undergoes during a shear test. The model deformed in the same way that the actual specimens deformed during shear testing. Also, the maximum amount of the stress distribution, based on a von Mises contour plot, was obtained in the interface of the top and bottom sheets.

It was observed that FSW butt welds performed as well as or better than GMAW welds. Weld tool development can tailor weld flow for producing tough joints that are without voids. Weld tool development can be aided by toughness plots, component testing, and e-NDE (force

feedback frequency spectra analyses). The rate of crack growth in FSW joints is not faster than in parent material due to the improved ductility in the weld zone. This was evidenced by the parent material in the assembly corners and side walls rupturing at higher speeds, while the friction stir welds folded and remained intact, demonstrating stable crack growth extending from the weld ends. Crack separation in the parent material appeared to move into the heat-affected weld zone after buckling. However, it has not been determined if this is a result of proximity to the joint or a material property influence caused by the HAZ associated with the FSW joint.

The experimental method was evaluated using a full-frontal sled test to evaluate the maximum deformation of the bumper and crack propagation at the weld joint. In addition, a numerical method was utilized to evaluate similar performance parameters by using the non-linear dynamic software LS-DYNA. The simulated bumper deflections for the full-frontal test were validated and shown to be in good agreement with the experimental results. The crash velocities for experimental and numerical methods were selected to be 7, 10, 15, and 20 km/hr. In addition to the full-frontal test, the computer simulation was also utilized in evaluating the performance of FSW and GMAW bumpers in an NCAP 40% offset test.

For the full-frontal experimental and simulated results, the overall bumper deflection was reduced with FSW, compared to GMAW. The performance of the FSW bumper-beam/crash-box assembly at higher crash velocities was generally better than at lower crash velocities. Similarly, bumper deflections for the 40% offset test with GMAW were consistently higher compared to FSW over all crash velocities. It was apparent that the performance of FSW and GMAW techniques is more significant in the 40% offset test compared to the full-frontal test. The FSW bumper, compared to the GMAW bumper, indicated a reduction of approximately 20% in bumper deflection for the 40% offset test and only 5% for the full-frontal test. In broad terms, the

increase in bumper strength, due to good energy distribution, allowed the bumper to sustain higher crash velocities while maintaining its structural integrity.

In terms of weld quality, no separation or crack growth was observed with FSW, while weld separation was observed in GMAW across all test velocities. The absence of cracks in FSW joints, indicating good material ductility, increased the energy transferred from the bumper to the crash box. Also, as shown in the experimental and numerical results, the FSW crash box at 20 km/hr was completely crushed, also indicating higher energy absorbed by the crash box. The complexity of crack growth was not indicated completely in the simulated model because it was assumed that the bumper was friction stir welded and gas metal arc welded onto the crash box in ideal scenarios. In addition, stress distributions were measured for both full-frontal and 40% offset, and it was shown that stresses in the bumper were evenly distributed and smaller in magnitude in the FSW bumper compared to the GMAW bumper.

Overall, the experimental and numerical method presented in this study proved that the structural strength of the bumper was enhanced with FSW, compared to the conventional and popular method of GMAW. Future work may include friction stir welding the bumper to a full-sized vehicle model to provide a more accurate analysis of the response of the vehicle in a more realistic frontal-crash scenario.

REFERENCES

LIST OF REFERENCES

[1] Mishra, R.S., and Mahoney, M.W., "Friction Stir Welding and Processing," Materials Park, OH, 2007, 1–78 pp.

[2] Prater, T., "An Investigation into the Friction Stir Welding of AL 6061 and AL 6061/SiC/17.5p Using Diamond Coatings," Vanderbilt University, Nashville, TN, 2008.

[3] Brown, J., "The Effects of Sealants and Surface Treatments on the Faying Surface of Swept Friction Stir Spot Welds," Master's Thesis, Wichita State University, Wichita, Kansas, 2008.

[4] Matsumoto, K., and Sasabe S., "Lap Joints of Aluminum Alloys by Friction Stir Welding" *Proceedings of the 3rd International Symposium on FSW*, Kobe, Japan, 2001.

[5] Nandan, R., DebRoy, T., and Bhadeshia, H.K.D.H., "Recent Advances in Friction Stir Welding Process, Weldment Structure and Properties," Pennsylvania State University, University Park, PA, 2008.

[6] Ericsson, M., Jin, L., and Sandstrom, R., "Fatigue Properties of Friction Stir Overlap Welds," *International Journal of Fatigue*, 2007, pp. 57–68.

[7] Burford, D. Gimenez-Britos, P., Boldsaikhan, E., and Brown, J., "Evaluation of Friction Stir Weld Process and Properties for Aerospace Application: e-NDE for Friction Stir Processes," FAA Joint Advanced Materials & Structures (JAMS) Center of Excellence, 6th Annual Technical Review Meeting, May, 2010.

[8] Boldsaikhan, E., Logar, A., and Corwin,E., *Real-Time Evaluation in Friction Stir Welding: The Use of Feedback Forces for Nondestructive Evaluation of Friction Stir Welding*, Lambert Academic Publishing, 2010.

[9] Mishra, R.S., and Ma, Z.Y., "Friction Stir Welding and Processing," *Materials Science and Engineering* Research Reports, vol. 50, 2005, pp. 1–78.

[10] Arbegast, W.J., "Friction Stir Welding: After a Decade of Development, Friction Stir Welding and Processing IV," TMS 2007, Orlando, Florida, February, 2007.

[11] Widener, C.A., "Evaluation of Post-Weld Heat Treatments for Corrosion Protection in Friction Stir Welded 2024 and 7075 Aluminum Alloys," Ph.D. Dissertation, Wichita State University, Wichita, Kansas, December 2005.

[12] Baratzadeh, F., Widener, C.A., Lankarani, H. M., and Burford, D.A., "Methods to Increase the Fatigue Life of Friction Stir Lap Welds in No-Load Transfer Coupons Using a Retractable Pin Tool," *Journal of ASTM International*, vol. 9, no. 5, 16p published online May 2012.

[13] Baratzadeh, F., Handyside, A.B., Boldsaikhan, E., Lankarani, H., Carlson, B., and Burford, D., "Friction Stir Lap Welds of Dissimillar Aluminum Alloys of AA6082-T6 with AA6063D. -T6," submitted to *science and technology of welding and joining journal*, 14p, Nov 2013.

[14] Burford, D. A., "Friction Stir Welding of Airframe Structure: From One Delivery System to Another," *SAE International*, vol. 112, 2003, pp. 295–300.

[15] Baratzadeh, F., "An Investigation into Methods to Increase the Fatigue Life of Friction Stir Lap Welds," M.S. Thesis, Wichita State University, Wichita, Kansas, 2010, pp. 9–12.

[16] Friction Stir Processing and Its Applications, <http://www.scribd.com/doc/4612026/Friction-Stir-Processing>, cited 2009.

[17] Rowe. CED, and Thomas. W.," B.Sc.C.Eng.C.Sci.MIMMM SenMWeldI Cedar Metals Limited," and Thomas, W." Advances in Tooling Materials for Friction Stir Welding," 2010.

[18] Prater, T., "An Investigation into the Friction Stir Welding of AL 6061 and AL6061/SiC/17.5p Using Diamond Coatings," Master's Thesis, 2008.

[19] Burford, D. A., "Friction Stir Welding Tool Having a CounterFlow Pin Configuration," U.S. Patent No. 7942306 , April, 2007.

[20] The A to Z of Materials, http://www.azom.com/details.asp, cited 2010.

[21] Khaled, T.," An Outsider Looks At Friction Stir Welding," Report #ANM-112N-05-06, July 2005.

[22] Arbegast, W.J., "Modeling Friction Stir Joining as a Metalworking Process," *Hot Deformation of Aluminum Alloys III*, TMS Annual Meeting, San Diego, CA, March, 2003, pp. 313–327.

[23] Reynolds, A.P., and Tang, W., "Alloy, Tool Geometry, and Process Parameter Effects on Friction Stir Weld Energies and Resultant FSW Joint Properties," *Friction Stir Welding and Processing*, Indianapolis, IN, November, 2001, pp. 15-23.

[24] The TWI website, <http://www.twi.co.uk/technical-knowledge/published-papers/development-and-implementation-of-innovative-joining-processes-in-the-automotive-industry-september-2005/>, cited September 2012.

[25] Brooker, M.J., van Deudekom, A.J.M., Kallee, S.W., and Sketchley, P.D., Second International Symposium on Friction Stir Welding (Session 9), Gothenburg, Sweden, June, 2000.

[26] Feldman, K., Kohn, G., and Stern, A., "Friction Stir Spot Welding: 1. JT Welding Technologies Ltd. 2. Departments of Mechanical and Materials Engineering Ben Gurion University of the Negev.

[27] Badarinarayan, H., Hunt, F., Okamoto1, K., and Hirasawa, S., "Study of Plunge Motion during FSW: Temperature and Flow Pattern,".

[28] <http://www.mse.utoronto.ca/Assets/pdfs/north.pdf>, cited 2009.

[29] <http://www.mek.dtu.dk/Forskning/Projekter-phd/phd_trinecoldinglomholt.aspx>, cited 2012.

[30] Tweedy, B.M., "Factors Affecting the Properties of Swept Friction Stir Spot Weld," *Proceedings of the 2008 SAE World Congress*, Detroit, MI, 2008.

[31] Oberembt, C. "Screening for Process Variable Sensitivity in Refill Friction Spot Welding of 6061 Aluminum Sheet," *Friction Stir Welding and Processing IV, TMS 2007*, Orlando, Florida, February, 2007.

[32] Addison, A.C., and Robelou, A.J., "Friction Stir Spot Welding: Principal Parameters and Their Effects," *Proceedings of the 5th International Friction Stir Welding Symposium*, sponsored by TWI, Ltd., Metz, France, September, 2004.

[33] Burford, D.A., Tweedy, B.M., and Widener, C.A. "Fatigue Crack Growth in Integrally Stiffened Panels Joined Using Friction Stir Welding and Swept Friction Stir Spot Welding," *Journal of ASTM International*, vol. 5, no. 4, Paper ID JAI101568, 2009.

[34] Bergdahl Associates, Inc., PR-1432 GP Material Safety Data Sheet, <http://www.bergdahl.com>, cited 2009.

[35] Merry, J., Tweedy, B., Widener, C., and Burford, D., "Static Strength Comparision of Discountinuous Friction Stir Welded Stiffened Panels," 7th AIAA Aviation Technology, Integration and Operations Conference (ATIO), Belfast, Northen Ireland, September, 2007.

[36] Addision, A.C., and Robelou, A.J., "Friction Stir Spot Welding: Principal Parameters and their Effects," *Proceedings of the Fifth Internatiomal Conference on Friction Stir Welding*, TWI, Metz, France, September, 2004.

[37] <www.corrosionsource.com/technicallibrary/corrdoctors/Modules/Matselect/corralumin.htm#Many>, cited 2009.

[38] Davenport, A.J., Ambat, R., Jariyaboon, M., and Connolly, B.J., "Corrosion of Friction Stir Welds in Aerospace Alloys," Corrosion and Protection of Light Metal Alloys: *Proceedings of the International Symposium*, vol. 23, 2003, pp. 403–412.

[39] Williams, S., Ambat, R., Price, D., Jariyaboon, M., Davenport, A., and Wescott, A., "Laser Treatment Method for Improvement of the Corrosion Resistance of Friction Stir Welds," *Materials Science Forum*, vols. 426-432, 2003, pp. 2855-2860.

[40] <http://corrosion-doctors.org/Forms-Uniform/uniform.htm>. cited 2009.

[41] <http://www.corrosionsource.com/technicallibrary/corrdoctors/Modules/Forms/exfoliation.htm>, cited 2009.

[42] Uhlig, H., *Corrosion and Corrosion Control*, 2nd ed., John Wiley & Sons, New York, 1963, pp.13–16.

[43] Jariyaboon, M., Davenport, A.J., Ambat, R., Connolly, B.J., Williams, S.W., and Price., D.A., "The Effect of Welding Parameters on the Corrosion Behavior of Friction Stir Welded AA2024-T351," *Corrosion Science*," vol. 49, iss. 2, February 2007, pp. 877–909.

[44] <http://www.efunda.com/Materials/alloys/aluminum/aluminum.cfm>, cited 2009.

[45] Mazzolani, F.M., *Aluminum Alloy Structures*, Second Edition, E & FN Spon, London, UK., 1995.

[46] <http://en.wikipedia.org/wiki/Aluminium_alloy>, cited 2009.

[47] <http://aluminium.matter.org.uk>, cited 2012.

[48] Karlsson, L., Svensson, L., and Larsson, H., "Characteristics of Friction Stir Welded Aluminum Alloys: Trends in Welding Research," Proceedings of the Fifth International Conference, Pine Mountain, GA, June, 1998, J. Vitek, S. David, J. Johnson, H, Smartt, and T. Debroy, Ed., ASM International, Materials Park, OH, 1999, pp. 574–579.

[49] Baratzadeh, F., Handyside, A.B., Boldsaikhan, E., Lankarani, H., Carlson, B., and Burford, D., "Microstructural and Mechanical Properties of Friction Stir Welding Joints of 6082-T6 with 6063-T6," *Friction Stir Welding and Processing VI*, TMS, 2011.

[50] Ericsson, M., Sandstrom, R., and Hagstrom, J. "Second International Symposium on Friction Stir Welding," Gothenburg, Sweden, June, 2000.

[51] Singh, P., Gandhi, S. K., and Shergill, H., "Evaluation of Strength Degradation and Microstructure in Friction Stir Welded Aluminium 6063-T6," *International Journal of Engineering Research & Technology*, vol. 1, iss. 7, September 2012.

[52] Mroczka, K., and Pietras, A., "FSW Characterization of 6082 Aluminum Alloys Sheets" *International Scientific Journal*, vol. 40, December 2009, pp. 104–109.

[53] Larsson, H., Karlsson, L., and Svensson, L.E., "Friction Stir Welding of AA 5083 and AA 6082 Aluminium," *Svetsaren*, vol. 2, 2000, pp. 6–10.

[54] Moreira, P.M.G.P., de Oliviera, F.M.F., and de Castro, P.M.S.T., "Friction Stir Welded Aluminum Alloy 6063-T6: Mechanical Characterization, Fatigue Tests and Defects Identification" 8th Mesomechanics, Porto, Portugal, July, 2006.

[55] <http://www.ssip.net/manufacturers/mazda/model/mazda-rx8>, cited 2012.

[56] <http://www.aws.org/w/a/wj/2004/02/hancock_feature/index.html>, cited 2012.

[57] <http://www.fpe.co.uk/applications/aerospace>, cited 2012.

[58] Rio Tinto Alcan, 6082 bumper extrusion and 6063 crash box extrusion supplier, <http://comalco.migrate.f5.com.au/freedom.aspx?pid=526>, cited 2010. .

[59] ASTM B557, Standard Test Methods for Tension Testing Wrought and Cast Aluminum- and Magnesium-Alloy Products, ASTM International, 2010.

[60] ASTM B 918/B 918M, Standard Practice for Heat Treatment of Wrought Aluminum Alloys, ASTM International, 2009.

[61] Kaufman, J.G., *ASM International Specialty Handbook*, Materials Park, Ohio, p. 272.

[62] Kristensen, J.K. LIST ALL AUTHORS HERE, "Properties of Friction Stir Welded Joints in the Aluminum Alloys 2024, 5083, 6082/6060 and 7075," *5th International Symposium on FSW*, vol. 6, 2004, p. 19.

[63] Baratzadeh, F., Handyside, A. B., Buller, J., Burford, D., Carlson, B., Boldsaikhan, E., "Performance Evaluation of Discontinuous Friction Stir Welding: Bumper Beam/Crash Box Case Study," CFSP Annual Report, 2011.

[64] Cederqvist, L., and Reynolds, A.P., "Factors Affecting the Properties of Friction Stir Welded Aluminum Lap Joints" *Welding Journal*, vol. 80, iss. 12, 2001, pp. 281S–287S

.

[65] Matsumoto, K., and Sasabe, S., "Lap Joint of Aluminum Alloys by Friction Stir Welding," Third International Symposium on Friction Stir Welding, Port Island, Kobe, Japan, September, 2001.

[66] Mishra, R.S., and Mahoney, M.W., "Introduction," in *Friction Stir Welding and Processing*, Materials Park, OH, 2007, pp. 1–5, courtesy of TWI, Ltd.

[67] Boldsaikhan, E., Corwin, E.M., Logar, A.M., and Arbegast, W.J., "The Use of Neural Network and Discrete Fourier Transform for Real-Time Evaluation of Friction Stir Welding," *Applied Soft Computing*, Elsevier, vol. 11-8, 2011, pp. 4839–4846.

[68] Arbegast, W.J., "Using Process Forces as a Statistical Process Control Tool for Friction Stir Welds," in *Friction Stir Welding and Processing III*, TMS, K. V. Jata, M. W. Mahoney, R. S. Mishra, and T. J. Lienert (Eds.), 2005, pp. 193–203.

[69] Morihara, T. "Investigations into the Use of Dynamic Spectra Response of Friction Stir Welding Forces, Master's Thesis, South Dakota School of Mines and Technology, Rapid City, SD, 2004.

[70] Cao, X., and Jahazi, M., "Effect of Welding Speed on Lap Joint Quality of Friction Stir Welded AZ31 Magnesium Alloy," 8th ASM International Conference, 2009, pp. 72–80,

[71] Yazdanian, S., Chen, Z.W., and Littlefair, G., "Mechanical Properties of Al and Mg Alloy Welds Made Using Friction Stir Lap Welding," *Friction Stir Welding and Processing VI*, TMS, 2011.

[72] Hendricks, C. E. "The Mechanical Effects of Weavetrack on Friction Stir Welds in a Lap Configuration," Master's Thesis, Nashville, Tennessee, August 2009.

[73] Livermore Software Technology Corporation, <http://www.lstc.com>,

[74] Naidu, R., "Friction Stir Welding: Thermal Effects of a Parametric Study on Butt and Lap Welds," Master's Thesis, Wichita State University, Wichita, Kansas, 2006.

[75] Handyside, A.B., Baratzadeh, F., Buller, J., Lankarani, H., Carlson, B., and Burford, D., "Friction Stir Welded 'A' Frame for Dual Function Test Fixture," *Friction Stir Welding and Processing VI*, TMS, 2011.

[76] Handyside, A.B., "Dual-Function Fixture Design for Dynamic Testing of Automotive Bumper/Crash-Box Case Study Utilizing Friction Stir Welding, Master's Thesis, Wichita State University, 2011.

[77] Federal Motor Vehicle Safety Standard (FMVSS 208) Part 581, <http://www.nhtsa.gov/cars/rules/import/fmvss/index.html#P581>, cited 2010.

[78] National Highway Traffic Safety Administration, <http://www.nhtsa.dot.gov>, cited 2010.

[79] Moreira, P.M.G.P., Santos, T., Tavares, S.M.O., Richter-Trummer, V., Vilaca, P., and de Castro, P.M.S.T., "Mechanical and Metallurgical Characterization of Friction Stir Welding Joints of AA6061-T6 with AA6082-T6," *Material and Design*, vol. 30, 2009, pp. 180–187.

[89] <http://www.safecarguide.com/exp/euroncap/euroncap.htm>, cited April 2013.

[90] Research Council for Automotive Repairs (ICT-RCAR), "The Procedure for Conducting a Low Speed 15 km/h Offset Insurance Crash Test to Determine the Damageability and Repairability Features of Motor Vehicles," Issue 1, January 1999, Office of Vehicle Safety Compliance, Washington, DC 20590, <http://www.rcar.org/Papers/Procedures/crash_test.pd>, cited 2010.

[91] Sahare, L., "Flexible Chassis and Seat Mechanism for Frontal Impact Protection," Master's Thesis, Wichita State University, Wichita, Kansas, 2004.

[92] Research Council for Automotive Repairs (ICT-RCAR), "The Procedure for Conducting a Low Speed 15 km/h Offset Insurance Crash Test to Determine the Damageability and Repairability Features of Motor Vehicles," Issue 1, January 1999, Office of Vehicle Safety Compliance, Washington, DC 20590, <http://www.rcar.org/Papers/Procedures/crash_test.pdf>, cited 2010.

[93] Özel, T., and Karpat, Y., "Identification of Constitutive Material Model Parameters for High-Strain Rate Metal Cutting Conditions Using Evolutionary Computational Algorithms," Department of Industrial and Systems Engineering, Rutgers University.

[94] Jeremy, D. S, Gilar, A., Jerome, A. K., and John, R. L., "High Strain Rate, High Temperature Constitutive and Failure Models for EOD Impact Scenarios," *Proceedings of 2007 SEM*, 2007.